This is to certify that the

dissertation entitled

CHARACTERIZATION AND MODELING OF A COMPACT ECR PLASMA SOURCE DESIGNED FOR MATERIALS PROCESSING

presented by

Meng-Hua Tsai

has been accepted towards fulfillment
of the requirements for

Ph.D. degree in Electrical Eng

Timothy Gougeth
Major professor

Date 8/16/99

CHARACTERIZATION AND MODELING OF A COMPACT ECR PLASMA SOURCE DESIGNED FOR MATERIALS PROCESSING

By

MENG-HUA TSAI

A DISSERTATION

Submitted to
Michigan State University
in partial fulfillment of the requirements
for the degree of

DOCTOR OF PHILOSOPHY

Department of Electrical and Computer Engineering

1999

ABSTRACT

CHARACTERIZATION AND MODELING OF A COMPACT ECR PLASMA SOURCE DESIGNED FOR MATERIALS PROCESSING

By

MENG-HUA TSAI

A compact ECR ion/free-radical source designed for materials processing is experimentally characterized and modeled under conditions typical for materials processing. Specifically, argon, hydrogen and hydrogen-argon discharges are created and studied in a compact microwave ECR (electron cyclotron resonance) plasma source operating in the 0.4-5 mTorr pressure range. The source has a discharge region of 3.6 cm in diameter and an excitation volume of 50 cm^3. The plasma species diffuse out of the source into a larger materials processing region. The discharge is excited at a frequency of 2.45 GHz with input power levels of 50-90 watts. Measurements of the ion density, electron temperature, and absolute atomic hydrogen concentration are performed using Langmuir probes, OES (optical emission spectroscopy) and actinometry. Measurements are performed in both the source/excitation region and in the downstream processing region.

A global model for the discharges in this plasma source and a downstream charge particle diffusion model are also developed. The features of these plasma discharges determined by the combined measurements and models include a source region ion density in the 10^{11} cm^{-3} range, which corresponds to an ionization ratio of 0.001 to 0.01. For the pure hydrogen discharges, the dominant ion species was H_2^+. Also, it was found for the hydrogen discharge that the electron temperature was in the range 5-8 eV, the atomic

hydrogen molar fraction was measured as 25-34% with an increasing fraction at higher pressures, and the surface recombination coefficient of atomic hydrogen was determined to be approximately 0.005. Argon and argon-hydrogen discharge mixtures were also modeled. The global model developed includes the effect of magnetic confinement/electron heating enhancement by the ECR magnets in the source. Extensive comparisons are made between the experimental measurements and the global model results.

To my mother,

whose great personality has been a continuous

inspiration and encouragement to me.

ACKNOWLEDGMENTS

I would like to thank Dr. Timothy Grotjohn, my academic advisor, for his continuous support and encouragement during the study of this dissertation. His years of experience in both modeling and experimenting in plasma sources has been a great help and inspiration throughout the completion of this work. Special thanks to Dr. Jes Asmussen for his support and many valuable suggestions during my years of study in Michigan State University. I would also like to thank my committee members, Dr. Don Reinhard and Dr. Norman Birdge, for their patience to proof-read my manuscript in such a short time. Many thanks to my friends, Peng U. Mak, Bo K. Kim, Mark Perrin, and Robert Pcionek for lots of useful discussions concerning the experiments and their wonderful friendship. Finally, I would like to thank my family who always believe in my completion of this dissertation. Thank you so much, my son, Jerry, who brought so much joys and laughters to my life since you were born in summer 1998.

List

List

Cha
Intr

Cha
High

Chap
The

Table of Contents

List of Tables

Chapter 3

Chapter 4

Chapter 5

List of Figures

Chapter 2

Chapter 3

Chapter 4

Chapter 5

Chapter 6

CHAPTER 1

Introduction

1.1 Motivation for High Density Plasma Sources

In recent years, plasma-aided dry etching has been widely used for fine pattern transfer in the fabrication of very large scale integrated (VLSI) circuits [1]. As integrated circuit device dimensions continue to drop below a quarter micron, a low-pressure, high-density plasma source (LPHD) is required for material processing to achieve more precise dimension control, faster processing rates, and lower substrate temperatures during the processing period.

Microwave electron cyclotron resonance (ECR) plasma sources are one possible LPHD source type available to fulfill this increasing demand of semiconductor manufacturing. They are able to provide a low pressure, low neutral gas temperature plasma which has low ion energies that minimizes the possible damage (dopant redistribution, thermal stress) to the substrate during the processing. In a low pressure (no more than a few mTorr) discharge, the collision frequency is low, the chemical interactions between the particles are minimized, and hence one of the primary interactions is between the charged particles and the processing surfaces. With these features, microwave ECR plasma sources may provide some useful applications in plasma-assisted etching,

sputtering, implantation, and deposition in integrated circuit fabrication. Specifically, studies have demonstrated their use in more precise etching line profile control [2]-[4], and in higher etch rates for polymers [5]. Other examples include lower oxidation temperatures in the conversion of Si to SiO_2 [6], low temperature homoepitaxial growth of Si by plasma enhanced chemical vapor deposition [7], and ECR plasma etching for selective and uniform high rate etching of polysilicon [8]. Additionally, as radiation damage induced by ion bombardment is becoming an issue, the lower ion energies produced in a microwave plasma may also offer some benefit in reduced damage.

1.2 Research Goals

Historically, plasma processes were often developed using a repeated trial/ incremental improvement approach. However, with increasing demands on the control and repeatability of plasma processes, a different approach relying on careful measurements and accurate models is becoming more necessary. Toward this end, this thesis work carefully characterizes and models a compact ECR ion/free radical source used for a range of material processing applications. The measurements and models developed in this thesis will be useful in directing the future applications and design modifications of ECR sources.

The first objective in this thesis is to understand via experimental characterization the plasma generation in an ECR plasma source. This characterization includes the ion density, electron density, electron temperature, neutral radical density, and electron energy distribution function (EEDF). Both noble and molecular gas discharges will be studied

including argon, hydrogen, and argon-hydrogen mixture discharges. The second objective is to develop appropriate models which predict the discharge properties for ECR plasma sources. The particular structure of the plasma reactor in this thesis is the MPDR 610 compact ECR ion/free radical source.

The research plan to achieve the objective of better understanding and controlling of the plasma during material processing begins by dividing the study of the source into sub-problems based on various plasma reactor regions including the plasma generation region, the processing chamber region, and the immediate substrate region (i.e., the substrate and its sheath). The first two regions will be studied in this work using a combined approach of experimental diagnostics and modeling.

Another technique that will allow the objective to be reached without tackling the most difficult problem immediately is to start with a single gas type discharge and work to the more complex gas mixture discharges which are usually the case in plasma processing. The discharges to be considered include argon, hydrogen, and argon-hydrogen mixtures.

1.3 Dissertation Outline

This dissertation starts with a brief introduction of the demanding trend for high density-low pressure plasma sources in the semiconductor industry. Chapter 2 gives a brief review of the some of the high density plasma sources (rf and microwave powered). The applications for these plasma sources in material processing are also introduced. Chapter 3 and 4 discuss the experimental approach to the diagnosis of the discharge characteristics. The experimental diagnostic techniques are described in Chapter 3. The techniques

employed in this study include single and double Langmuir probes and optical emission spectroscopy (OES). Chapter 4 presents the experimental results utilizing the characterization techniques described in Chapter 3. The plasma source properties measured are electron temperature, neutral and ion density, and electron energy distribution function. In addition to experimental diagnosis of the discharge properties, in Chapter 5 and 6, a spatially-averaged global model is developed to characterize and predict the behavior of the discharge species under low pressure conditions (no more than a few mTorr). Chapter 5 describes the theory of the global model applied to a compact ECR plasma source. Consideration of the magnetic confinement in the discharge chamber and the species reactions in argon, hydrogen, and argon-hydrogen mixture are made in the model. The model considers two basic equations including charged particle balance and power balance. Chapter 6 presents the modeling results and their comparison with some of the experimental data presented in Chapter 4. Finally, Chapter 7 concludes this work with a summary of the important results and suggestions for future research.

CHAPTER 2

High Density Plasma Sources in Material Processing and their Modeling

2.1 Introduction

Plasma-aided manufacturing has proven to be an effective and efficient processing method in a vast range of industrial applications including thin-film sputter deposition, plasma polymerization, microcircuit fabrication, welding, tool hardening, arc melting, synthesis of pure, ultrafine powders, plasma spraying, plasma sintering, and microwave generation [9]. Of particular interest in this work is its applications in the deposition and etching of thin films for the fabrication of semiconductor microelectronic devices. The continuous demand for smaller device features requires a high density plasma source for a fast processing rate that also operates at a low pressure to obtain small device dimensions and prevent possible damage on the wafer. This chapter describes some of the high density plasma sources which are commonly used as etching and deposition tools. The modeling and simulation of these sources are later introduced.

2.2 Rf Powered High Density Plasma Sources

In this section, three high density plasma sources which utilize rf power coupling to the plasma will be briefly introduced and some of their applications to material processing will also be discussed. The three rf plasma sources presented include the planar inductively coupled plasma source, helical resonator plasma source and the helicon plasma source. The helicon sources require a dc magnetic field for efficient power coupling, but the excitation of inductive coupled plasma sources and helical resonant sources requires no magnetic field.

2.2.1 Planar Inductively Coupled Plasma Sources

A schematic of a typical planar inductive coupled plasma (ICP) source is shown in Fig. 2.1. It consists of a cylindrical discharge region with a diameter similar or larger than its length. The reason for having such a geometry is the design requirement to have a large area and uniform density plasma source for material surface processing in industry. The induction planar coil is a flat spiral and usually placed on top of the vacuum chamber. The coil is separated from the plasma source by a dielectric window in order to prevent possible metallic contamination from the coil. This is especially important during semiconductor microelectronic circuit processing. The dielectric window is typically made of quartz or alumina. Multipole permanent magnets can be used around the process chamber circumference to increase the radial plasma uniformity. This source type was developed initially for rapid, high efficiency sample etching, because the ion densities are about two orders of magnitude higher than in conventional rf parallel plate discharges [22],[23]. ICP also provides independent control of discharge power and substrate bias

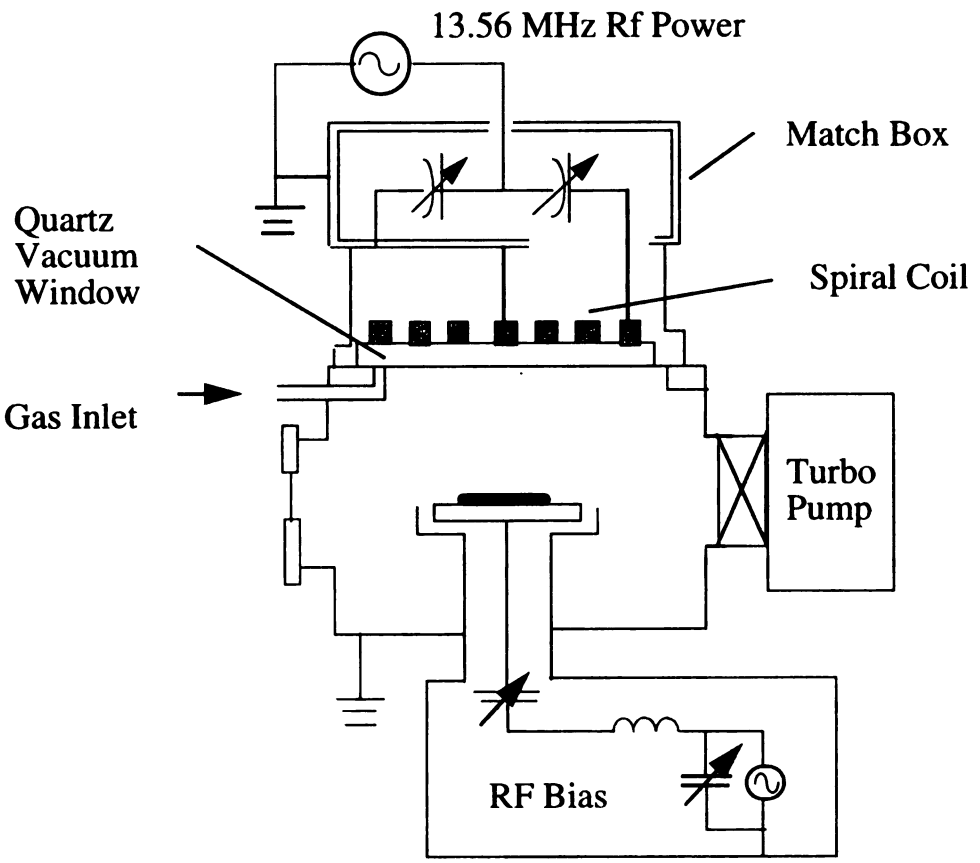

Figure 2.1 Schematic of a planar inductively coupled plasma source with an independent rf biased substrate for material processing.

voltage. Substrates are placed on a rf (13.56 MHz) driven electrode which is used to control the ion bombardment energy.

Inductively coupled plasma sources are being applied to a wide range of applications. An example of one such application is DLC thin film growth using a rf inductively coupled plasma (RFICP) source operating with an argon and methane gas mixture discharge as described by Pappas and Hopwood [21]. The typical processing pressure was around 10 mTorr.

2.2.2 Helical Resonator Plasma Sources

A typical helical resonator is shown in Fig. 2.2. The source consists of a helix coil connected to a rf power (3-30 MHz). The coil is wrapped around the quartz tube inside which the plasma is generated. The entire source is covered by a grounded metallic cylinder to shield the rf energy. An rf matching network is located externally to adjust for different plasma load impedance matching. This structure becomes resonant when the length of the helix approximately equals to an integral number of quarter wavelengths of the rf field [10]. The electromagnetic field within the helical resonator can sustain a plasma with low match loss at low gas pressures. The quartz tube is connected with the processing chamber near where the substrate is located. The substrate can also be biased with rf power to independently control the ion energy bombarding the substrate.

J. M. Cook et al. [11] used the helical resonator structure operated at radio frequencies for submicron polysilicon etching in Cl_2 plasmas at low pressures ($< 10^{-3}$ Torr). With 1% of O_2 added to the Cl_2 plasma and 75 W of the input resonator power, a polysilicon etch

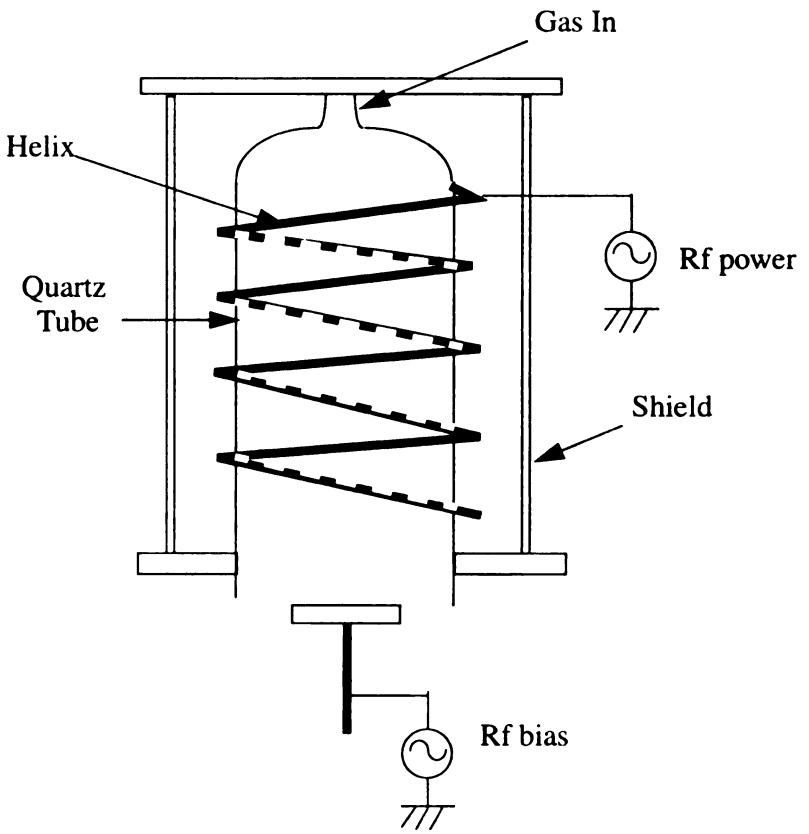

Figure 2.2 Schematic of a helical resonator plasma source

rate

The

acc

con

2.2

197

elec

proc

freq

used

proc

typi

shou

and

(

was

pow

magn

optim

the e

rate of 16.2 nm/min was obtained with good material selectivity over SiO_2/photoresist. The etch rate can be increased considerably by scaling the size of the resonator to accommodate larger diameter discharge tubes and by adding an axial magnetic field confinement [12].

2.2.3 Helicon Plasma Sources

Helicon generation of plasmas in high efficiency was first employed by Boswell in 1970 [13]. The study of Chen in 1985 [14] and subsequently in 1991 [15] suggested that electrons accelerated by the Landau/collisionless damping mechanism can be used to produce primary electrons at the optimum energy for ionization. The typically driving rf frequency for this high density plasma source is 1-50 MHz, with 13.56 MHz commonly used for processing discharges. The magnetic fields vary from 20 to 200 Gauss for processing discharges. Plasma densities range from 10^{11}-10^{14} cm^{-3}, with 10^{11}-10^{12} cm^{-3} typical for processing. For a more detailed study of the helicon discharges, the reader should refer to the research work conducted by Boswell et al. [16][17], Chen et al. [18], and Shoji et al. [19].

Characteristics of the helicon wave plasma employing Cl_2 gas for aluminum etching was studied by Jiwari et al. [20] using a m = 0 mode antenna powered with a 13.56 MHz rf power. A schematic illustration of the experimental apparatus is shown in Fig. 2.3. The magnetic field at the quartz tube was 50 G and at the reactor was varied to establish an optimum condition. A wafer stage was installed in the reactor at a distance of 10 cm from the edge of the quartz tube. The stage was biased negatively by an rf power supply of 100

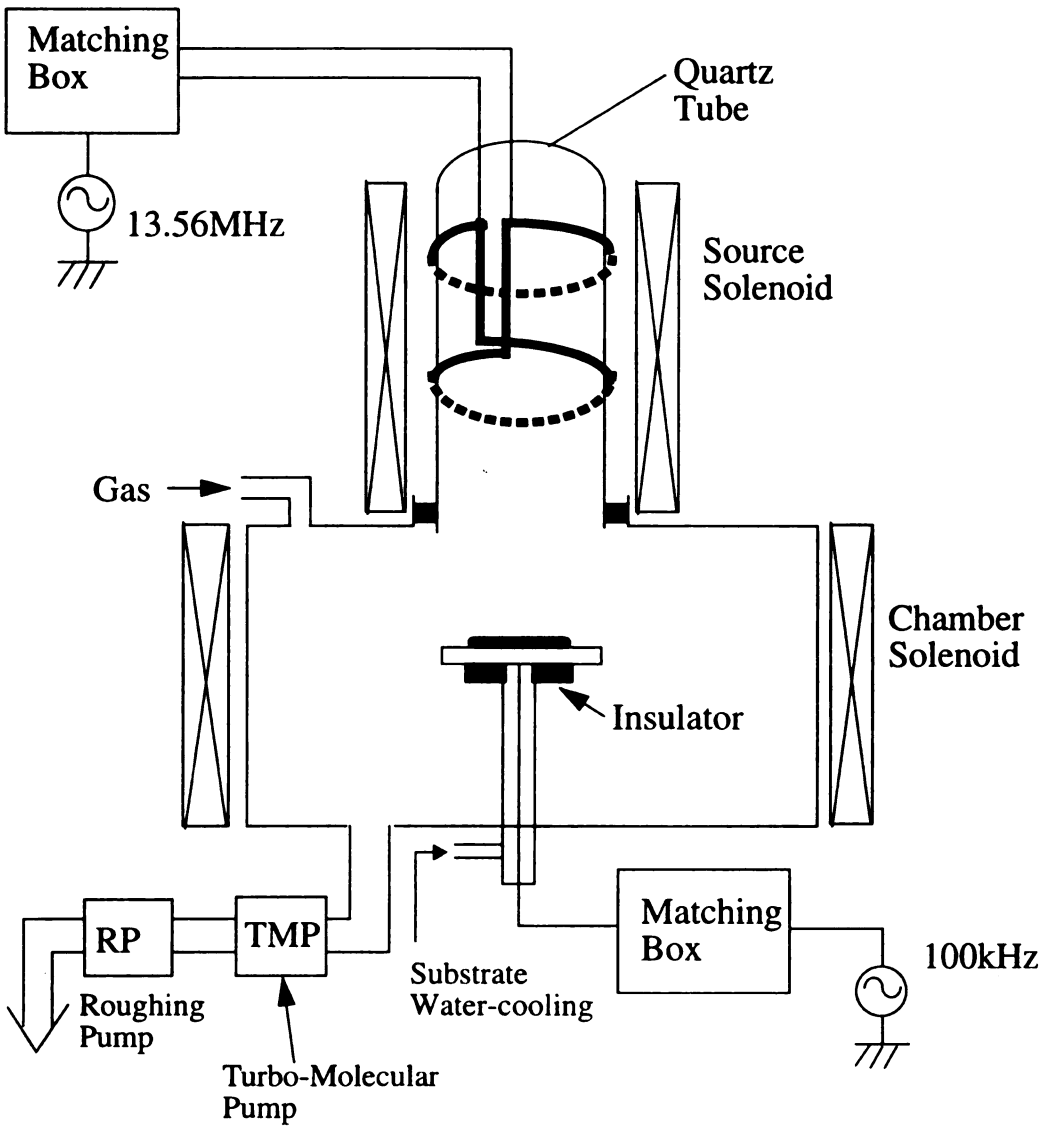

Figure 2.3 Schematic illustration of a helicon wave plasma source [20].

2.3

T

freq.

where

electr

inten

ECR

(DEC

2.3.1

In

semic

then, t

deposit

of ECR

kHz and cooled by water. The typical etching condition were 2 mTorr, 1200W Rf power, and 200 V bias. The electron density, electron temperature, and ion saturation current in the Cl_2 plasma at 2 mTorr were $5x10^{10}$ cm^{-3}, 5.5 eV, and 15 mA/cm^2.

2.3 Microwave ECR Plasma Sources

The electron cyclotron resonance (ECR) condition occurs when the excitation wave frequency ω equals the electron cyclotron frequency ω_{ce} in a static magnetic field.

$$\omega = \omega_{ce} = \frac{eB}{m_e} \tag{2.1}$$

where B is the magnetic field intensity, $e = 1.6x10^{-19}$ coul, and $m_e = 9.11x10^{-31}$ kg is the electron mass. For an microwave frequency of f = 2.45 GHz, the required magnetic field intensity is approximately 875 Gauss. This section introduces three types of microwave ECR plasma sources including the divergent field ECR source, the distributed ECR (DECR) source and the microwave plasma disk reactor (MPDR) source.

2.3.1 Divergent-Field ECR Plasma Sources

In the 1970's, Musil [25] and Suzuki [24] conducted the pioneering works for semiconductor deposition and etching utilizing divergent field ECR plasma sources. Since then, the research work regarding the source operation and applications on thin film deposition and etching became widespread [26]-[29]. Here a brief description of this type of ECR plasma sources is presented.

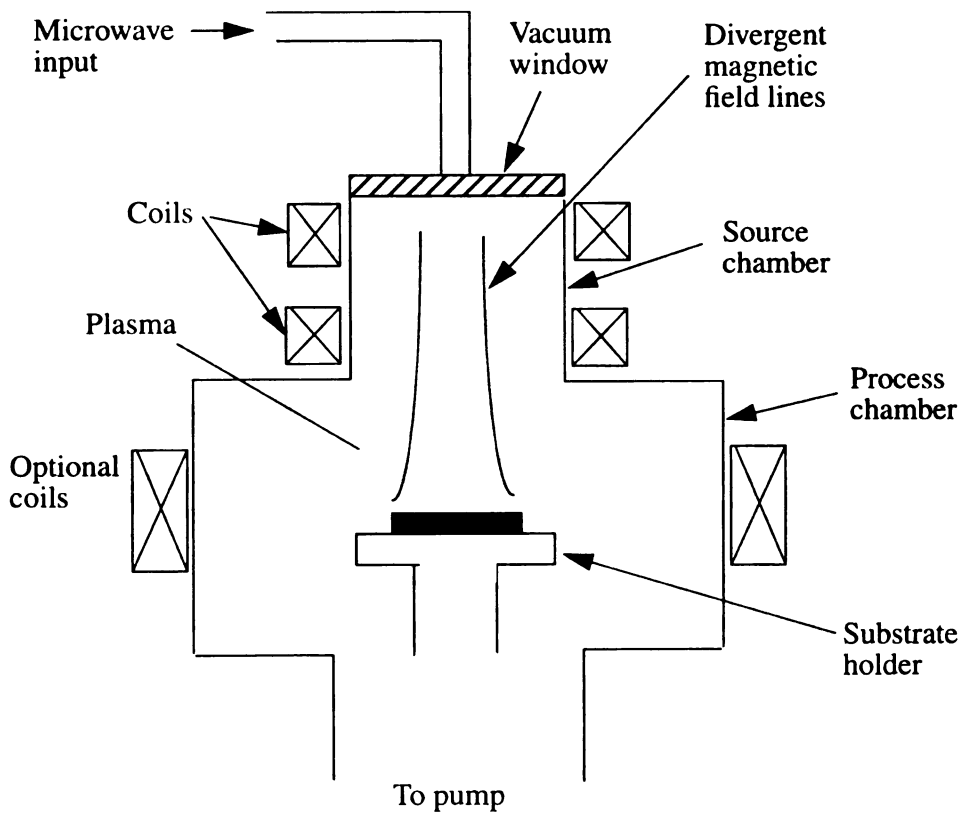

Figure 2.4 Divergent field ECR plasma source

A typical divergent field ECR processing source is shown in Fig. 2.4. The system isoften divided into a source region, where most of the plasma is created, and a process chamber where the substrate is located. A steady magnetic field is generated by one, or more electromagnets surrounding the source chamber. The magnetic field is typically 1000 Gauss or more in the source chamber and tapers off to tens or hundreds of gauss in the process chamber as the field lines diverge to larger radii in the process chamber.

Microwaves are introduced into the source chamber through a dielectric vacuum window (usually quartz or alumina) by a coupling structure. The typical microwave circuit is shown in Fig. 2.5 [30]. It consists a microwave source (2.45 GHz usually), a ferrite microwave circulator to protect the source by shunting the reflected power to a dummy load, a reflected power monitor, tuning stubs, and the plasma coupler. The reflected microwave is sampled through a directional coupler and converted to a DC signal, and then connected to a power meter. Three tuning stubs allow adjustment of the impedance to match the plasma load. When the plasma is generated, electrons and ions diffuse along the magnetic field lines that diverge as moving to the process chamber. Additional coils are sometimes placed around the process chamber to create converging field lines which help confine the charged particles in the process chamber where the substrate is located. This arrangement also helps control the ions incident angle on the substrate which is important for anisotropic etching.

One drawback of conventional divergent field ECR reactors is the use of electromagnets with their associated costs of coils, power supplies, power, and cooling. The development of ECR sources using permanent magnets to produce the required field strength for ECR is aimed to solve this problem [31],[32]. Mantei et. al. reported an ECR

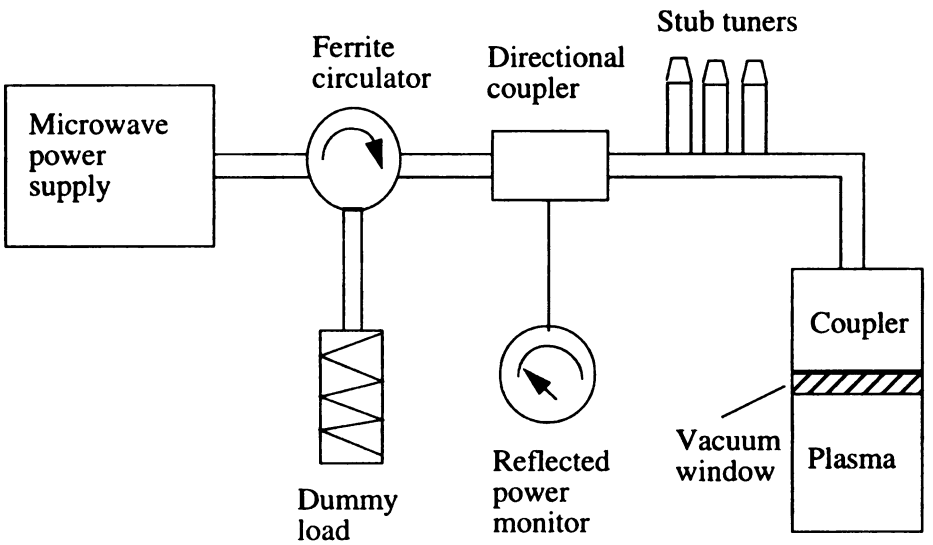

Figure 2.5 The microwave circuit of an ECR plasma source.

per

ma

ma

pov

mic

cha

2x1

2.3

ratio

Furt

mat

ener

mul

eme

mult

875

the p

F

reacte

place

Perma

permanent magnets located behind the microwave window to produce a divergent magnetic field. They used a 15 x 15 x 9 cm, 18 kg block Nd-Fe-B magnet to generate a magnetic field which falls to 875 G at a distance of 8 cm from the magnet face. Microwave power is applied from the side into the space between the magnetic face and the microwave window. Plasma uniformity was improved by surrounding the process chamber with an additional permanent magnet bucket. Plasma densities greater than $2x10^{11}$ cm^{-3} in an argon discharge at 500 W and 1 mTorr were achieved.

2.3.2 Distributed ECR Plasma Sources (DECR)

In a common ECR microwave sustained discharge, the plasma density is limited by the ratio of the surface area of the source to the volume of the reactor into which it diffuses. Furthermore, this type of source has the drawback that conducting or semiconducting materials can get deposited on the dielectric window which transmits the microwave energy into the discharge. To solve these problems, a new reactor concept, based on a multipolar magnetic field confinement structure, termed distributed ECR (DECR) [33] emerged. This new design allows integration of the microwave field applicator to the multipolar magnetic confinement structure such that the ECR conditions (approximately 875 G at a 2.45 GHz excitation frequency) are met. Such a scheme permits one to adjust the plasma source dimension to the required plasma size.

Fig. 2.6 is a schematic representation of the microwave field applicator in a cylindrical reactor. It consists of a linear conductor of cylindrical cross-section, called the antenna, placed a few millimeters above the ground-plane constituted by the reactor wall. Permanent magnets are arranged in a similar way as for classical multipolar magnetic field

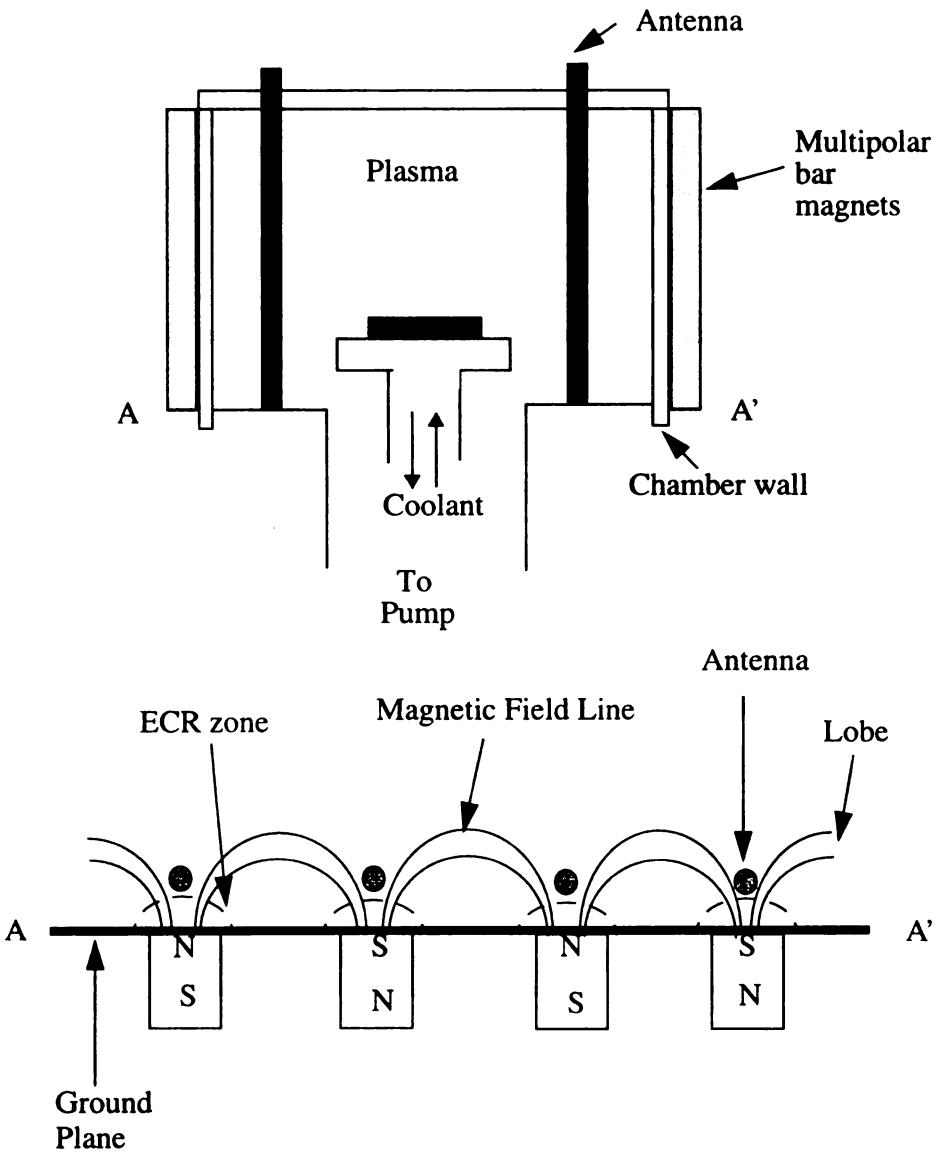

Figure 2.6 Distributed ECR plasma source (DECR).

confinement. These magnets provide the required 875 G (the ECR condition at a 2.45 GHz excitation frequency) isomagnetic surface in the vicinity of the antenna along its entire length. The magnetic field is closed by two adjacent magnet rows as in a conventional multipolar field. A magnetic field configuration is thus created whereby a microwave field, applied at 2.45 GHz through a coaxial feedthrough, results in ECR coupling along the full antenna length. The gas is ionized by electrons in the lobes and the produced plasma then diffuses to the center of the chamber.

The DECR plasma source can be easily scaled up by increasing the number of antenna-magnet bar pairs. However the direct exposure of antennas to the discharge may cause possible contamination from sputtering antenna material during reactive etching processes. During the deposition processes, the antennas can also be deposited with non-conducting material on their surfaces, causing abnormal operation. In addition, in the presence of plasma, microwaves cannot propagate along the antennas without absorption, and this may lead to a non-uniformity of the plasma along the axial direction.

2.3.3 Microwave Plasma Disk Reactor

Similar to the DECR system described previously, the microwave plasma disk reactor (MPDR) uses a multipolar magnet configuration surrounding the discharge region. Rather than using a discrete wave applicator for each magnetic cusp, the MPDR uses a resonant cavity applicator allowing electromagnetic resonance in a single mode. Fig. 2.7 shows an example of an MPDR utilized in the processing of material. The system has a cavity with a sliding short for an adjustable cavity length and a tunable microwave coupling probe which allows the impedance matching of the source with the plasma load and enables

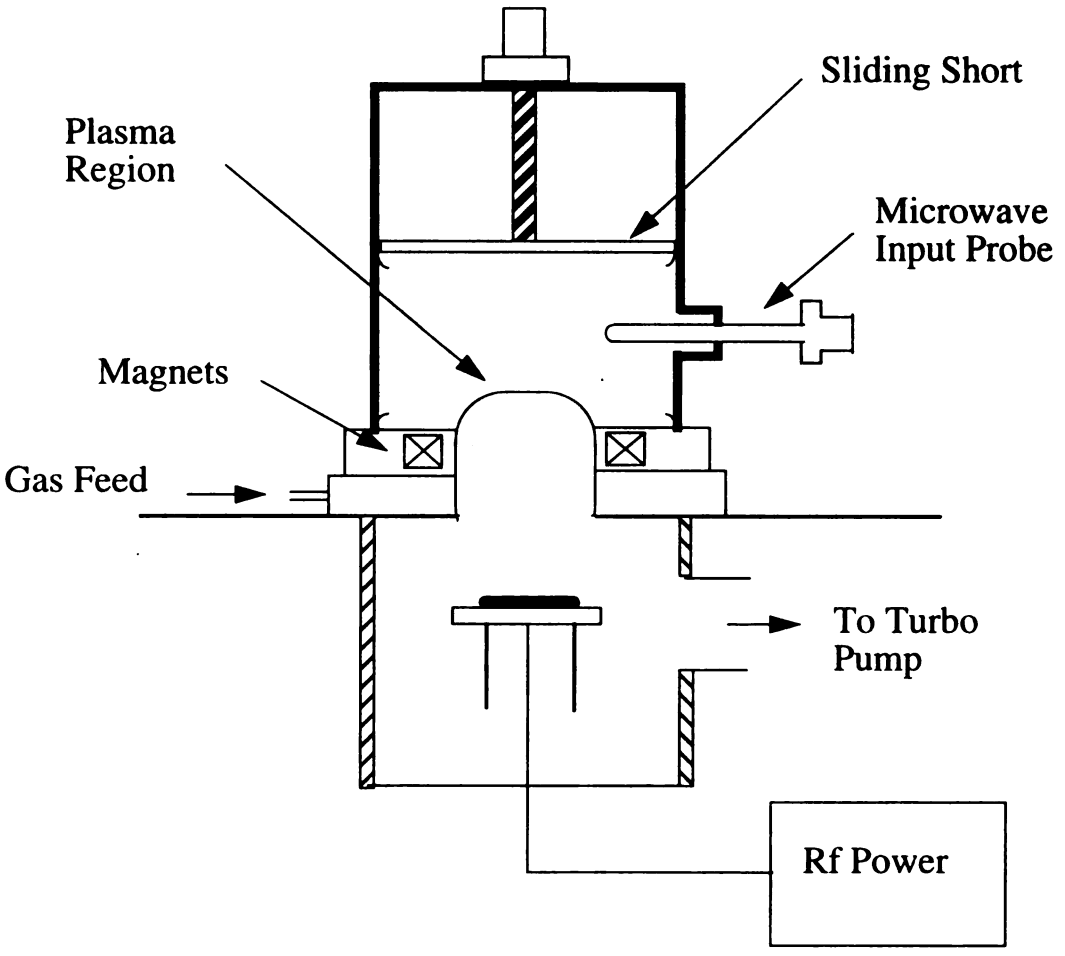

Figure 2.7 An example of the MPDR system

efficient power coupling to the plasma. The cylindrical bell jar surrounded by multipolar magnets and located in the lower end of the cavity is the plasma generation region. This type of applicator enables specific and prechosen electromagnetic modes to be impressed and efficiently coupled into the discharge chamber. The resonant cavity facilitates simple discharge ignition, and by length and microwave coupling probe tuning of the cavity, it produces rapid automatic impedance matching of the plasma machine as the process variables are changed [34],[35]. The MPDR is capable of matching microwave power into disk or cylindrical discharge volumes over pressure regimes of sub mTorr to over 300 Torr [36]. The processing wafer stage is located in the downstream region away from the strong magnetic field. Rf power maybe applied on the substrate to provide a substrate bias. The investigated plasma source performance of the MPDR 610 generated plasma source is studied in this thesis. A more detail description of this low pressure ECR plasma source and its applications is given in Chapter 4 of this thesis.

2.4 Plasma Modeling and Simulation Methods

There are a variety of discharge models in a number of papers in the literature ranging from zero-dimensional global models to two and three-dimensional models. In general, a zero-dimensional global model assumes a uniform steady state plasma and solves the plasma parameters by considering two basic equations: (1) charged particle conservation, i.e., the number of ions created in the plasma by collisions is equal to the loss of ions by diffusion to the wall, and (2) the power absorbed by the electrons must be equal to the power loss from the electron gas by electron-neutral collisions, inelastic and elastic ion-

neutral collisions, and the loss of electron and ion kinetic energies as they recombine on the wall. The global model assumes a Maxwellian electron energy distribution described by a temperature of T_e and the electron collision rates are constants in the plasma volume. In addition, at the low pressures of this study, the electron-ion recombination occurs only at the walls and is absent in the plasma volume. A detail description of this global model can be seen in Ref. [51] and the model is further described in Chapter 5 of this thesis.

M. Meyyappan and T. R. Govindan developed a model to predict the spatially-averaged plasma characteristics of ECR reactors [37]. The model consists of global conservation equations for species concentration, electron density and energy. A gas balance is used to predict the neutral temperature self-consistently. The model provides the global plasma characteristics as a function of system variables in a very efficient manner and can be used in a sensitivity study to identify the contribution of various reactions to the overall system behavior.

Other than the global model which solves a uniform zero-dimensional plasma, a numerical simulation model considers at least one-dimensional variation of the particle densities in the discharge. One method to deal with the properties of the processing discharges is by means of fluid simulation, in which each of the charged particle species (electrons, and positive and negative ions) is treated as a separate fluid, characterized by its temporally and spatially varying density, average velocity, and average energy. A fundamental assumption in this model is that the particle distribution functions of the various species are known. They are usually taken to be drifting Maxwellians.

Examples of applying the fluid model in plasma simulation are briefly described below. A one-dimensional fluid model of the microwave ECR discharge, which includes

the inhomogeneity effects of the external magnetic field, was developed by N. S. Yoon et al. [38]. For the efficiency of the simulation, the plasma body and the sheath regions were separately modeled. For the argon discharge, various quantities such as the axial profiles of plasma density, electron temperature, and microwave power deposition were obtained. Another simulation is of low pressure inductive plasma sources using a time averaged two-dimensional fluid model including an electromagnetic module with self-consistent power deposition [39]. Comparison with the experiment and previous simulation results showed that the fluid model is feasible in a certain range of gas pressure. D. P. Lymberopoulos et al. studied the two-dimensional fluid simulation of polysilicon etching with chlorine in an inductively-coupled high density plasma source [40]. The complex plasma chemical reactions (involving electrons, ions, and neutrals) as well as surface chemistry were included in the simulation. Quantities such as power deposition, species density and flux, and etch rate and uniformity were calculated. As power deposition was increased, the electron density increased linearly, the plasma became less electronegative, the degree of gas dissociation increased, and the plasma potential remained constant. The radial uniformity of the Cl atom flux was better than that of the ion flux.

Another numerical simulation used is the particle-in-cell (PIC) model [41],[42]. The Lorentz force on each particle determines its self-consistent motion, and the charges and currents generated by the moving, charged particles determined the self-consistent fields through Maxwell's equations. Monte Carlo techniques are used to determine the short-range collisional process (ionization, scattering, and so on). This technique yields time- and space-resolved information on the charged particle velocity distribution functions in a discharge from which fluxes and generation rates can be calculated.

Surendra et al. [41] used the PIC simulation to study the structure of rf glow discharges in helium. The differences between discharges in which secondary electrons play a key role in sustaining the discharge and those in which secondary electrons are unimportant were examined in three cases which illustrate the importance of the discharge-sustaining mechanisms. Electron energy distribution were found to be, in general, non-Maxwellian. The simulation also indicated that the ion power deposition scaled as the square of the applied voltage, while electron power deposition scaled approximately linearly with applied voltage. Kuo et al. [43] simulated the electron energy distribution (EED) in an ECR microwave discharge via the Monte Carlo technique. The time averaged, spatially dependent EED was computed self-consistently by integrating electron trajectories subjected to the microwave field, the divergent magnetic field, the space charge field, and the sheath field. The electron-electron collisions and collisions with the neutral hydrogen atoms were considered. At low pressures (0.5 mTorr), the EED was spatially independent due to the large electron mean free path.

Other simulations such as the hybrid model used particle ion and fluid electron methods to simulate charged particle behavior in the high density ECR plasmas [44],[45]. N. H. Choi et al. used the one-dimensional hybrid model which included both the ECR electron heating phenomena and the transport of ions along the divergent axial magnetic field lines. Microwave power was considered as an energy flow attenuated by the thermal electron fluid. Electron motions were coupled to the ions through ambipolarity. The results showed a strong effect of the distributed ionization on the ion energy distribution.

The application of global models to the MPDR 610 plasma source with magnetic confinement in the source region for three different gas discharges is considered in this

thesis. Previous modelings of this plasma source include a two-dimensional numerical model using a Monte Carlo particle method coupled with a solution of the Maxwell equations and a three-dimensional electromagnetic particle-in-cell (PIC) model [46]-[48]. The particles in the source move subject to the Lorentz force equation and to the appropriate elastic and inelastic collision processes. The electric fields and time-varying magnetic fields were solved using a finite-difference time-domain (FDTD) technique. The electromagnetic fields and the plasma dynamics were solved in a self-consistent manner. The static magnetic field produced by the permanent magnets, microwave electric fields at 2.45 GHz, microwave power absorption, and electron energy distribution in the source were modeled for argon and helium discharges. The difficulty with these models is the use of small times in the solutions. The time steps are small enough that many of the slower chemical reactions can not be simulated in reasonable simulation times. An alternative is to use global models which allow all the reactions to be included at the expense of not having information on the detailed spatial variations in the plasma source.

3.1

In

a nur

categ

optica

laser

In

used i

Doubl

to esti

electro

employ

utilized

CHAPTER 3

The Experimental Diagnostic Techniques and Theories

3.1 Introduction

In order to understand and analyze the plasma properties during the actual processing, a number of diagnostic techniques have been developed [49]. These techniques can be categorized as intrusive such as Langmuir probe measurements and non-intrusive such as optical emission spectroscopy(OES), actinometry, laser induced fluorescence and infrared laser absorption.

In this chapter, we are going to discuss the plasma diagnostic techniques which were used in this thesis. They include Langmuir probe measurements, OES, and actinometry. Double Langmuir probe (DLP) were used to characterize positive ion concentrations and to estimate the electron temperature. Single Langmuir probe (SLP) were used to obtain electron temperatures and electron energy distribution function (EEDF). OES was employed to measure the electron temperature in the source. Finally, actinometry is utilized to obtain the density of neutral radical species.

3.2 Double Langmuir Probe Measurements

One of the most widely used plasma diagnostic techniques is the measurement of positive ion densities using a double Langmuir probe (DLP). The DLP measurement also provides the electron temperature of the high energy tail of the distribution under the assumption that the electron energy distribution function (EEDF) is Maxwellian.

The set up of the DLP measurement circuit is shown in Figure 3.1. Two probes made of tungsten are covered by a pyrex tube on the outside to isolate all but the probe tips from the plasma source. Each probe tip has a diameter of 0.11 cm and a length of 0.64 cm. The entire circuit is electrically floated. A dc voltage is applied between the two probes. The output of the DC voltage supply and the current reading from the multimeter are sent to the computer through a series connection of GPIB cables for further analysis. The electron temperature and ion density are then determined from the I-V characteristics curve of the probe.

Figure 3.2 shows a typical DLP I-V characteristics generated from the compact plasma source, MPDR610. The applied voltage on the probe is from -50V to +50V. When the applied voltage between the electrodes are zero, both the probes collect equal amount of electrons and ions. Hence the current in the circuit is zero. When there is a potential difference between the two probes, the more negative one will begin to repel electrons and collect more ions. While the other probe (more positive one) will collect more electrons than ions. The current flow will no longer be zero. As the differential potential starts to increase, the current flow will also increase and eventually the more negative probe will draw the ion saturation current, which is balanced by the net electron current drawn

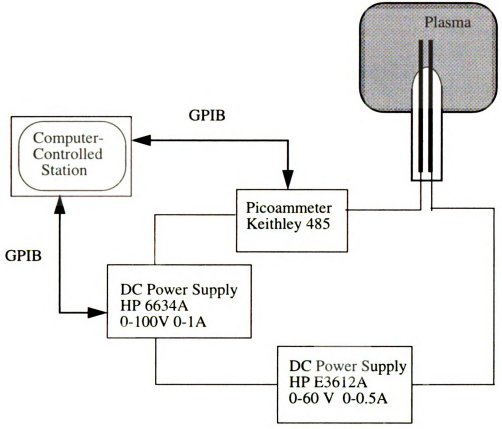

Figure 3.1 Double Langmuir Probe Circuit

hen

distr

T

prob

In ter

Assu

the e

wher

prob

Poter

and

If A

to the other probe. Notice that the net current never exceeds the ion saturation current, and hence the electron current collected will be only from the high energy tail of the electron distribution.

The theory of the DLP is explained as follows [51]. The ion and electron currents to probes 1 and 2 are defined as I_{i1}, I_{e1} and I_{i2} , I_{e2}. The condition that the circuit float is

$$I_{i1} + I_{i2} - I_{e1} - I_{e2} = 0 \tag{3.1}$$

In terms of net current in the loop *I*, Eqn. (3.1) can be rearranged as

$$I_{e1} - I_{i1} = I_{i2} - I_{e2} = I \tag{3.2}$$

Assuming a Maxwellian distribution of electron energy, and from Boltzmann's relation, the electron current can be expressed as

$$I_{e1} = A_1 J_1 e^{V_1/T_e} \text{ and} \tag{3.3}$$

$$I_{e2} = A_2 J_2 e^{V_2/T_e} \tag{3.4}$$

where J_1 and J_2 are electron random current densities to the probes, A_1 and A_2 are the probe collecting areas, and V_1 and V_2 are the probe potentials with respect to the plasma potential. Note that the electron temperature T_e here is expressed in eV. Using $V=V_1-V_2$ and substituting Eqns.(3.3), (3.4) into Eqn.(3.2), we have

$$\frac{I + I_{i1}}{I_{i2} - I} = \frac{A_1}{A_2} e^{V/T_e} \tag{3.5}$$

If $A_1=A_2$, then $I_{i1} = I_{i2} = I_i$. Eqn. (3.5) can be simplified to

I (mA)

Fi
condit

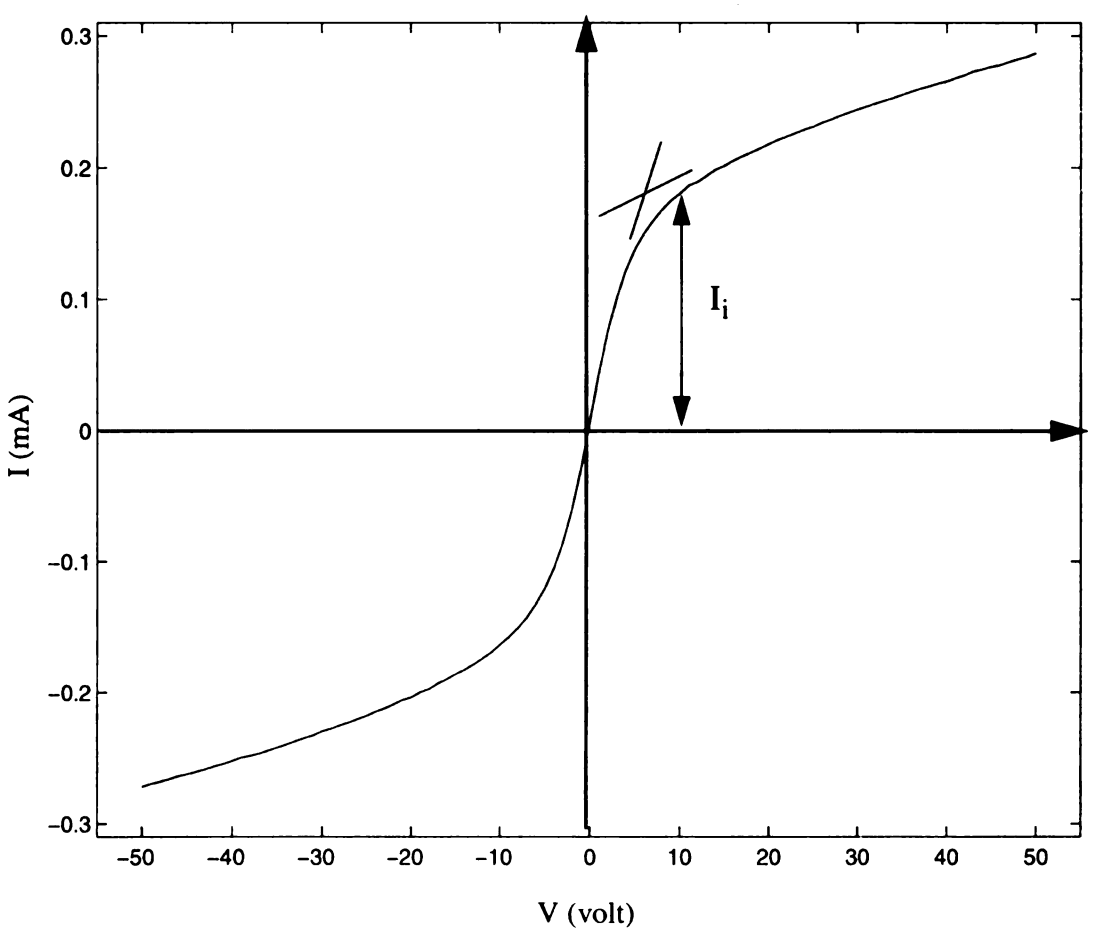

Figure 3.2 A typical I-V characteristic of a double Langmuir probe. Plasma conditions are P_{in} = 90W, 3 mTorr, and flow rate = 8 sccm. The data is collected at 2 cm downstream.

One

deriv

The s

where

tange

the de

where

the ion

probes

Debye

$$I = I_i \frac{e^{V/T_e} - 1}{e^{V/T_e} + 1} \text{ or}$$

$$I = I_i \tanh\left(\frac{V}{2T_e}\right) \tag{3.6}$$

One simpler way to obtain T_e from the experimental I-V characteristic is by taking the derivative of the above equation with respect to V, and we have

$$\frac{dI}{dV} = \frac{I_i}{2T_e}\left(\operatorname{sech}\frac{V}{T_e}\right)^2 \tag{3.7}$$

The slope of the I-V plot at V=0 can then be related to T_e as

$$\left.\frac{dI}{dV}\right|_{V=0} = \frac{I_i}{2T_e} \tag{3.8}$$

where I_i is the ion saturation current and is determined by the intersection point of the tangential lines as shown in Fig. 3.2. Once the electron temperature is determined, from the development of Chen [50], the ion density is related to the ion saturation current (I_i) by

$$I_i = 0.6 n_i e A_p \left(\frac{kT_e}{m_i}\right)^{1/2} \tag{3.9}$$

where n_i is the ion density, e is the electron charge, A_p is the effective probe area, and m_i is the ion mass. The effective probe area represents the increased ion collecting area of the probes due to the plasma sheath. It is approximated by the actual probe dimension plus the Debye length, λ_D, where

$$\lambda_D = 69\sqrt{T_e/n_e} \text{ (m)} \tag{3.10}$$

which is also a function of plasma density and electron temperature. Thus several iterations between Eqn's. (3.9) and (3.10) were applied in the probe I-V characteristics analyzing computer program. The termination of the iteration is set whenever the new plasma density falls within 1% of the previous one.

3.3 Single Langmuir Probe Measurements

In an ECR discharge, electrons gain energy from the electromagnetic field through ECR excitation or through ohmic collisional heating. The electrons then lose their energies by collisions with ions, neutrals, and the wall. Since the electron impact excitation is the major source of reactive species in low pressure plasmas, it is important to understand the distribution of electron energy.

In 1930, Druyvesteyn [52] showed that the EEDF is proportional to the second derivative of the I-V characteristic of a single Langmuir probe in the region where the applied voltage is below the plasma potential:

$$f(E) \propto \sqrt{V_p - V}\frac{d^2 I_e}{dV^2} \tag{3.11}$$

where V_p is the plasma potential, V is the voltage applied to the probe, I_e is the electron current drawn by the probe, and $E = V_p - V$. The second derivative is approximated with d^2I/dV^2 where I is the total probe current and it equals to the sum of I_e and ion currents drawn to the probe. This approximation is justified if the applied voltage on the probe is less than V_p in the regions where the ion currents have small variations.

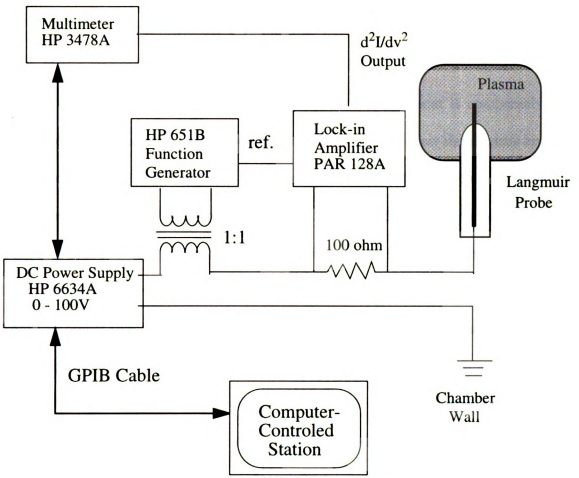

Figure 3.3 Single Langmuir Probe Circuit Set Up.

The plasma potential adopted in this thesis is from the conventional definition in Ref. [53],[54] which is taken to be the voltage where the maximum of the second derivative of the Langmuir probe I-V characteristic occurs. The EEDF, f(E), is normalized according to

$$\int_0^\infty f(E)dE = 1 \tag{3.12}$$

The set up of the single Langmuir probe (SLP) measurement is comparably more complicated than that of the DLP circuit. And the result shows how the electron energy is actually distributed instead of the assumption of Maxwellian distribution used in the DLP measurements. Figure 3.3 shows the set up circuit for SLP measurements. A single Langmuir probe of a tungsten wire protruding from a pyrex tube is inserted in the plasma. It has a cylindrical electron current collecting area of 1.1 mm in diameter and 6.3 mm in length. A power supply with a GPIB interface is used to provide computer control of the sweeping DC voltage applied to the probe. The output of the dc power supply is varied from -15 to 20 volts with a step voltage of 0.5 volts. A small sine wave with a frequency of 1 kHz and amplitude of no more than 0.5 volts is superimposed on the DC probe voltage through a transformer. This will produce a probe current that has both DC and AC components:

$$\mathrm{I=I\{V+a(\sin \omega t)\}} \tag{3.13}$$

Expanding this function as a Taylor series, we have

$$I = \left[I(V) + \frac{a^2}{4}\frac{d^2I}{dV^2} + \frac{a^4}{64}\frac{d^4I}{dV^4} + \ldots \right] + \Delta I_{ac1} + \Delta I_{ac2} + \text{higher order harmonics} \tag{3.14}$$

where

$$\Delta I_{ac1} = \left[a\frac{dI}{dV} + \frac{a^3}{8}\frac{d^3I}{dV^3} + \ldots \right] \sin\omega t \tag{3.15}$$

$$\Delta I_{ac2} = \left[\frac{a^2}{4}\frac{d^2I}{dV^2} + \frac{a^4}{48}\frac{d^4I}{dV^4} + \ldots \right] (-\cos 2\omega t) \tag{3.16}$$

are the first and second harmonic terms. The second harmonic current is proportional to the second derivative $d^2I(V)/dV^2$ if the amplitude of the AC signal is small enough compared to the DC value and the interference from the higher order differential terms is minimal. Therefore those terms can be ignored without considerable error.

A Princeton Applied Research (PAR-128A) lock-in amplifier referenced with the oscillator frequency differentially measures the voltage across a current-sampling resistor with its input locked on twice the oscillator frequency. The filtered output of the lock-in amplifier which is proportional to d^2I/dV^2 at the applied DC potential is sent to the multimeter. Both the readings from the multimeter and DC power supply are recorded by the computer through the GPIB bus for later analysis. Note that the entire probe circuit is grounded at the processing chamber wall to provide a loop for electron current drawn from the probe. Another computer program is used to modify the raw data taken from the probe measurement and generate a plot of EEDF with normalization according to Eqn.(3.11). The average of the electron temperature is then calculated from the EEDF using:

$$\langle E \rangle = \int_0^\infty Ef(E)dE \tag{3.17}$$

3.4 Optical Emission Spectroscopy

Both the SLP and the DLP methods are intrusive techniques and hence they are difficult to apply and interpret within the plasma source where the static magnetic fields are present. Within the source region, optical emission spectroscopy (OES) may serve as a more appropriate technique in plasma diagnosis. The set up of OES adopted in this thesis is shown in Fig. 3.4.

3.4.1 Measurements for T_e

The first OES technique applied in this thesis for measuring the electron temperature is by using the emission spectrum originating from a range of excited state energy levels of noble gases including argon, krypton, and xenon [55]. A small amount (less than 5%) of these noble gases are added to the discharge using a second gas flow channel on the plasma source system. The spectra of emission across the range from 750 nm to 850 nm from the source region is then recorded with a ORIEL 1/4 m monochromator (Model 77100) which has self-scanning photodiode arrays for light detecting. The associated threshold energies of the excited states observed range from 9.82 eV to 13.5 eV. A total of 19 emission lines were observed in this study. A list of the transitions with their associated branching ratios, threshold energies, and electron excitation cross sections are

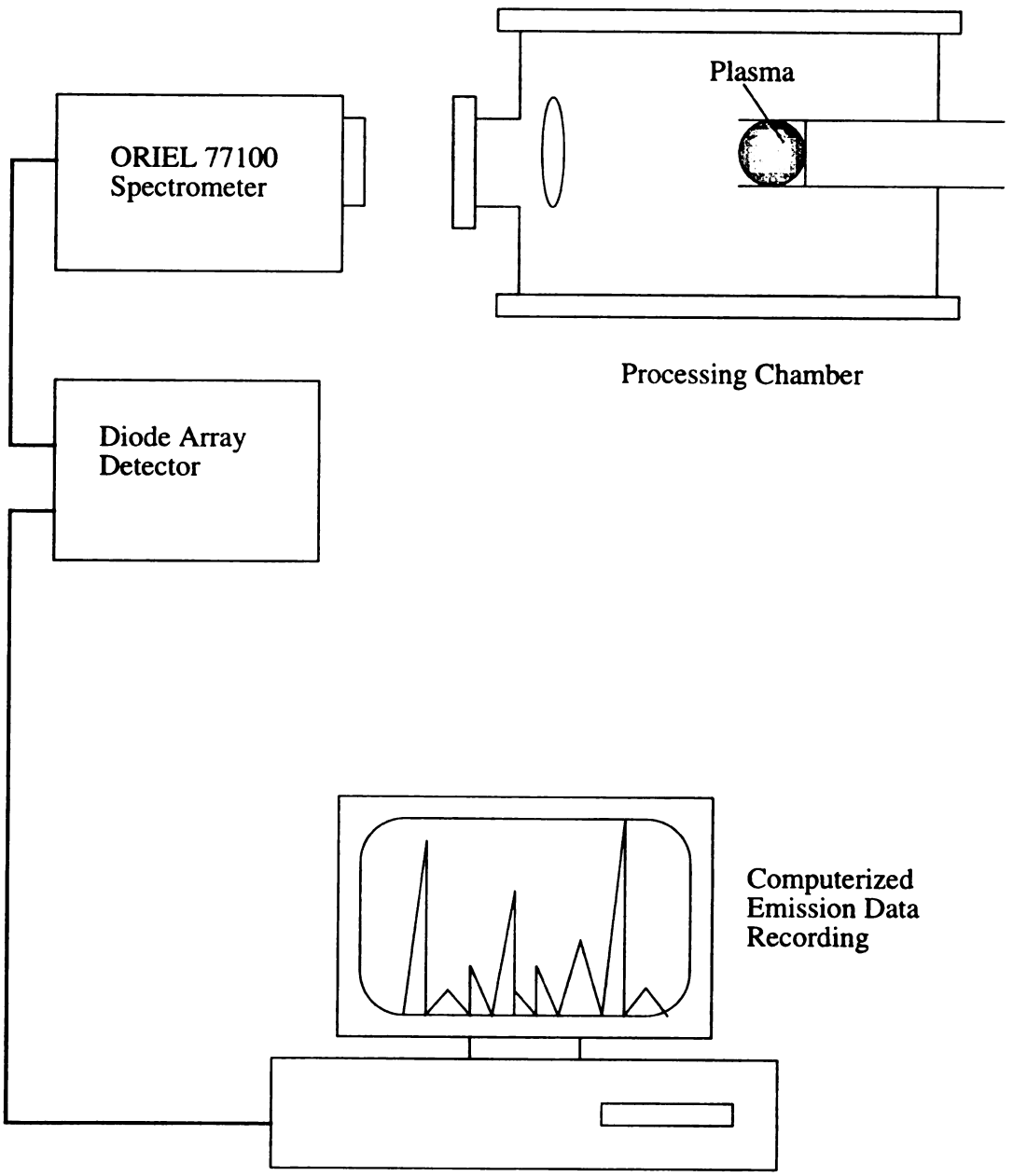

Figure 3.4 The set up for OES

summarized in Table 3.1.

To determine the electron temperature, the expected emission intensities are calculated at each experimentally observed wavelength for various electron temperatures. The assumption is made in this study that the population of the emitting states come mostly

Table 3.1 The cross section data, branching ratios, threshold energies of the observed transitions [63]-[65] and the spectrometer correction factors.

Gas	$\lambda_{j,k}$ (nm)	$b_{j,k}$	E_{th} (eV)	E_{max}	σ_{max} ($x10^{-19}$ cm^2)	Q
Ar	750.4	1.0	13.5	21.0	114	.6289
Ar	751.4	1.0	13.3	23.0	48	.6325
Ar	763.5	0.41	13.2	23.0	132	.6850
Ar	842.4	0.55	13.1	23.5	202	1.3751
Ar	811.5	1.0	13.1	22.0	195	1.0506
Kr	768.5	1.0	12.3	20.5	20	.7167
Kr	826.3	0.94	12.2	21.0	109	1.1734
Kr	785.5	0.55	12.1	20.5	51	.8282
Kr	806.0	0.38	12.1	19.5	76	1.0161
Kr	850.9	0.62	12.1	19.5	76	1.4596
Kr	758.7	1.0	11.7	20.0	88	.6621
Kr	760.1	0.57	11.5	20.0	160	.6693
Kr	819.0	0.43	11.5	20.0	160	1.1225
Kr	769.5	0.13	11.5	20.5	124	.7204
Kr	829.8	0.87	11.5	20.5	124	1.2003
Kr	810.4	0.25	11.4	20.0	215	1.0496
Kr	877.7	0.75	11.4	20.0	215	1.6249
Kr	811.3	1.0	11.4	20.0	108	1.0506
Xe	834.7	0.97	11.06	18.0	33	1.2829
Xe	828.0	1.0	9.94	27.0	83	1.1905
Xe	823.1	0.62	9.82	14.5	96	1.1552

from the ground state excitations instead of from metastable state excitations. This assumption is made based on the electron energy being 4 - 8 eV for the pressure range in this work. The energy range is high enough that extensive excitation occurs directly from the ground state. The intensity of emission at wavelength $\lambda_{j,k}$ accompanying the state transition $A_k \rightarrow A_j$ is given by

$$I_{j,k} = 4\pi Q^{-1}(\lambda_{j,k}) n_g b_{j,k} \int_{v_o}^{\infty} \sigma_{g,k}(v) v^3 f_e(v) dv \tag{3.18}$$

where $Q(\lambda_{j,k})$ is the spectrometer correction factor at $\lambda_{j,k}$, n_g is the radical density at the ground state, $\sigma_{g,k}(v)$ is the effective cross section at electron speed v for electron impact excitation from the ground state g to state k, and v_o is the minimum electron speed for excitation. The determination of the Q's values will be discussed in the following subsection. The branching ratio is denoted as $b_{j,k}$ for transition $A_k \rightarrow A_j$ and it is defined as

$$b_{j,k} = \frac{I_{j,k}}{\Sigma I_k} \tag{3.19}$$

where $I_{j,k}$ is the relative intensity of emissions from state k to state j, and the summation in the denominator represents the allowed transition from state k to all lower states. A Maxwellian electron distribution f_e is assumed in this technique. The electron temperature is found by comparing the calculated emission intensities (I_{cal}) at various assumed electron temperatures to the observed emission intensities (I_{obs}). This comparison is done as a function of the threshold energy (E_{th}) of each of the excitations. First, dividing I_{obs} by I_{cal} and the log of this ratio is plotted versus E_{th}. A least square line is then fitted to these

data [66]. Each fitted line corresponds to an assumed electron temperature. The slopes of these lines in the assumed range of T_e's are then plotted versus T_e. The electron temperature in the source will then be found at zero slope.

3.4.2 Determination of Spectrometer Correction Factors

Although each spectrometer has its own scanning range, the output from the photodetector may not be accurate without considering the spectrometer correction factor. This difference between the measured output and the real spectrum of the incoming light is usually due to the grating and photodetector sensitivity versus wavelength. It is therefore necessary to obtain a correcting factor table for each different spectrometer before taking the spectrum measurements.

The way to obtain the correction factor is stated as follows. A 45W quartz-halogen tungsten lamp (Optronic Lab., Model 245C) with known calibration intensity over a range of wavelengths was used and put in front of the spectrometer that would be used for measurements. During the calibration, the current flow through the lamp was fixed at 6.5 Amps in order to generate constant emissions from the lamp during the calibration process. The outputs from the spectrometer were then recorded over the same wavelength range of the known lamp spectrum (I_{lamp}). Fig. 3.5 plots the spectrum of the tungsten lamp. The summarized measurement results for the ORIEL spectrometer are shown in Table 3.2. Once the measured spectrum ($I_{measured}$) is known, the correction factor, Q can be calculated from

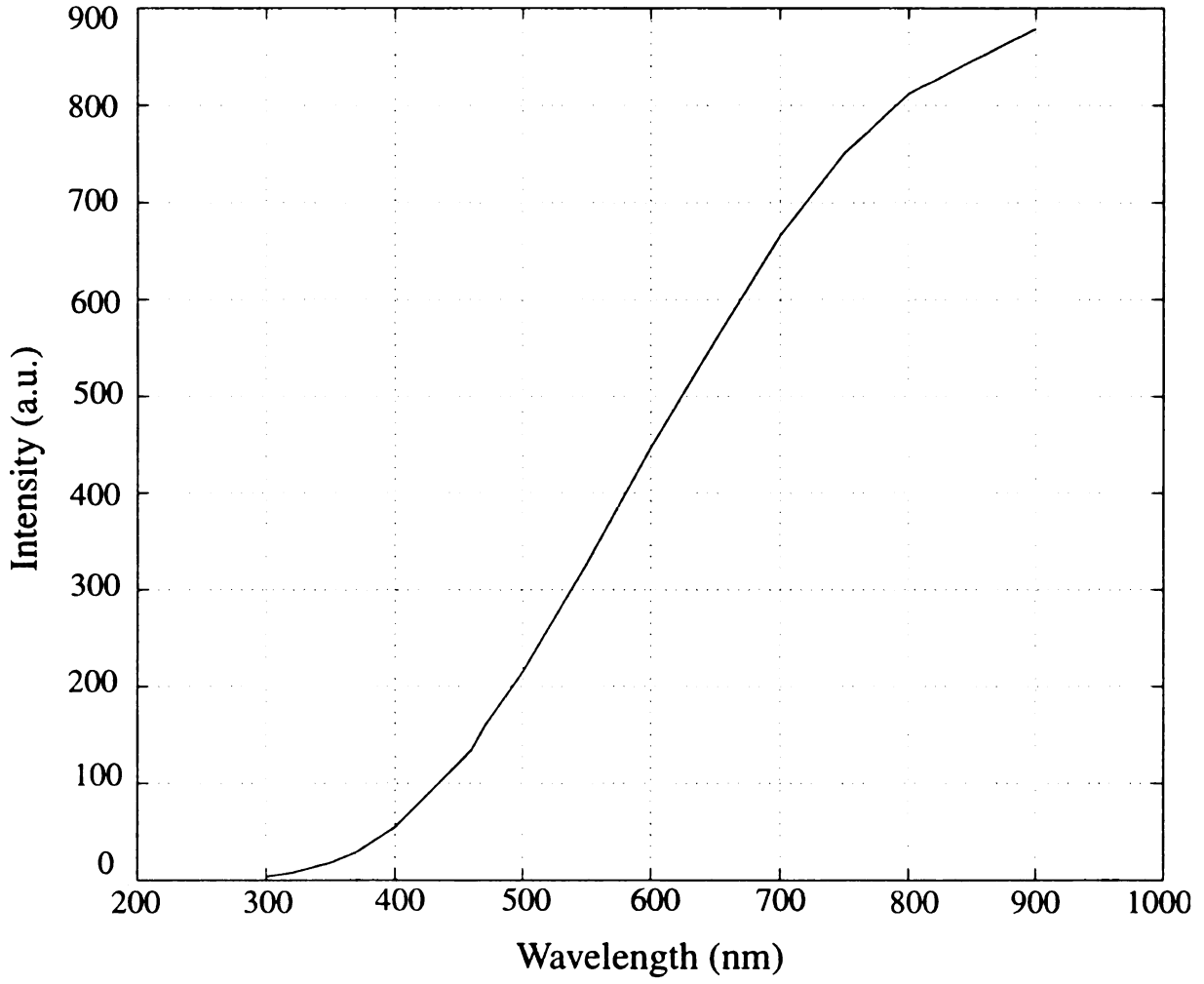

Figure 3.5 The emission spectrum of the tungsten lamp

Table 3.2 The measurement results for the ORIEL spectrometer.

Wavelength (nm)	Intensity	Wavelength (nm)	Intensity
450	419	650	1498
460	448	660	1501
470	501	670	2042
480	525	680	2240
490	566	690	2010
500	595	700	1660
510	620	710	1505
520	710	720	1393
530	782	730	1329
540	900	740	1257
550	983	750	1195
560	1020	760	1136
570	1081	770	1108
580	1026	780	1075
590	1175	790	974
600	1233	800	906
610	1319	810	851
620	1403	820	623
630	1467	830	417
640	1492	840	388

The v

3.4.3

In

many

conce

actino

study.

(1) G

W

emiss

and th

where

$$Q(\lambda) = \frac{I_{lamp}(\lambda)}{I_{measured}(\lambda)} \tag{3.20}$$

The values of Q are seen to be varied for different wavelengths and shown in Table 3.1.

3.4.3 Actinometry

In a hydrogen discharge, hydrogen molecules dissociate into atomic hydrogen and also many different kinds of charged species by inelastic collisions. In order to figure out the concentrations of different species in this relatively complicated discharge, the actinometry technique is applied to find out the relative atomic hydrogen density. In this study, actinometry will be performed in H_2 discharges for neutral density measurements.

(1) General Expression of Actinometry [56,57]

We begin with a general expression of actinometry as follows: the intensity of an emission line may be expressed as

$$I_x \propto \nu_{ex} = N_x\langle v\sigma_{ex}\rangle = N_x\int_{E_{ex}}^{\infty} v\sigma_{ex} f(E)EdE \tag{3.21}$$

and the intensity of an actinometer as

$$I_a \propto \nu_{ea} = N_a\langle v\sigma_{ea}\rangle = N_a\int_{E_{ea}}^{\infty} v\sigma_{ea} f(E)EdE \tag{3.22}$$

where σ is the excitation cross section, N is atomic gas concentration, E_{ex} and E_{ea} are

excitation threshold energies, f(E) is electron energy distribution function, and ν is excitation frequency. Dividing Eqn. (3.21) by Eqn. (3.22), we have

$$\frac{I_x = N_x \int_{E_{ex}}^{\infty} v\sigma_{ex} f(E) E dE}{I_a = N_a \int_{E_{ea}}^{\infty} v\sigma_{ea} f(E) E dE} \tag{3.23}$$

Assuming $\sigma_{ex} \approx \sigma_{ea}$ and $E_{ex} \approx E_{ea}$, then we have

$$\frac{I_x}{I_a} = \frac{N_x}{N_a} \tag{3.24}$$

The criteria of choosing an actinometer is (a) it is relatively inert to the desired species, and (b) the energies of the involved excited states are similar. From Eqn. (3.24) we conclude that the desired atomic species concentration is proportional to the ratio of desired species emission intensity to the actinometer emission intensity.

(2) Modified Actinometry Theory in this Thesis

This modified actinometry technique is used to determine the absolute H-atom concentration in the discharge following the work in [58],[59]. Argon is chosen as the actinometry gas in this study since it satisfies the two criteria mentioned above. The emission lines observed were 750.4 nm for argon (energy level = 13.4 eV) and 486.1 nm for hydrogen (energy level=12.75 eV). As noted in section 3.4.1, the contribution of argon emission at 750.4 nm due to excitation from metastable states is small. Hence only the excitations from ground states are considered in this thesis.

The emission intensity from argon can be expressed as

$$I_{Ar} = Q^{-1}(\lambda_{Ar}) b_{Ar} n_{Ar} \int_{v_{th}}^{\infty} \sigma_{Ar}(v) v f_e(v) 4\pi v^2 dv = \alpha(\lambda_{Ar}) b_{Ar} n_{Ar} K_{Ar} \qquad (3.25)$$

where Q is the spectrometer correction factor at wavelength λ_{Ar}, n_{Ar} is the argon neutral density, b_{Ar} is the argon branching ratio for the line at λ_{Ar} [55], and $\sigma_{Ar}(v)$ is the electron excitation cross-section of argon ground state atoms by electrons of velocity v. A Maxwellian assumption for the electron distribution is assumed and the integral is solved as

$$K_{Ar}(T_e) = \int_{v_{th}}^{\infty} \sigma_{Ar}(v) v f_e(v) 4\pi v^2 dv \qquad (3.26)$$

Next consider the emission from H(486.1 nm)

$$I_{H_\beta} = Q^{-1}(\lambda_{H_\beta}) b_{H_\beta} (n_H K_{H_\beta} + n_{H_2} K_{H_2}) \qquad (3.27)$$

where again a Maxwellian approximation to the electron distribution function is used. n_H is the atomic hydrogen density and n_{H2} is the molecular hydrogen density. $b_{H\beta}$ is the branching ratio for the line at $\lambda_{H\beta}$ [62]. The excitation rate constants $K_{H\beta}$ and K_{H2} are calculated using the same equation as in Eqn. (3.26) by replacing σ_{Ar} with $\sigma_{H\beta}$ and σ_{H2} respectively. Here the cross section data of $\sigma_{H\beta}$ and σ_{H2} are from [60][61]. Here we consider both the direct electron excitation of atomic hydrogen and the dissociative excitation of H_2. The dissociative excitation becomes more important as the electron temperature in the discharge goes higher. The electron temperatures in the source as shown later in Chapter 6 range from 6 to 8 eV. It is found that for electron temperatures in this range the effect of dissociative excitation is not negligible and therefore is included in

Eqn. (3.27). Dividing Eqn. (3.27) by Eqn. (3.25), we have

$$\frac{I_{H_\beta}}{I_{Ar}} = \frac{Q^{-1}(\lambda_{H_\beta})b_{H_\beta}}{Q^{-1}(\lambda_{Ar})b_{Ar}}\left[\frac{n_H K_{H_\beta} + n_{H_2} K_{H_2}}{n_{Ar} K_{Ar}}\right] \tag{3.28}$$

Rearranging this equation gives

$$\frac{n_H}{n_{Ar}} = \frac{K_{Ar}}{K_{H_\beta} b_{H_\beta}}\left(\frac{Q^{-1}(\lambda_{H_\beta})}{Q^{-1}(\lambda_{Ar})}\frac{I_{H_\beta}}{I_{Ar}} - \frac{b_{H_\beta} K_{H_2}}{K_{Ar}}\frac{n_{H_2}}{n_{Ar}}\right) \tag{3.29}$$

which yields the absolute atomic hydrogen density based on actinometry results and on the model of the associated electron excitation rates calculated from the electron temperature in the discharge.

CHAPTER 4

Experimental Properties of MPDR™ 610

4.1 Introduction of MPDR 610

In this chapter the properties of the plasma discharges generated in the compact microwave plasma disk reactor are experimentally investigated. The source studied is designed for materials processing and synthesis applications, including use as an ion and free radical source injector in MBE deposition processes [67]. Some materials processing applications that have been investigated using this source include its use as an atomic nitrogen source in III-V nitride growth [68],[69], as an atomic oxygen source in high-temperature superconductor deposition [70],[71], and as an atomic hydrogen source for III-V substrate cleaning [72]. In the past this source has been characterized [73]-[77] for a number of discharge types including Ar, He, N_2 and O_2, but little work has been reported on hydrogen discharge characteristics. This chapter experimentally characterizes the Wavemat MPDR™ 610 [78] plasma source with argon, hydrogen, and argon-hydrogen mixture discharges running at the pressure range of 0.4-5 mTorr.

A sketch of the MPDR 610 source is shown in Figure 4.1. The cylindrical source is made of stainless steel with an outer diameter of 5.8 cm. The vacuum seal at one end of the source is made by a standard 4.5 inch Conflat flange with the entire length of the

source inserted into the processing chamber. At the other end of the source is a UHV metal to quartz vacuum seal. The discharge region at this end is confined within a cylindrical quartz tube which has a 3.6 cm diameter and 3.0 cm length. The quartz tube is surrounded by three ring shaped axially magnetized permanent magnets which provide a static magnetic field within the plasma discharge chamber for plasma confinement and for ECR plasma heating. The magnets have an outer diameter of 4.95 cm, an inner diameter of 4.32 cm, and a height of 1.27 cm. The three magnets are aligned with the same poles facing each other, as shown in Fig. 4.1. This magnet arrangement creates a multicusp magnetic field in the axial direction and tends to push the 875 Gauss ECR zone away from the quartz discharge wall. The quartz walls and the magnets are cooled by compressed air flowing through the center conductor and blowing onto the quartz top. The center conductor and the sliding short permit optimal microwave power coupling to the discharge region. A small loop antenna is attached to the sliding short, and this loop excites the electromagnetic modes in the microwave cavity. The region between the discharge and sliding short is a waveguide section with the first half section a coaxial waveguide section and the second half the evanescent circular waveguide region. The reason for the evanescent electromagnetic wave is the diameter of the waveguide region (5.6 cm) is too small to sustain any electromagnetic propagating modes for the 2.45 GHz excitation frequency. The lowest frequency EM propagating mode - TE_{11} requires a diameter of at least 7.2 cm at the frequency of 2.45 GHz. For more detail description of the MPDR 610 source, the reader should refer to Ref. [79].

Previous experimental measurements and characterizations of the MPDR 610 source done by A. K. Srivastava are summarized as the following:

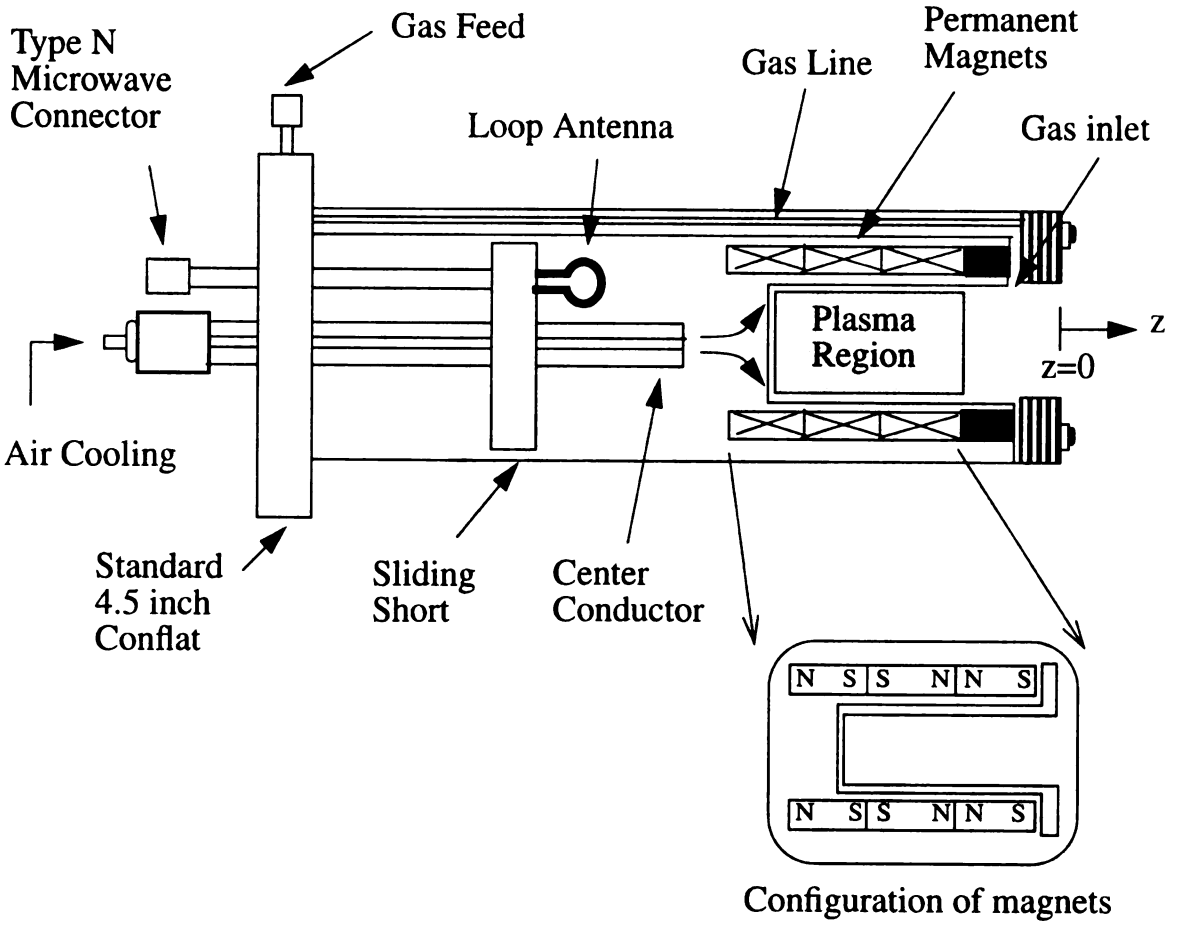

Figure 4.1 MPDR 610 cross section

(1) Ion density versus pressure (0.1 - 0.8 mTorr) at different input microwave powers (66, 82, 123, 164Watt).

(2) Ion current density versus pressure (0.1 - 0.8 mTorr) at different input microwave powers (66, 82, 123, 164Watt).

(3) Electron temperature versus pressure (0.1 - 0.8 mTorr) at different input microwave powers (66, 82, 123, 164Watt).

(4) Ion current density versus radial position (r=0 - 2 cm) at different downstream positions (z=1, 3 cm) and different input microwave powers (123, 164Watt).

(5) Electron energy distribution function at some specified plasma conditions.

(6) Ion energy distribution function at different input microwave powers (82, 123, 164Watt).

(7) Ion energy distribution function at different pressures (0.24, 0.43, and 0.72 mTorr).

(8) Plasma potential versus pressure (0.1 - 0.8 mTorr) at some specified plasma conditions.

(9) Ion energy distribution function at different downstream positions (z=5, 7, 9 cm).

It is noted that the pressures specified in this earlier work were the pump stack pressures. The pressure in the chamber was measured later to be about twice that in the pump stack. And, most of the measurements were taken in argon discharges. For nitrogen discharges, only measurements (5), (6), (7), (8), (9) were taken.

4.2 System Configuration

Fig. 4.2 shows the vacuum system used in the experiments. The processing chamber (1) with diameter of 19.5" and length of 10" is capped by two stainless steel plates (2)

with thickness of 2.5 cm on both its top and bottom ends. The vacuum seals on both ends are made with two O-rings. The plates are equipped with electrical motorized control to raise and lower the plates (2). This provides an easy access to the processing chamber for plasma diagnostics set up or processing substrate positioning. On the sides of the chamber there are four 10" diameter flanges each of 90 degrees apart. The MPDR 610 source (3) is inserted through one of the openings. Another opening at 90 degrees from the source is connected to a diffusion pump (4). The passage is controlled by a high vacuum gate valve (6) and then a throttling valve (7). The throttling valve is controlled by a MKS-651 pressure controller for a more precise control of chamber pressure. The diffusion pump is backed by a mechanical pump (5) which is purged by dry nitrogen at the exhaust when operating with a flammable gas such as hydrogen. Two thermocouple vacuum gauges (8) measure the roughing and foreline pressures which range from several mTorr to a few Torr. To measure the chamber pressure, a MKS-627 absolute pressure transducer (9) is installed at the bottom of the chamber and connected to the MKS-651 pressure controller which measures the pressure down to $1x10^{-5}$ Torr. In addition, an ionization vacuum gauge (SensaVac^{TM} 919) is located at the passage to the diffusion pump. This hot cathode vacuum gauge is capable of pressure readings down to $1x10^{-10}$ Torr and is used to calibrate the reading of the MKS-627.

High purity(99.999%) gas cylinders are connected to appropriate pressure regulators. Then the gases are flowed through 1/4" stainless steel tubing to a MKS-1159 flow controller (10) which is able to operate at a maximum flow of 100 sccm. The flow controller is connected to a MKS-247C 4-channel readout for flow rate settings.

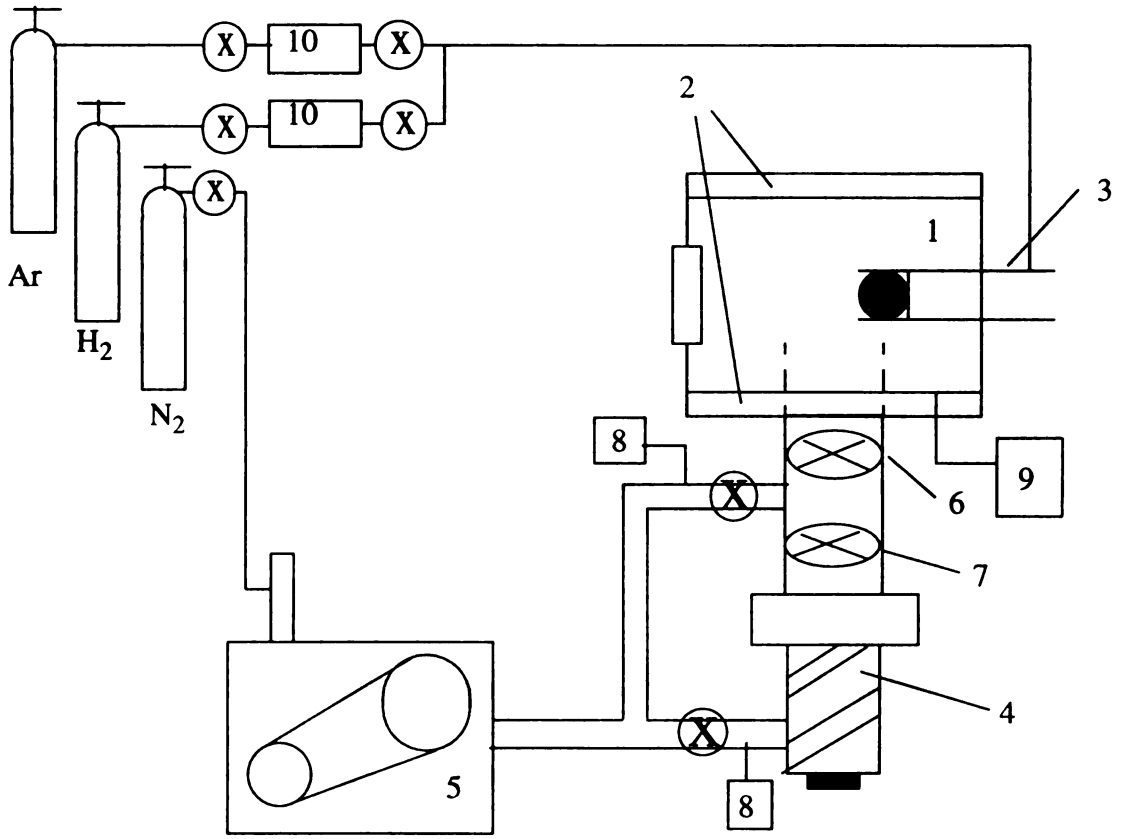

Figure 4.2 The vacuum system configuration

(1)Processing Chamber (2)Stainless Steel Plate (3)MPDR 610

(4)Diffusion Pump (5)Mechanical Pump (6)Gate Valve

(7)Throttling Valve (8)Thermocouple Vacuum Gauge (9)Absolute Pressure Transducer

(10)Flow Controller.

Microwave energy is supplied by a microwave power generator (Raytheon PGM-10). It outputs 2.45 GHz microwave power up to a maximum power of 100W. The microwave circuit includes a three-port circulator and a dummy load to protect the power supply. Two dual directional couplers each connected to attenuators and then two HP-432A power meters measure the incident and reflected power. The power meter for incident power reading was calibrated to have a correction factor of 0.909. That is, a 10 mWatt reading on the meter have an actual power of 9.09 Watt. The correction factor of the power meter for reflected power was also measured to be 0.902. The coaxial cable which transmits the microwave power to the MPDR 610 source has been measured to have a loss of 0.89dB. That is, 19% of the incident power is consumed into heat as it transmits down the cable.

4.3 The System Parameter Spaces and Measured Quantities

In order to have a better understanding and controllability in a complex plasma process, the processing system variables are categorized as three types of variables: the input variables, internal variables, and output variables. The input variables are defined to be able to be independently controlled and/or set at the beginning of a processing experiment, for example the operating power, pressure, gas flow rates, and substrate temperature. The internal variables are the dependent variables which are related and controlled by the different combinations of input variables. They can, for example, be plasma electron temperature, ion density, and neutral density. The output variables are the desired outputs from a process.

The following subsections describe the input variables and internal variables

con

per

diff

late

4.3

pla

4.3

Pro

considered in this thesis. The diagnostic measurements of the internal variables were performed in two regions: plasma source region and chamber (downstream) region with different settings of input variables. The results of these measurements will be presented later in this chapter.

4.3.1 Plasma Source Region Measurements

The input variables and observed internal variables defined in the measurements of the plasma source region are :

(1) Independent input variables:

(a) Pressure, **variable**: P = 0.4 - 5.0 mTorr.

(b) Input microwave power, **variable**: P_{in} = 60 - 90 Watt.

(c) Gas feed, **fixed**: H_2.

(d) Gas flow rate, **fixed**: f = 50 sccm.

(e) Microwave cavity tuning (Sliding short), **tuned for minimum P_{ref}.**

(f) Microwave cavity tuning (Probe position), **tuned for minimum P_{ref}.**

(2) Dependent internal variables:

(a) Reflected power, P_{ref}.

(b) Electron temperature, T_e.

(c) Neutral density: [H].

4.3.2 Processing Chamber Region Measurements

The input variables and observed internal variables defined in the measurements of the processing chamber region are :

(1) Independent input variables:

(a) Pressure, **variable**: P = 0.4 - 5.0 mTorr.

(b) Input microwave power, **variable**: P_{in} = 60 - 100 Watt.

(c) Gas feed, **variable**: Ar, H_2, Ar/H_2 .

(d) Gas flow rate, **variable**: f = 5 - 50 sccm.

(e) Microwave cavity tuning (Sliding short), **tuned for minimum P_{ref}.**

(f) Microwave cavity tuning (Probe position), **tuned for minimum P_{ref}.**

(2) Dependent internal variables:

(a) Electron temperature, T_e and EEDF.

(b) Electron density, [N_e].

(c) Ion densities: [Ar^+], [H^+], [H_2^+], [H_3^+].

4.4 Calibration of the Source Pressure

A pressure gradient was found to exist between the plasma source and the processing chamber region where the pressure transducer (9) is installed for chamber pressures sensing. The measured pressures in the chamber is usually less than the actual pressure in the MPDR 610 source. In order to find out the difference between them, an experiment was conducted. The discharge source region was connected directly to the pressure transducer by a plastic tube. The throttling valve position was changed from 100 to 1 % open and at each valve position, the actual pressure reading in the source is recorded. Next, the tube connecting the source region to the pressure transducer was removed. This is the setting under which the actual diagnostic measurements were taken. The test was then repeated. The chamber pressure was recorded. Table 4.1 lists the results of the hydrogen flow rate test. The H_2 gas flow was set at 30 sccm, a typical value used in plasma

parameters diagnostics in hydrogen discharges. Table 4.2 and 4.3 list the results of argon flow rate test with its flow rate set at 8 and 20 sccm, respectively.

Table 4.1 Results of hydrogen flow rate test. The flow rate is set at 30 sccm.

Valve position	Pressure (mTorr)		Difference
%	In source	In chamber	
100	0.63	0.41	0.22
80	0.63	0.41	0.22
60	0.65	0.43	0.22
50	0.67	0.45	0.22
40	0.72	0.50	0.22
30	0.82	0.60	0.22
20	1.10	0.86	0.24
15	1.42	1.22	0.20
10	2.18	1.92	0.26

Table 4.2 Results of argon flow rate test. The flow rate is set at 8 sccm.

Valve position	Pressure (mTorr)		Difference
%	In source	In chamber	
100	0.73	0.41	0.32
70	0.73	0.42	0.31
50	0.80	0.50	0.30
30	1.04	0.73	0.31
20	1.45	1.17	0.28
15	1.96	1.70	0.26
10	3.02	2.82	0.20
5	4.95	4.81	0.15
1	5.81	5.65	0.17

Table 4.3 Results of argon flow rate test. The flow rate is set at 20 sccm.

Valve position %	Pressure (mTorr) In source	In chamber	Difference
100	1.70	0.81	0.89
70	1.75	0.86	0.89
50	1.90	1.02	0.88
30	2.42	1.56	0.86
20	3.40	2.59	0.81
15	4.62	3.88	0.74
10	7.24	6.56	0.68

From the above tables, it is seen that for argon flow at 8 sccm, the actual pressure in the source is about 0.17 - 0.32 mTorr higher than the measured pressure in the chamber and about 0.22 mTorr higher for hydrogen flow at 30 sccm. The pressure difference decrease slightly as the operating pressure increases. The experimental data presented in this thesis therefore uses the corrected pressures in the plasma source unless otherwise specified.

4.5 Microwave Power Absorption in the Plasma

Although the microwave reflected power is tuned to be minimum each time the experiment on the MPDR 610 is running, the reflected powers in the discharges were found to be nonuniform in the argon discharge. Fig. 4.3 plots the absorbed power

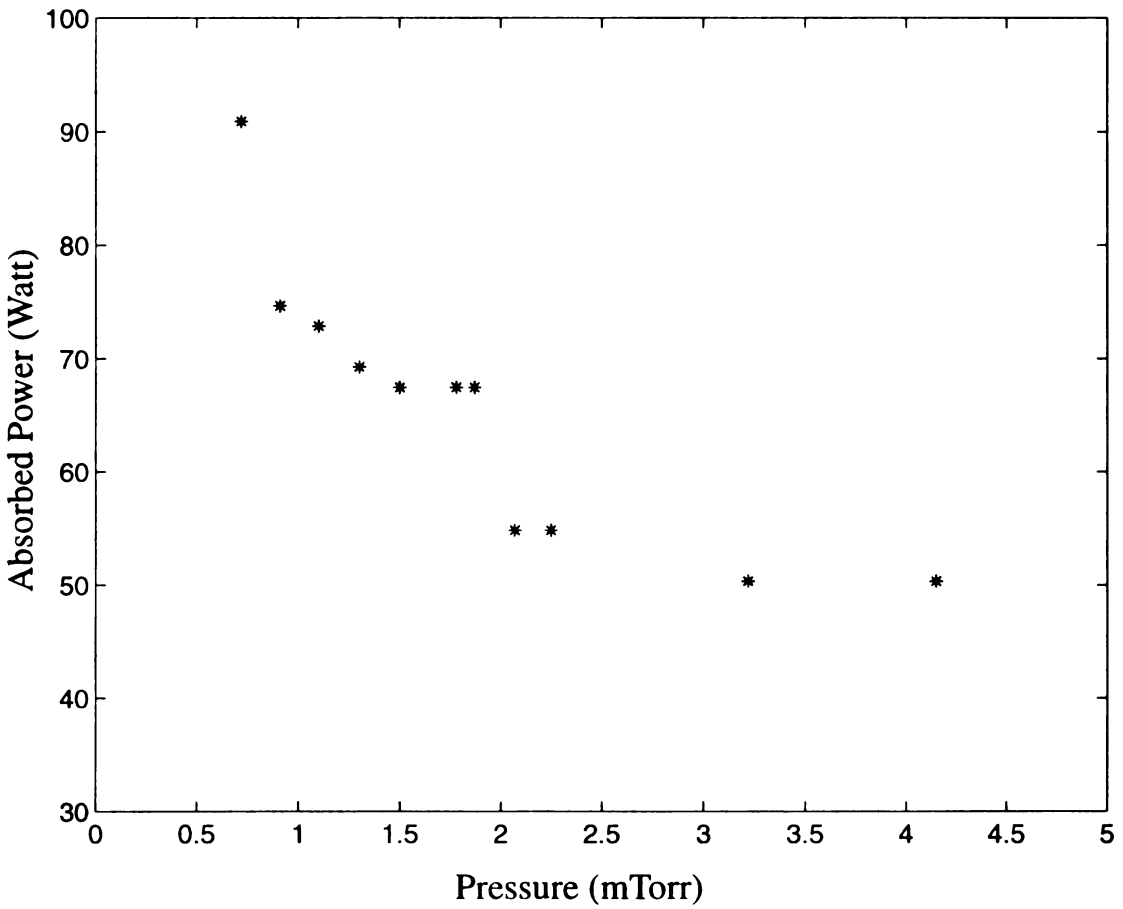

Figure 4.3 Power absorption in the argon discharge. Input power = 91W, flow = 8 sccm.

(incidentpower - reflected power) in the argon plasma at a flow rate of 8 sccm. The input power is 91 W. During the experiment, the sliding short position and the center conductor position were adjusted for minimum reflected power. Also note that the absorbed power plotted in Fig. 4.3 did not account for the 19% power loss in the coaxial transmission line as described in Section 4.2. Additionally, power absorbed by microwave cavity heating (direct wall heating), which is estimated to be 13% of the incident power for the operation conditions used in this work [79] needs to also be substracted to get the actual power absorbed. This concludes that the actual absorbed power is 32% less the value shown in Fig. 4.3. Unlike in the argon discharge, the typical reflected power observed in the hydrogen discharge was usually zero at lower pressures and less than 5 Watt at higher pressures (>3 mTorr).

4.6 Ion Density

The ion saturation current collected using a double Langmuir probe at pressures 0.5 - 4.0 mTorr in argon and hydrogen plasmas is shown in Fig. 4.4. The probe position was at 2 cm downstream. Fig. 4.5 shows the ion saturation current of the hydrogen discharge measured at 2 cm downstream with different flow rates (10-55 sccm). The input power is 90 W and the chamber pressure is fixed at 1 mTorr. The measurements were taken twice and the averaged value is plotted here. The saturation current appeared to be a weak function of the gas flow rate. The maximum saturation current occurred at 30 sccm. From Eqn. (3.9) in Chapter 3, we can see that the ion saturation current is directly proportional to the density of the plasma. Hence it can be used as an estimation of the ion densities.

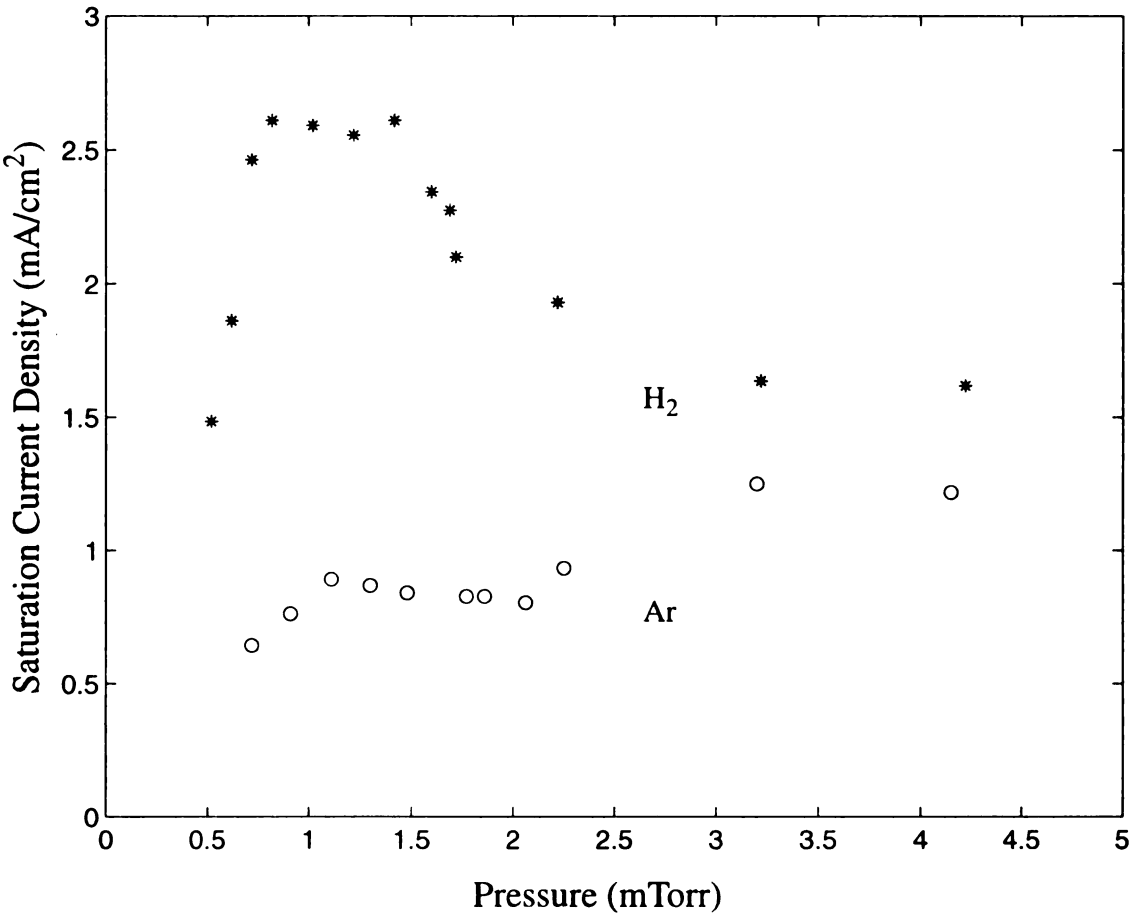

Figure 4.4 The ion saturation currents in argon and hydrogen plasmas where P_{in}=90W, z=2 cm. H_2 flow = 30 sccm, Ar flow = 8 sccm.

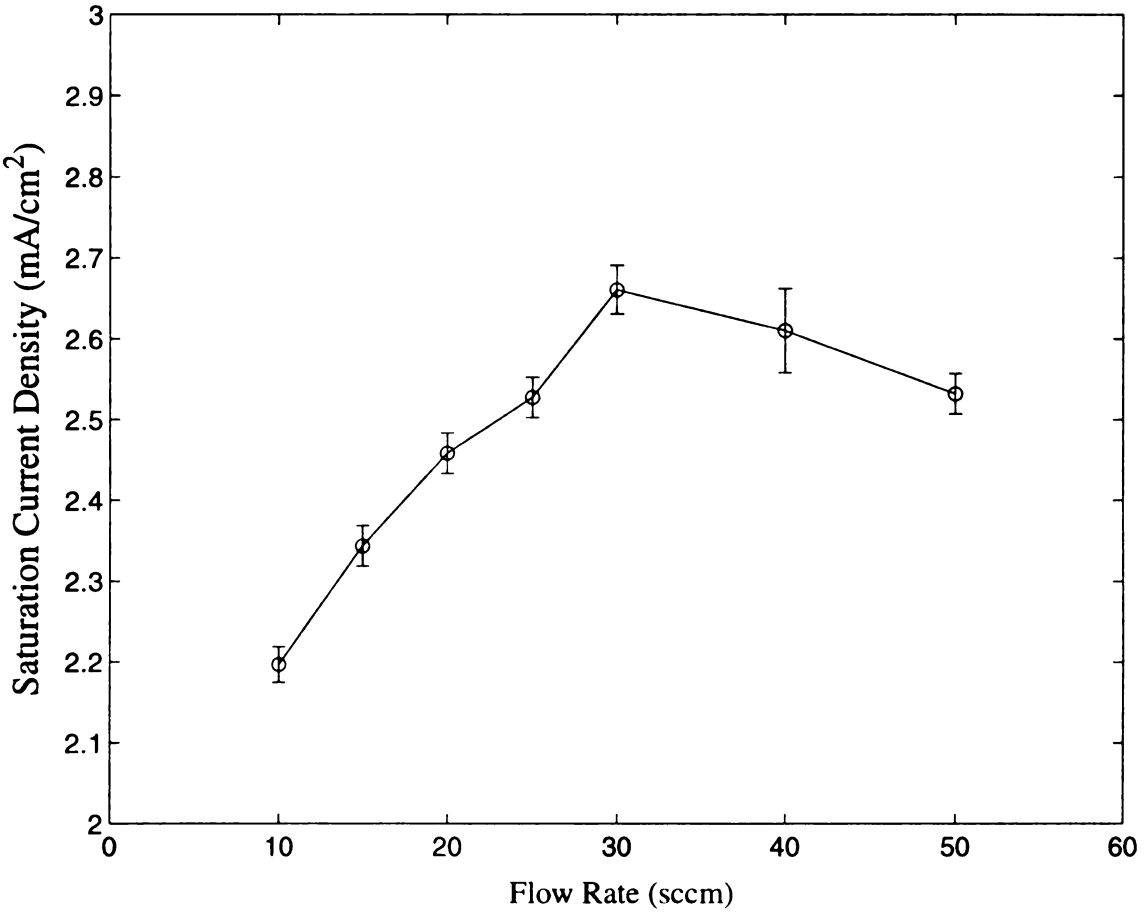

Figure 4.5 Hydrogen plasma ion saturation current at 2 cm downstream with various gas flow rates. P_{in}= 90W. Pressure = 1 mTorr.

The ion

stated in S

input micro

versus pres

taken at 2 c

this definit

measuremer

Fig. 4.7

(z=2cm) wit

Note that in

in Chapter 6

increases as

90 watt input

powers. This

to the dissoci

of the ion de

detail analysi

following cha

Fig. 4.8 sh

would indicat

predicted from

species decreas

the wall. Note h

The ion densities reported in this thesis are from the results of DLP measurements as stated in Section 3.2. The operating pressure ranges from 0.5 mTorr to 4 mTorr and the input microwave powers are 90W and 72W. The ion densities of the argon plasma plotted versus pressures is shown in Fig. 4.6. The gas flow rate is 8 sccm. The measurements were taken at 2 cm downstream from the end of the source to the center of the probe. Note that this definition of downstream distance will be adopted for the Langmuir probe measurements presented through this thesis.

Fig. 4.7 shows the hydrogen ion density versus pressure at the same probe position (z=2cm) with flow rate of 30 sccm. Three input power levels (90, 72, and 54W) were used. Note that in the calculation of ion density, we chose the H_2^+ ion mass which as shown later in Chapter 6 is the dominant ion species in the hydrogen discharge. The ion density increases as the pressure increases up to about 1.5 mTorr and then it starts to decrease at 90 watt input power. Similar density curves also occur at 72 and 54 watt microwave input powers. This may be due to at higher pressures more of the electron collision energy goes to the dissociation of molecular hydrogen instead of ionization. Therefore slight decreases of the ion densities were observed as the pressure increased above 1.5 mTorr. A more detail analysis of the power dissipation of the absorbed power will become clear in the following chapters where the modeling of the discharge source is presented.

Fig. 4.8 shows the downstream ion density variation. A linear line on this semilog plot would indicate an exponential decay of the densities along the downstream region. As is predicted from the ambipolar diffusion of charged species, the densities of the charged species decrease in the power of exponential as they diffuse away from the source and to the wall. Note here that to account for the possible increase of sheath thickness due to the

Figure 4.6

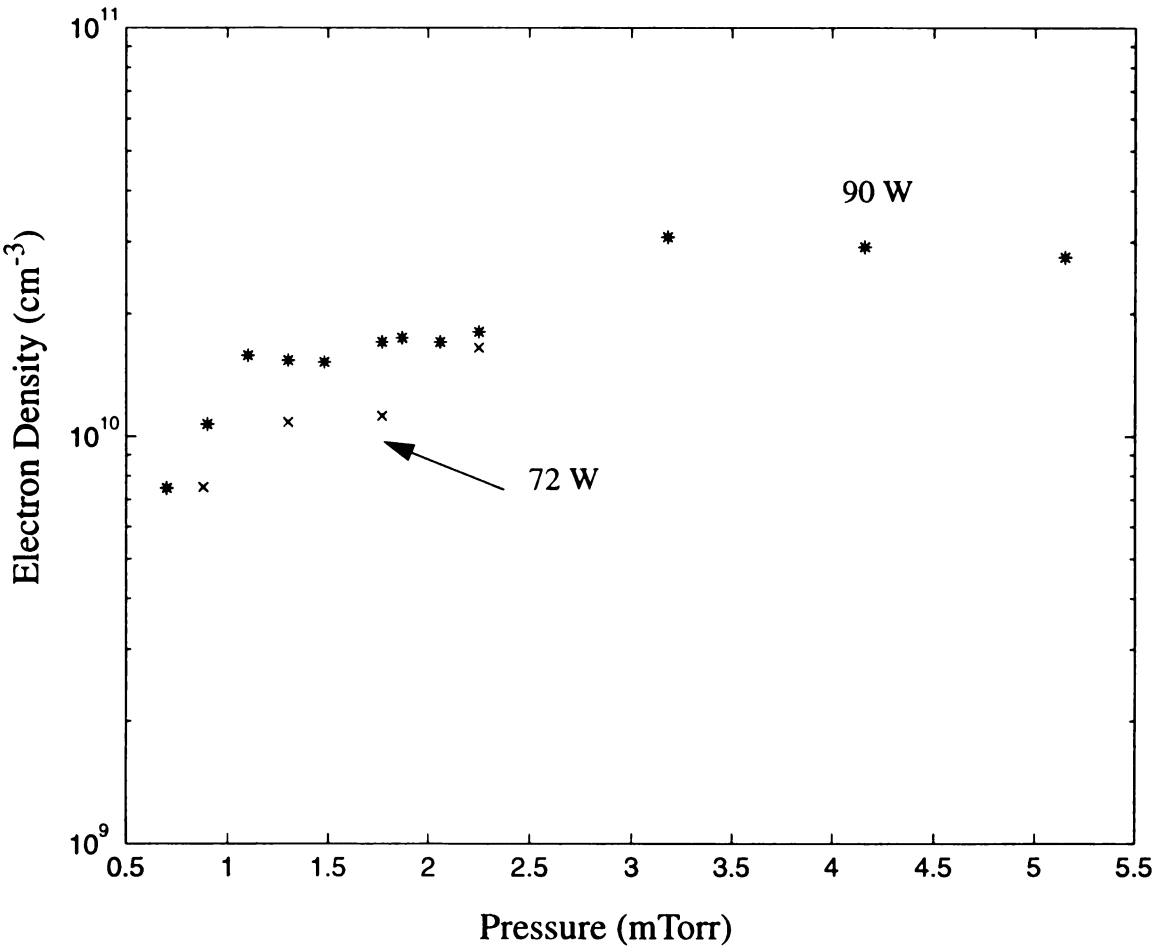

Figure 4.6 The ion densities of argon plasma measured at 2 cm downstream. Input powers are 90, and 72 W. Flow rate is 8 sccm.

Figure 4.7 H
are 90, 6

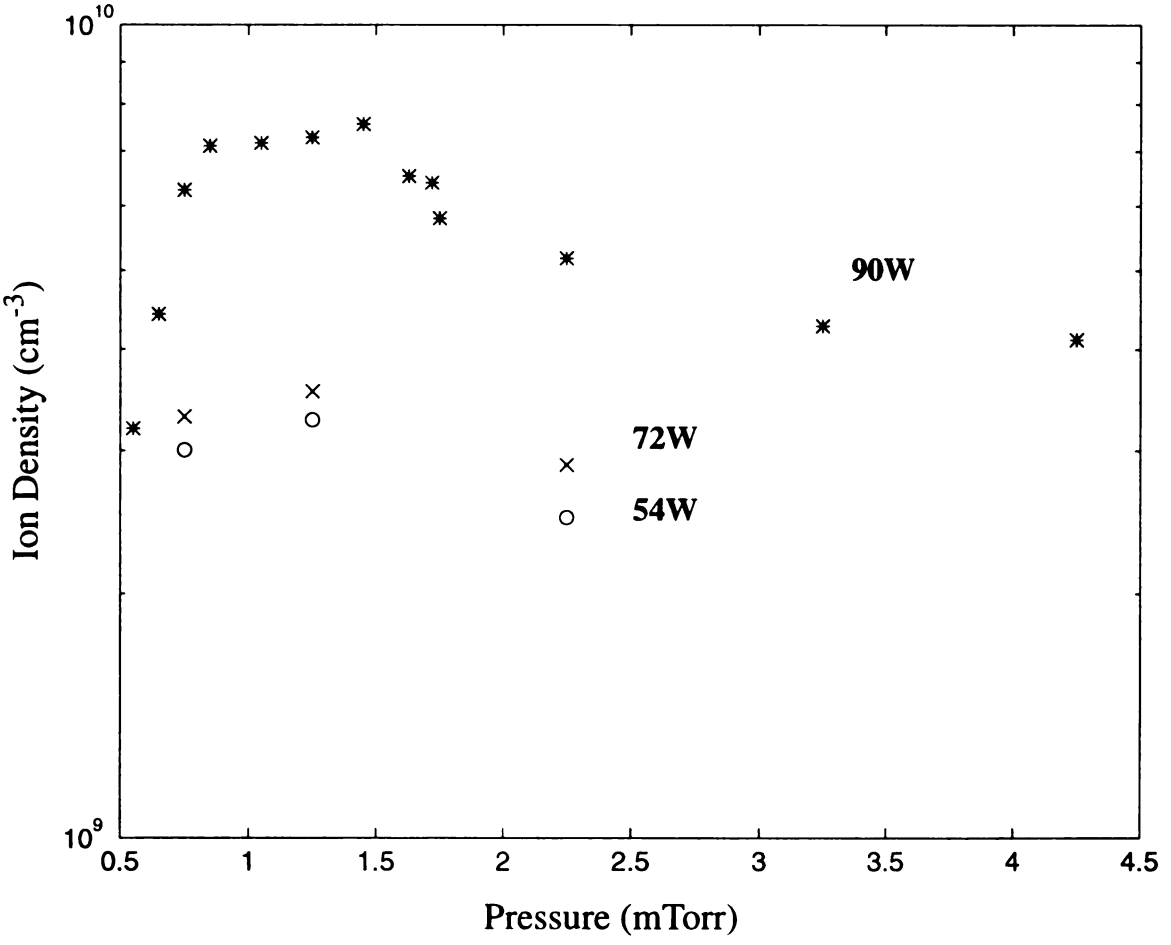

Figure 4.7 Hydrogen ion densities measured at 2 cm downstream. The input powers are 90, 63, and 54 W. Flow rate = 30 sccm. The ion assumed for this density determination is H_2^+.

Electron Density (cm^{-3})

Fig

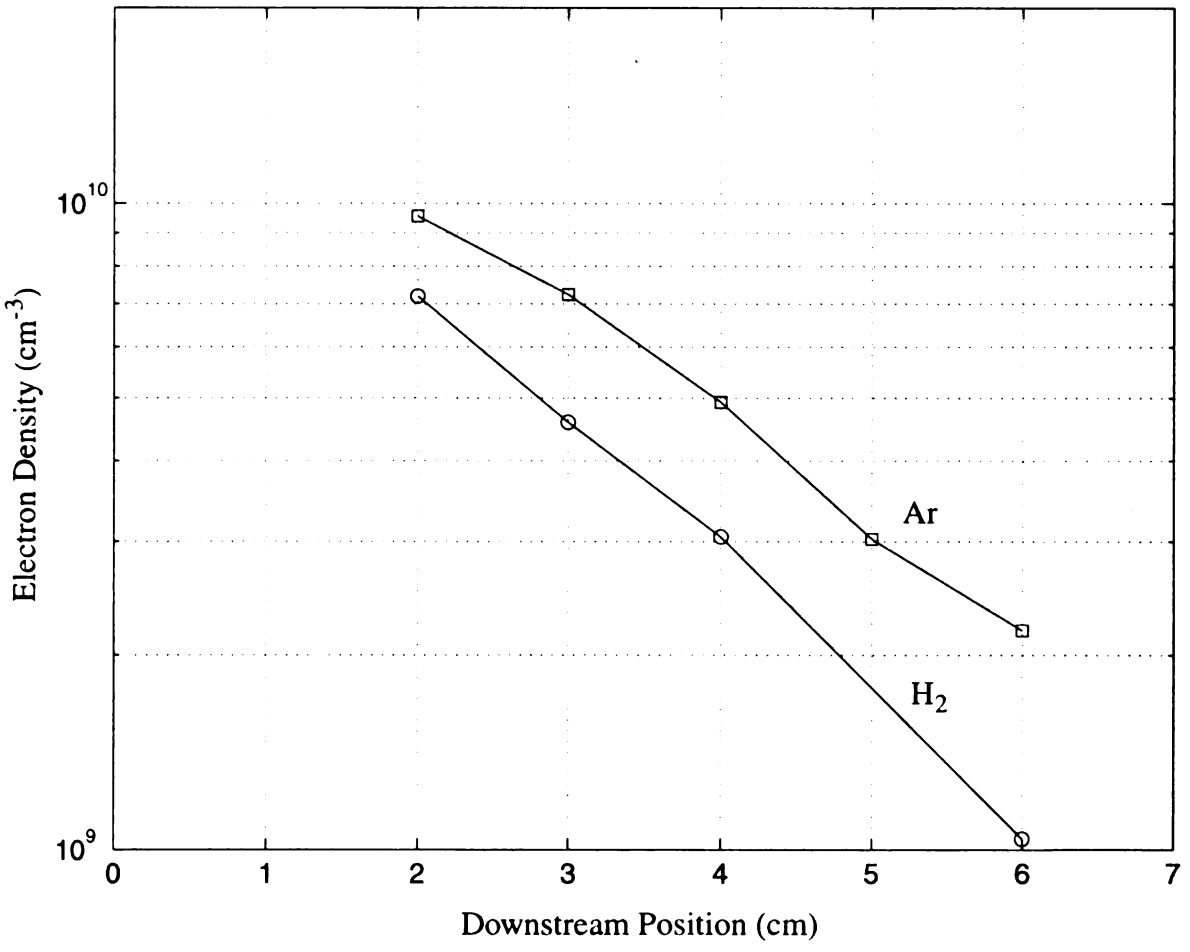

Figure 4.8 Downstream ion densities of argon and hydrogen plasmas. The input power is 90W, and the pressure is 1 mTorr.

increase of electron Debye length, we used a Child law sheath [51] to calculate sheath thickness. The equation for the sheath thickness is given as

$$s = \frac{\sqrt{2}}{3}\lambda_{De}\left(\frac{2V_o}{T_e}\right) \tag{4.1}$$

where λ_{De} is the electron Debye length, and V_o is the potential difference between the plasma and probe surface. The effective probe collecting area A_p is then corrected using a cylindrical surface with radius R = r + s, where r is the probe radius. The values of A_p become much larger as the plasma densities continue to decrease further downstream in the chamber region.

4.7 Electron Energy

The electron energy distribution function (EEDF) and average electron energy in the downstream region were obtained from single Langmuir probe (SLP) measurements. For downstream spatial variation of the electron temperatures, an in vacuum stepper motor was used to remote control the position of the probe. This arrangement has the advantage of not having to open the chamber to re-position the probe and pump down the processing chamber to vacuum again. Since the plasma stayed on during the measurements, it prevented possible variations of the operation condition if the plasma was regenerated every time the probe position was changed. The electron temperature in the source was also measured using OES with small amounts of noble gases (Ar, Kr, Xe) added in the hydrogen discharge.

Figs. 4.9 and 4.10 show the electron temperature dependence on pressure in argon and

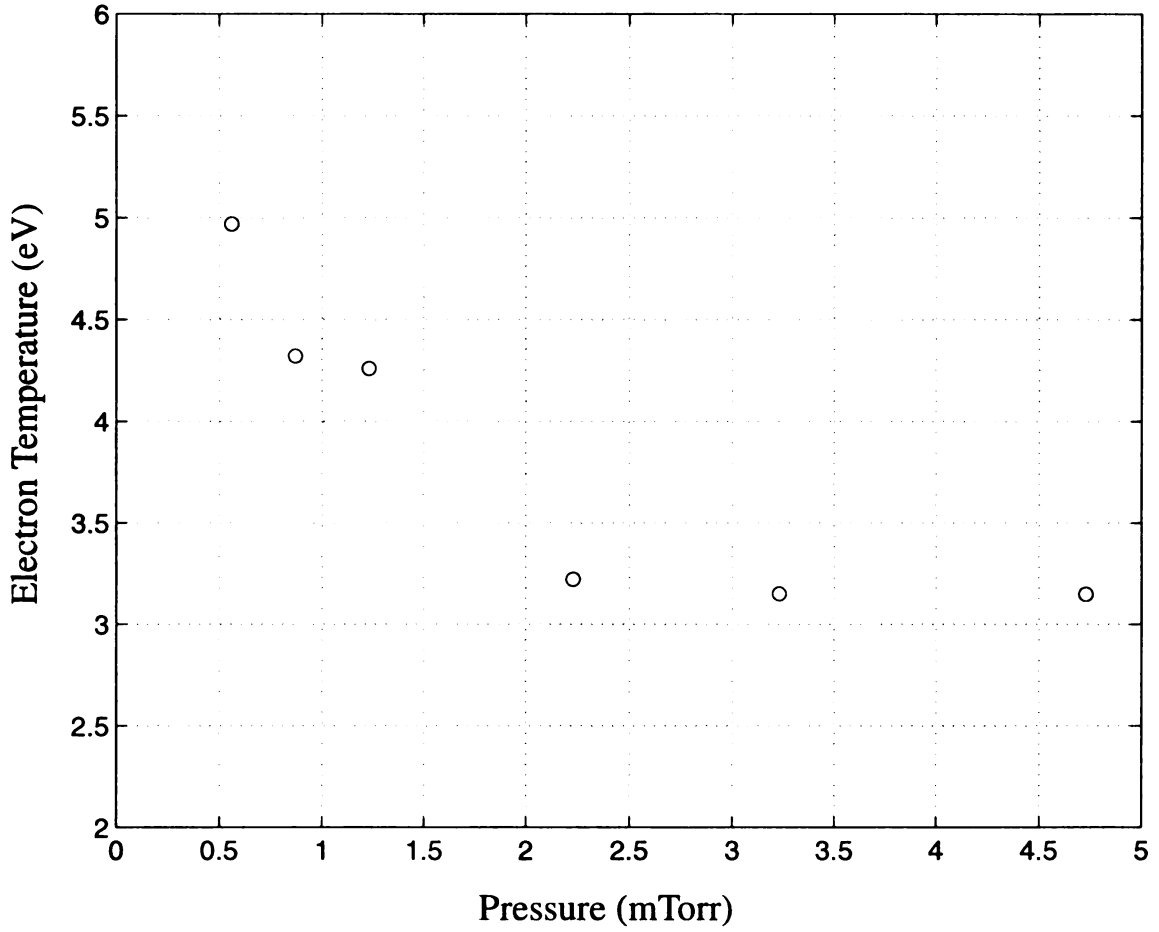

Figure 4.9 Argon plasma electron temperatures at 2 cm downstream. P_{in}= 90W, and flow rate = 8 sccm.

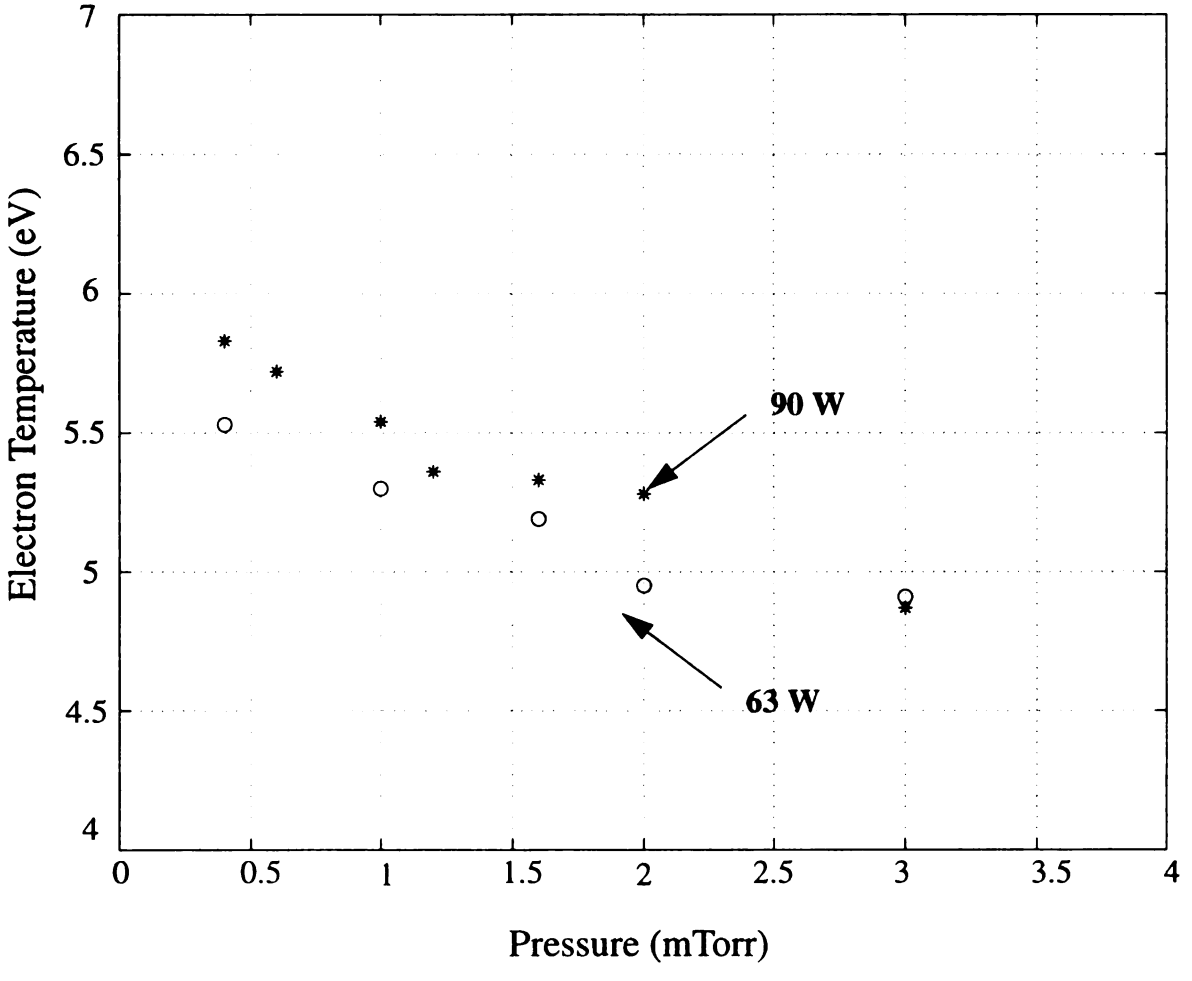

Figure 4.10 Hydrogen plasma electron temperature. P_{in}= 90 (*) and 63 W (o). Gas flow rate = 30 sccm.

hydrogen discharges. Two input powers 90 and 63W were used in Fig. 4.10. The single Langmuir probe used for this measurement was positioned at 2 cm downstream from the end of the source for both argon and hydrogen plasmas. The data shows an electron temperature increase as the pressure goes down. This is the expected behavior since in order to sustain the discharge as the pressure drops, the electron temperature must increase enough to maintain sufficient ionization. Fig. 4.9 shows the electron temperatures in an Ar plasma drops from 5.0 eV to 3.2 eV as the chamber pressures changed from 0.5 to 4.7 mTorr. In Fig. 4.10 the hydrogen electron temperatures had about 1.0 eV change in the pressure range of 0.5 -3 mTorr and 90 W input power. The plasma potentials determined from the maximum of the second derivative of SLP I-V characteristic are shown in Fig. 4.11.

Fig. 4.12 plots the electron temperature in the Ar-H_2 mixture discharge with various gas compositions. At 0.6 mTorr, the electron temperature increases from 5.4 eV to 6.2 eV as the hydrogen partial pressure ratio increases from 0.5 to 5. As we compare the results with argon and hydrogen discharges at the same pressure, it is found that at a low ratio (P_{H2}/P_{Ar}), the electron temperature in the mixture discharge is close to that in the argon discharge and at a high ratio, it is close to that in the hydrogen discharge within reasonable experimental error.

The emission spectrum of an argon plasma at a low pressure of 0.3 mTorr with an input power of 90 W and a flow rate of 3 sccm was also observed and it is shown in Fig. 4.13. Two argon doubly ionized emission lines were found. They are lines at 328.59 nm and 331.13 nm. This indicated the existence of high energy electrons (>25 eV) at a low pressure, i.e. 0.3 mTorr. Or, that is to say, that the high energy tail of the EEDF can not be

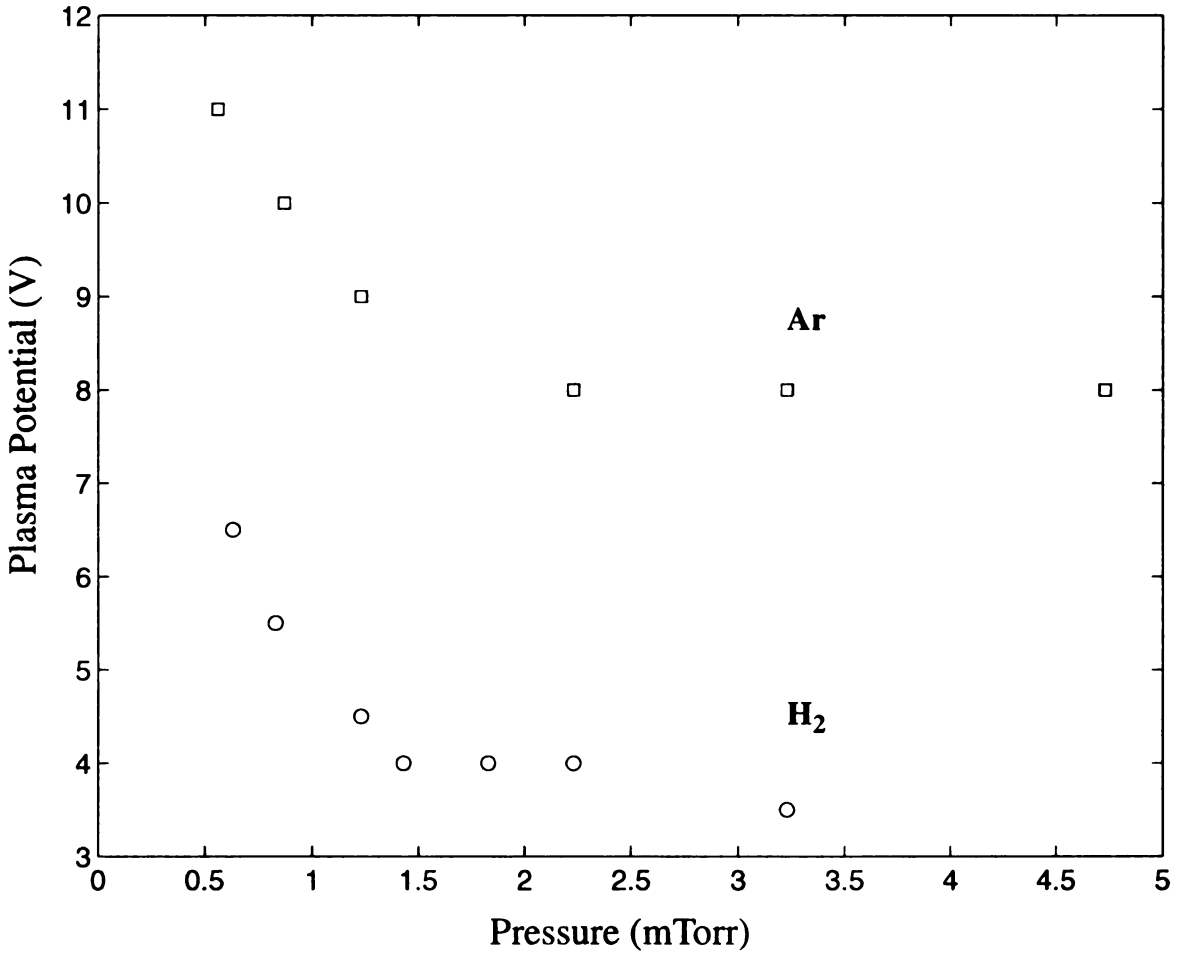

Figure 4.11 The plasma potentials in Ar and H_2 discharges measured at 2 cm downstream. P_{in}= 90W. H_2 flow rate= 30 sccm. Ar flow rate= 8 sccm.

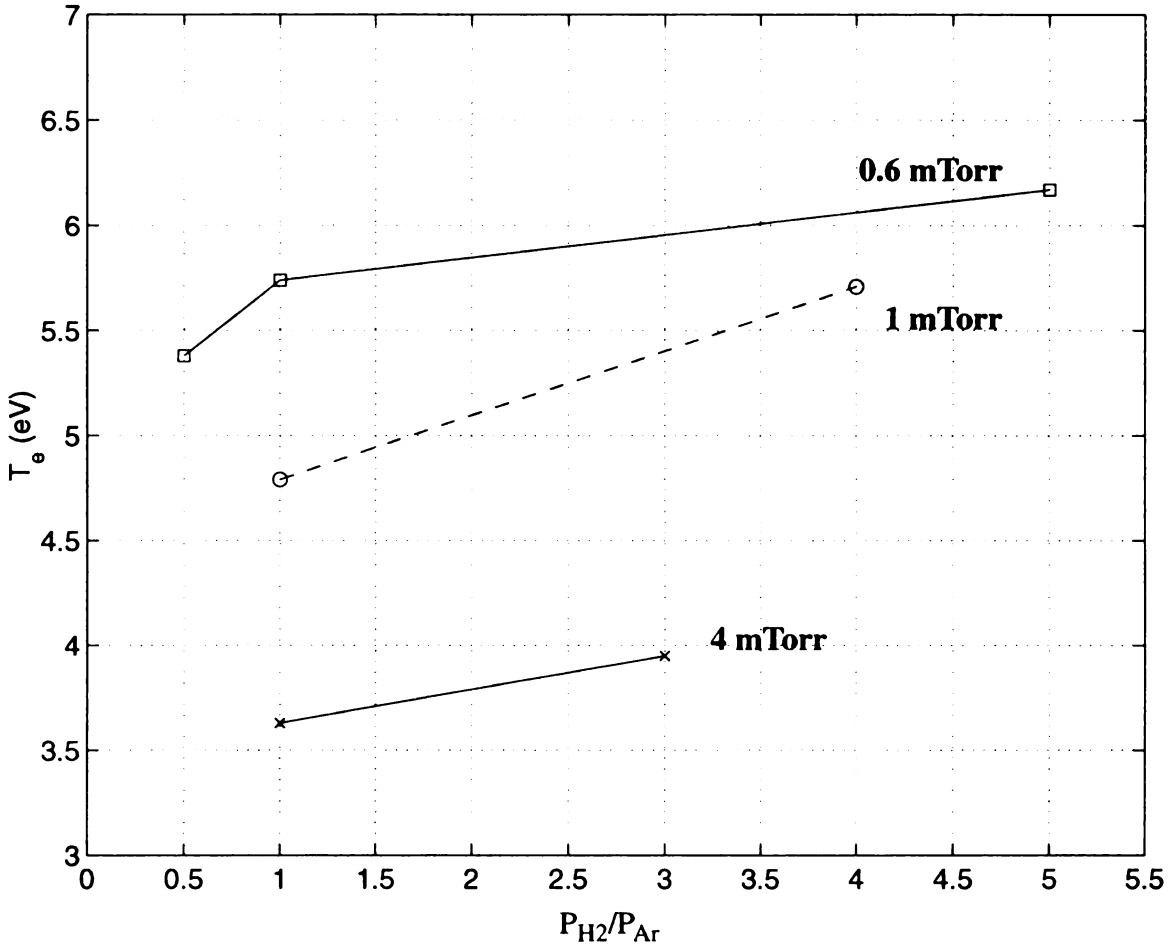

Figure 4.12 The electron temperatures in Ar/H_2 mixture plasma taken at 2 cm downstream. The input power is P_{in}=90W. The gas composition is varied.

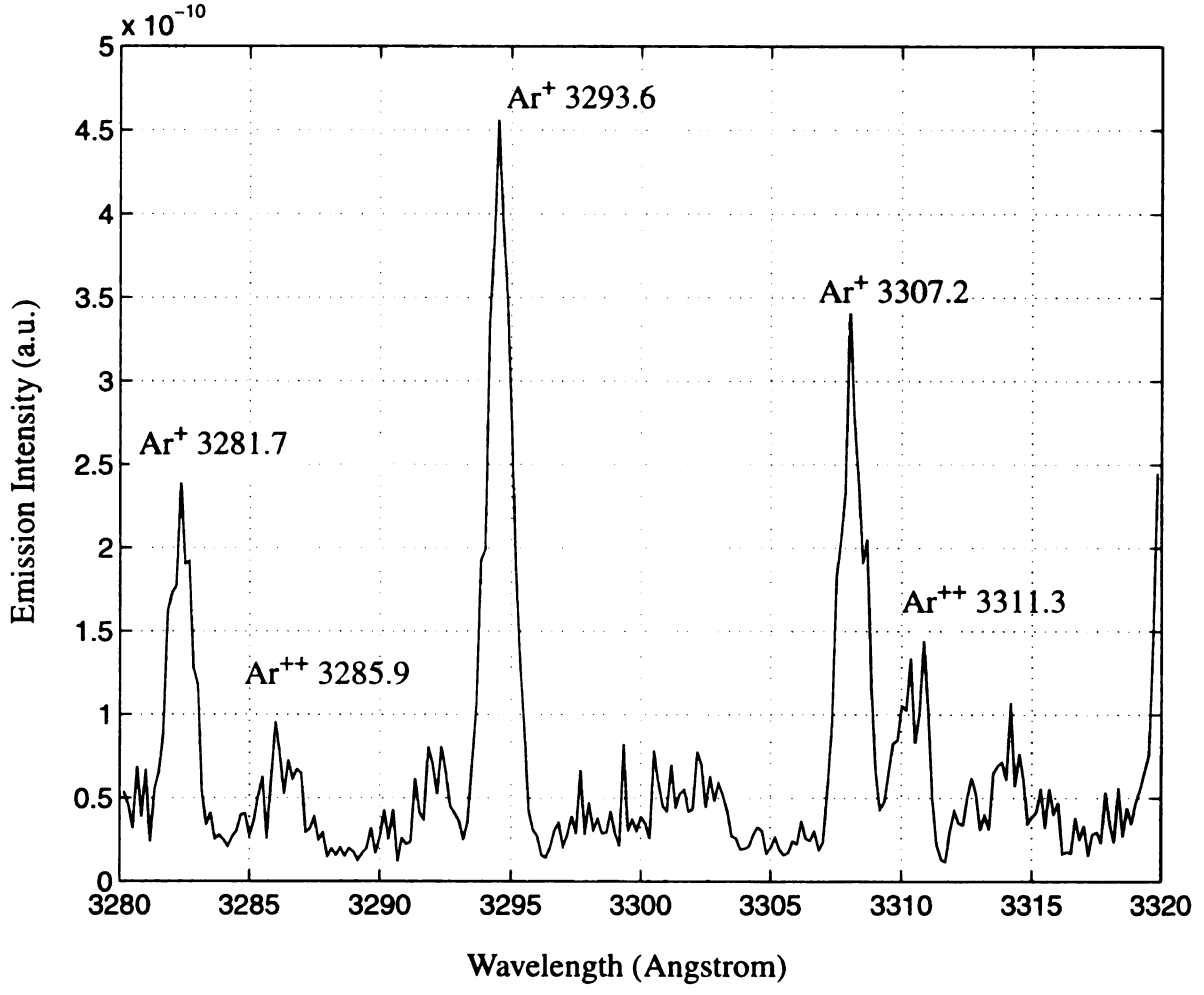

Figure 4.13 Argon plasma emission spectrum at 90W input power, 0.3 mTorr, and flow rate of 3sccm. Monochromator slit width is 50 micron.

ignored.

The downstream EEDF of argon and hydrogen discharges are plotted in Figs. 4.14 and 4.16. It can be seen that at the same operating conditions, the electron temperature decreased from 4.25 to 2.37 eV in argon plasma and from 5.48 to 2.39 eV in the hydrogen plasma as the probe position was moved from 2 cm to 6 cm downstream from the plasma source. The electrons gain energy in the source region through ECR heating and lose energy by collisions with particles (neutrals, and ions) in the discharge. As the electrons diffuse out of the source region they continue to lose their energies when collisions happen and they gain no more energies in the downstream region. Hence the electron temperature drops as electrons diffuse through the downstream region and toward the chamber wall.

Figs. 4.15 and 4.17 plot the electron temperature vs. downstream position in the argon and hydrogen discharge respectively. An extrapolated dashed line is drawn to the z =0 cm position. This gives an estimated electron temperature of the discharge in the source region where the Langmuir probe technique is not applicable due to the static magnetic fields in this region. The estimated electron temperature in the argon discharge region is about 5.9 eV and in hydrogen discharge, it is 7.8 eV. The EEDF of argon and hydrogen plasmas plotted on a logarithm scale is shown in Figs. 4.18 and 4.19. The data was taken at an input power of 90W, pressure of 2 mTorr, and a downstream position of z=2 cm for argon discharge.

Within the plasma source the electron temperature of the hydrogen plasma is measured using the OES technique as described earlier in Section 3.4.1. The ratio of observed emission intensity to calculated intensity versus transition threshold energy is plotted in Fig. 4.20 for a pressure of 3 mTorr. Various electron energies ranging from 1.2 eV to 7.5

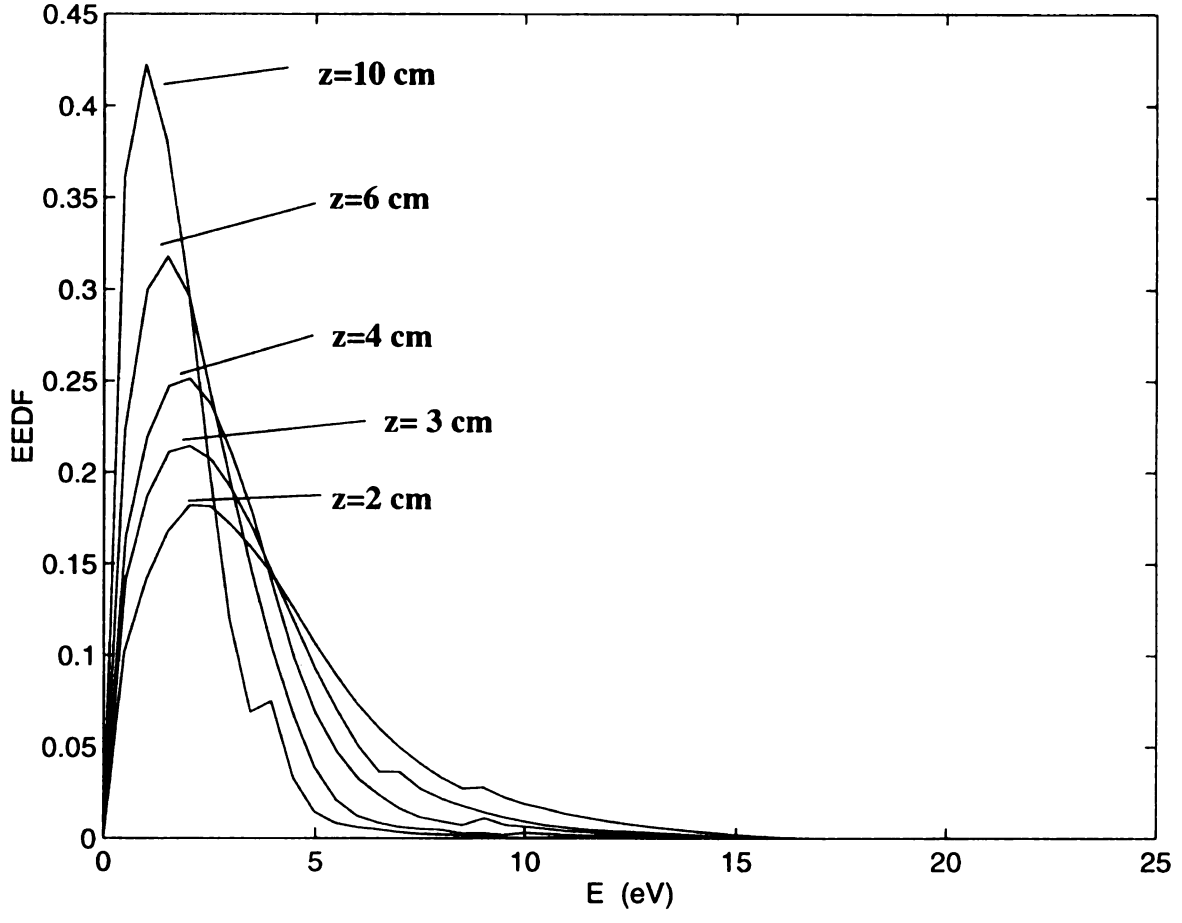

Figure 4.14 The EEDF of Ar plasma. P_{in}= 90W. Pressure = 1 mTorr and z = 2, 3, 4, 6, 10 cm with $\langle E_e \rangle$= 4.25, 3.50, 2.95, 2.37, 1.81 eV respectively.

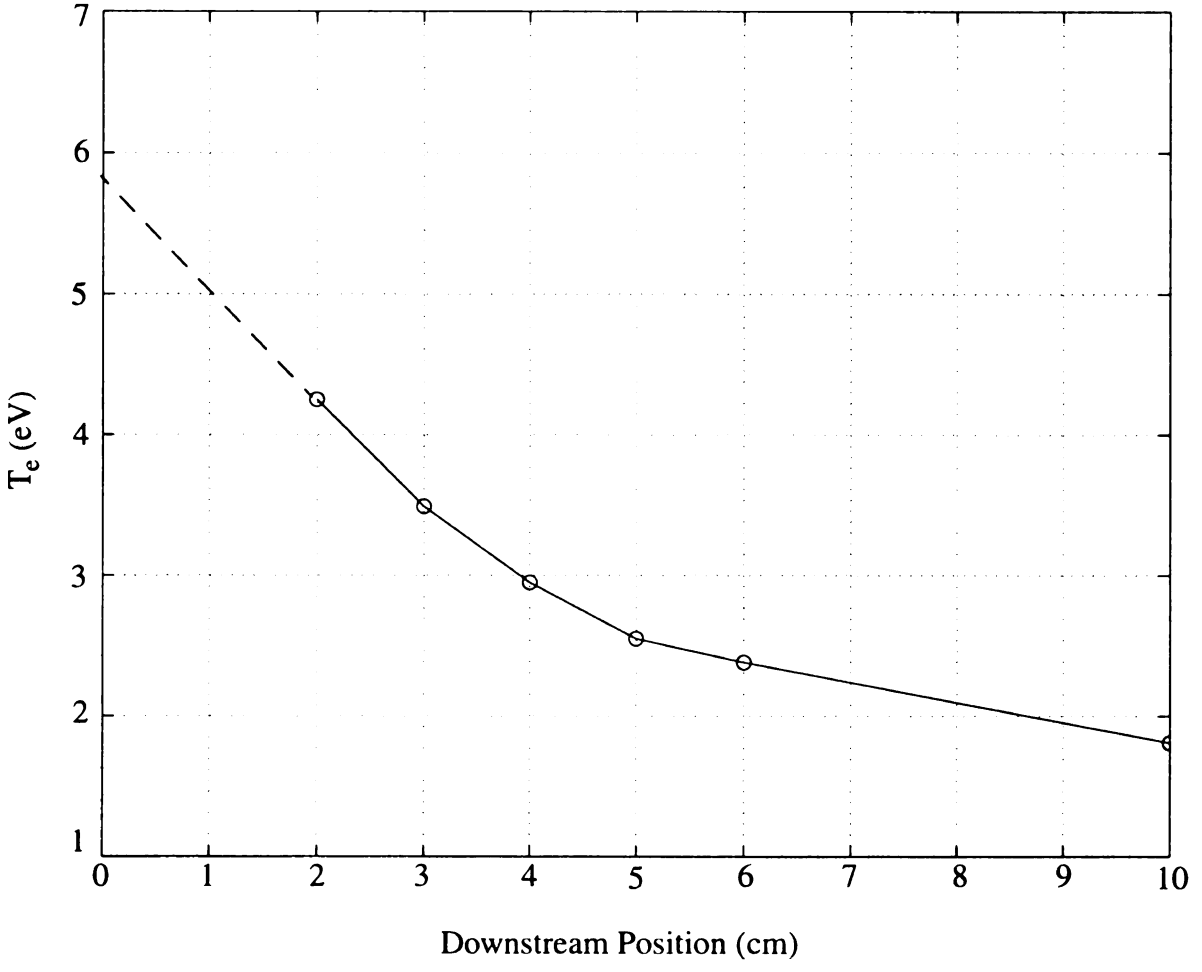

Figure 4.15 Electron temperatures of Ar plasma at downstream positions z = 2-10 cm. The extrapolating line to z=0 cm indiates an estimation of the electron temperature in the source being 5.9 eV .

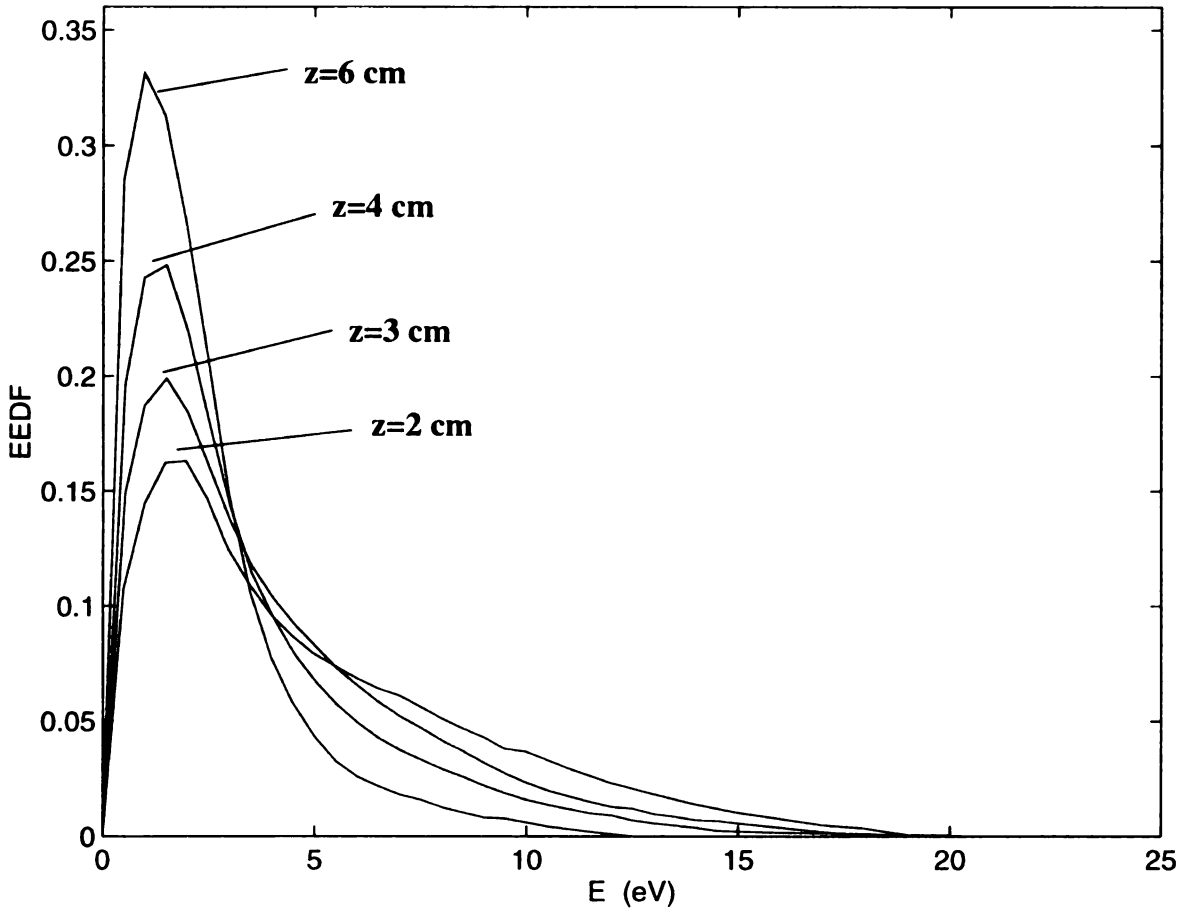

Figure 4.16 The EEDF of H_2 plasma. P_{in}= 90W. Pressure = 1 mTorr and z = 2, 3, 4, 6 cm with $\langle E_e \rangle$= 5.48, 4.46, 3.68, 2.39 eV respectively.

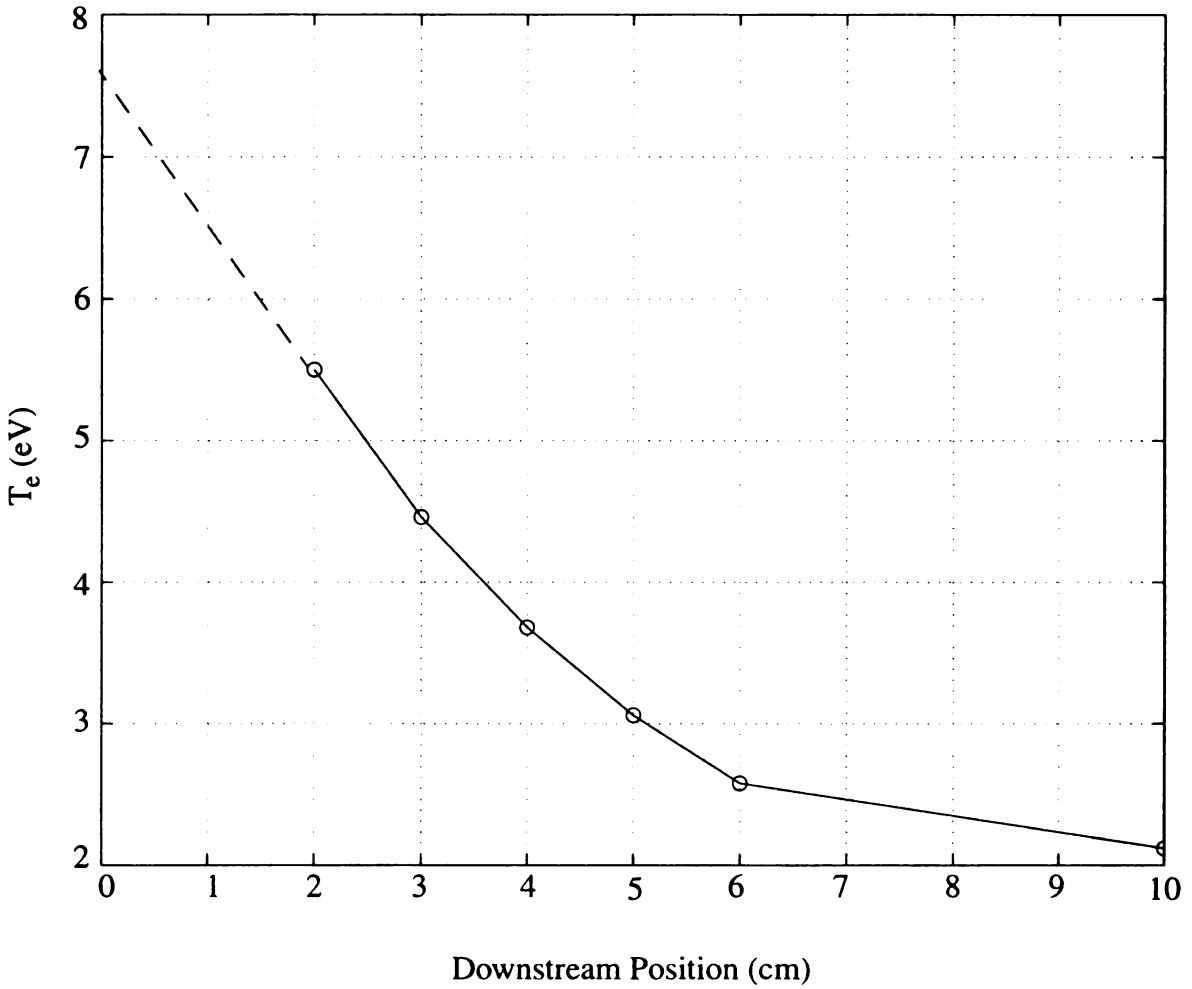

Figure 4.17 Electron temperatures of H_2 plasma at downstream positions z = 2-10 cm. The extrapolating line to z=0 cm indiates an estimation of the electron temperature in the source being 7.8 eV.

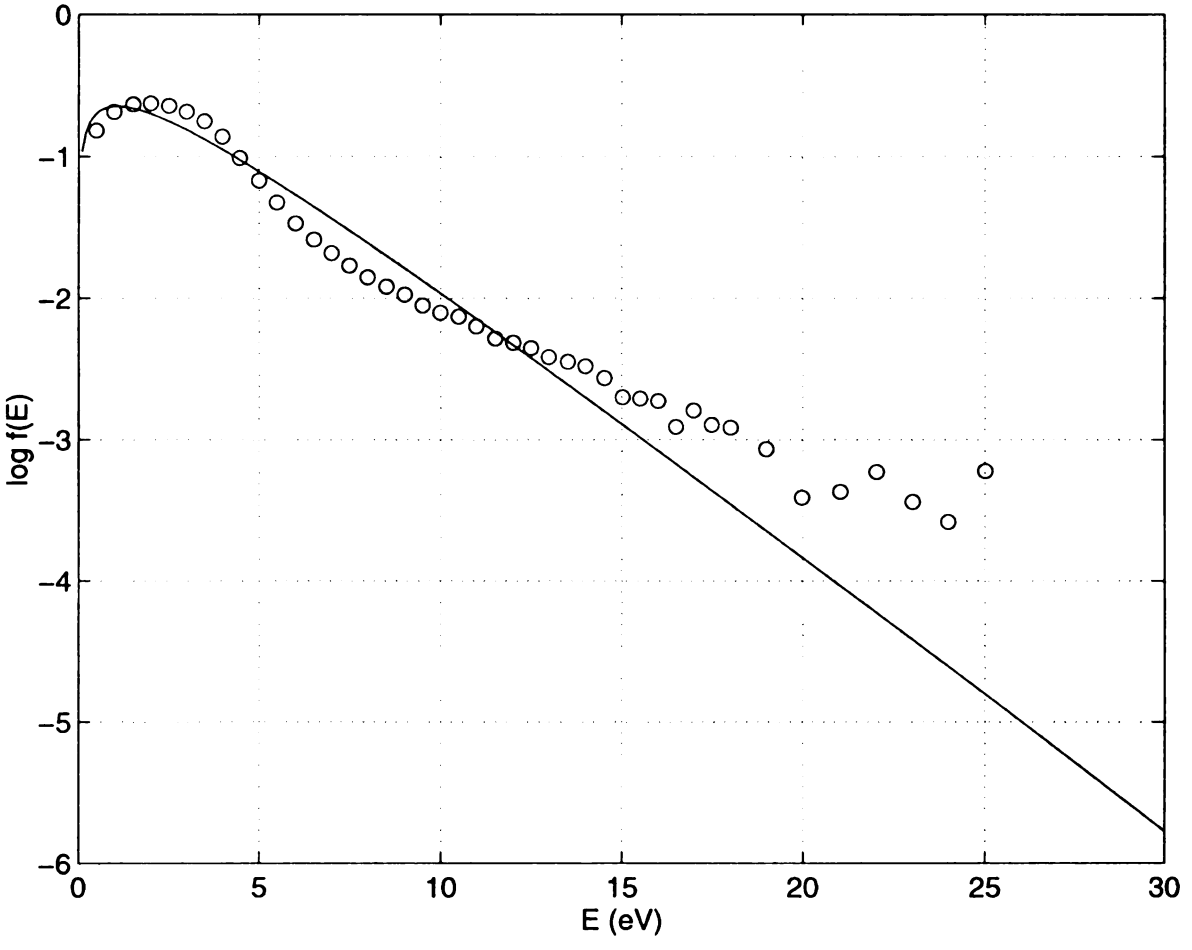

Figure 4.18 The EEDF of Ar plasma plotted on a logarithm scale. P_{in}=90 W, pressure = 2 mTorr, z = 2 cm, and flow rate = 8 sccm. The electron temperature is 3.22 eV.

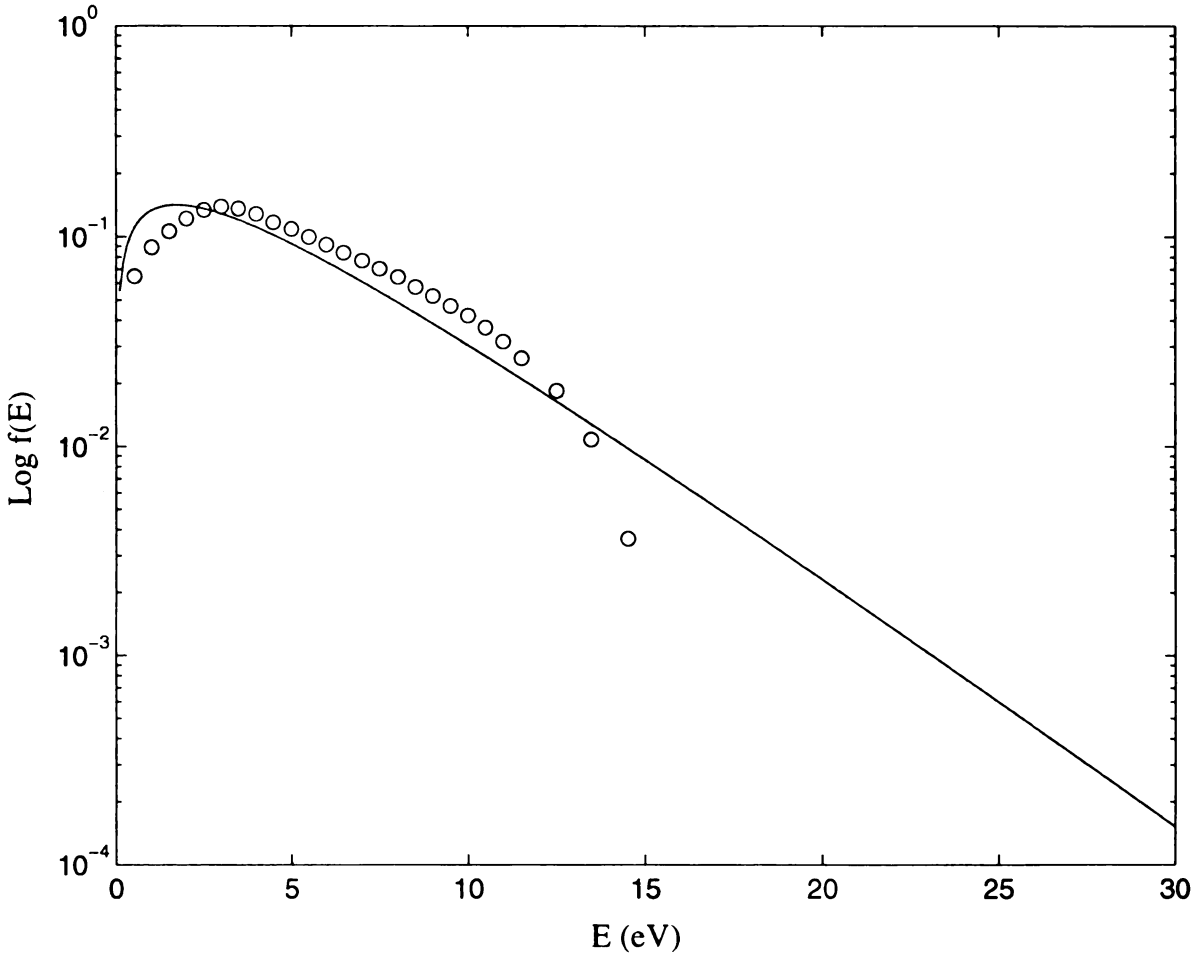

Figure 4.19 The EEDF of hydrogen plasma plotted on a logarithm scale. P_{in}= 90 W, pressure = 0.4 mTorr, and z = 3 cm.

eV were used for the calculated emission value, I_{cal}. A least squares line fit of each I_{obs}/I_{cal} data set versus threshold energy is used to obtain the slope for the different assumed electron energies. The electron temperature was estimated to be between 1.2 and 2 eV where the slope of fitted line would be zero. This value was low compared with the results from Langmuir probe measurements(~4.5 eV). The possible reasons for the difference maybe due to the following. The emission lines observed here have threshold energies ranging from 9.8 to 13.5 eV. The excitation and ionization energies of molecular hydrogen are known to be mostly in the range of 11.2 - 15 eV. Since only a small amount of noble gases are added in the discharge, most of the electronic collisions will happen with hydrogen neutrals. This could make the electron distribution depleted in the energy range above about 11 eV from Maxwellian distribution. For example, refer to the earlier electron temperature measurement shown in Fig. 4.19. Here the calculated emission intensities (I_{cal}) would be estimated to be larger for a Maxwellian distribution and therefore their ratios I_{obs}/I_{cal} would be smaller. If we look at the emission lines used again, most of them have energies of 11.2 - 13.5 eV except for the xenon emission lines.

An alternative way is ignoring the xenon emission data and replotting Fig. 4.20 in Fig. 4.21. The electron temperatures used here were from 2 to 12 eV and the threshold energies from 11.4 to 13.5 eV. The slopes of the fitted lines for each electron temperature value in Fig. 4.21 are plotted in Fig. 4.22. For comparison, the fitted line slopes from Fig. 4.20 were also plotted at the same time. The electron temperature where the slope is zero indicates $I_{obs}=I_{cal}(T_e)$. It is therefore this electron temperature of 6.6 eV from the interpolation of Fig. 4.22 that is responsible for the observed source region emission.

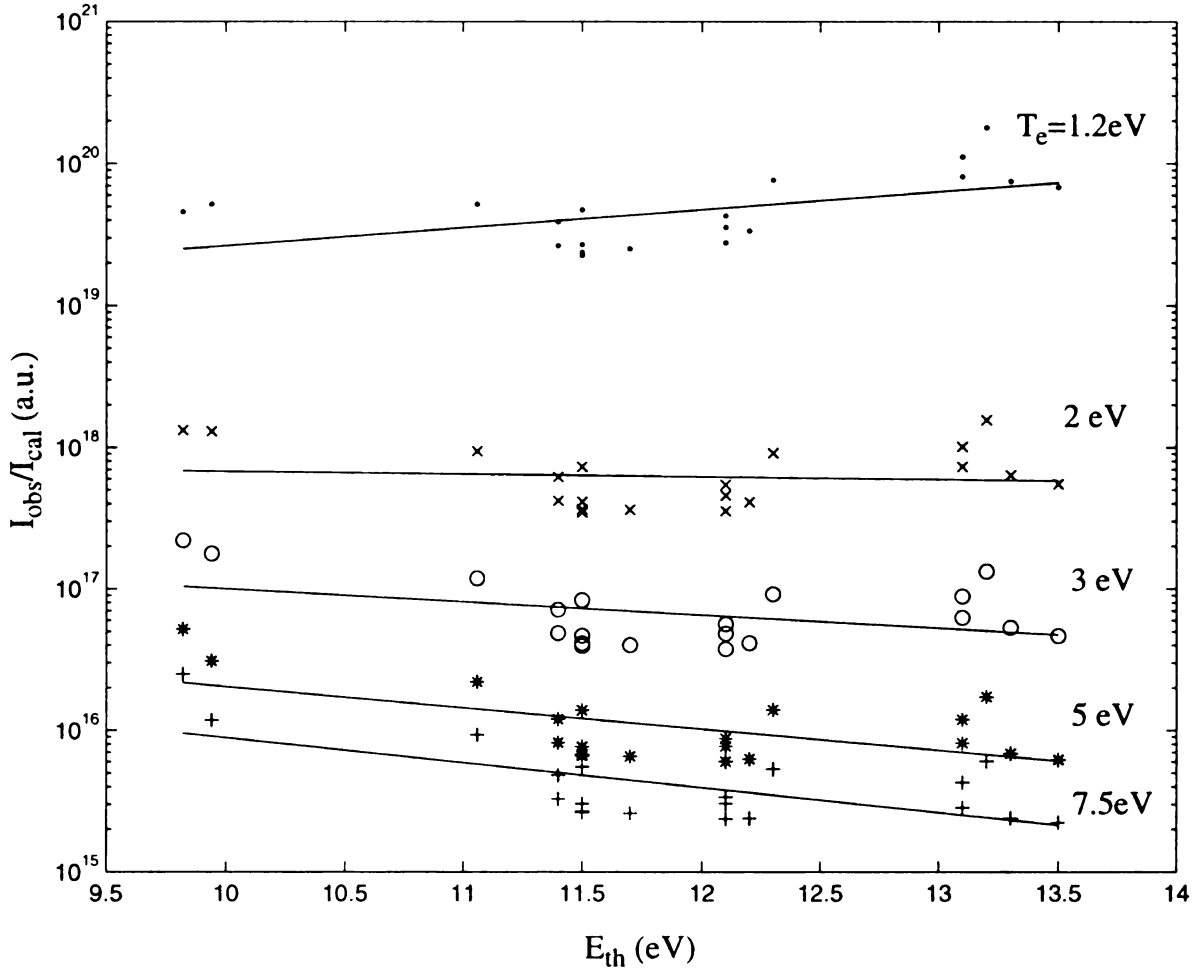

Figure 4.20 Emission ratio of the observed emission line intensities to the calculated line intensities (I_{obs}/I_{cal}) for the hydrogen plasma. The operating pressure is 3 mTorr. The ratios are done for five different T_e's= 1.2, 2, 3, 5, 7.5eV.

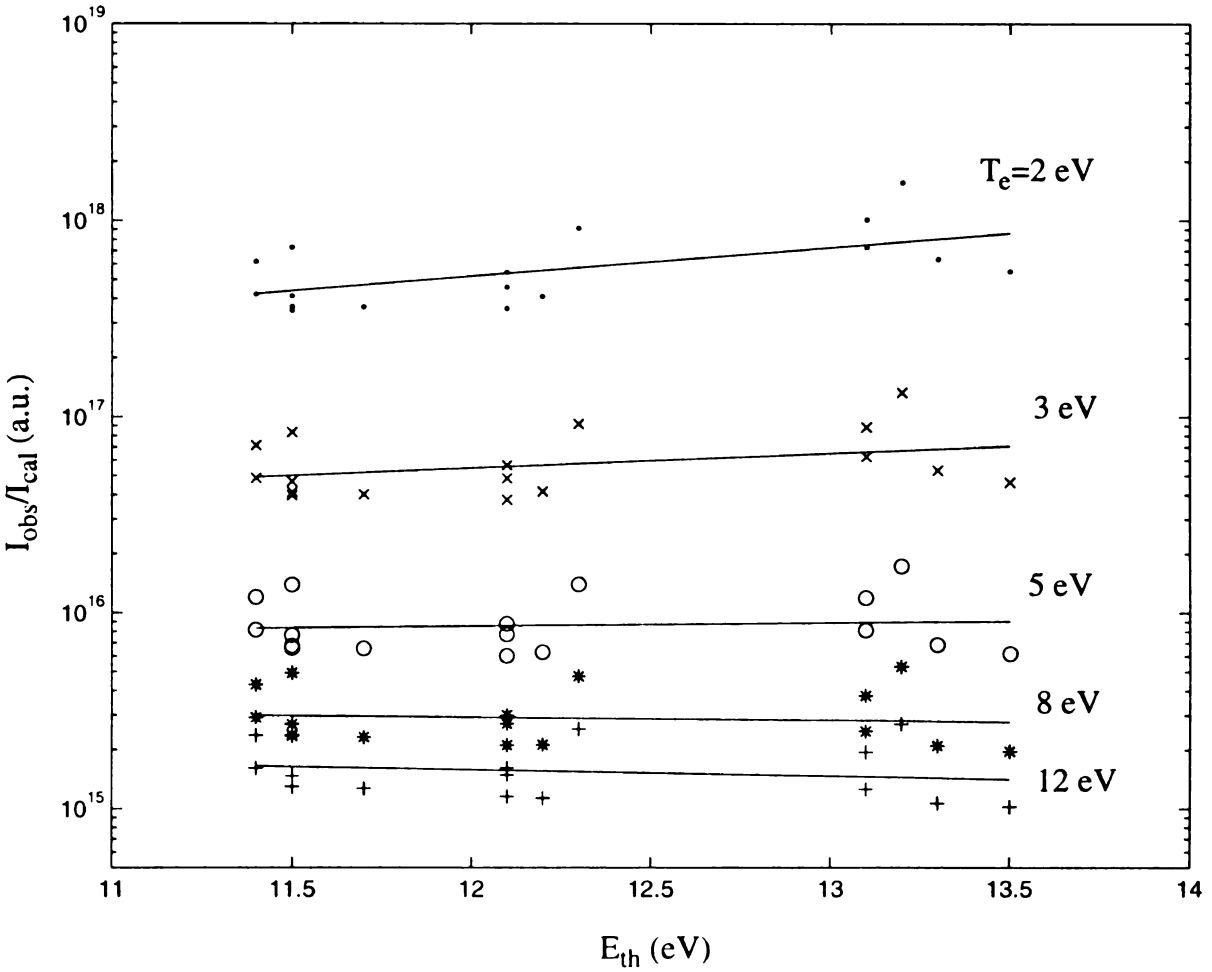

Figure 4.21 Emission ratio of the observed line intensities to calculated line intensities (I_{obs}/I_{cal}) for a hydrogen plasma(excluding xenon emissions). The operating pressure is 3 mTorr. The ratios are done for five different T_e's = 2, 3, 5, 8, 12 eV.

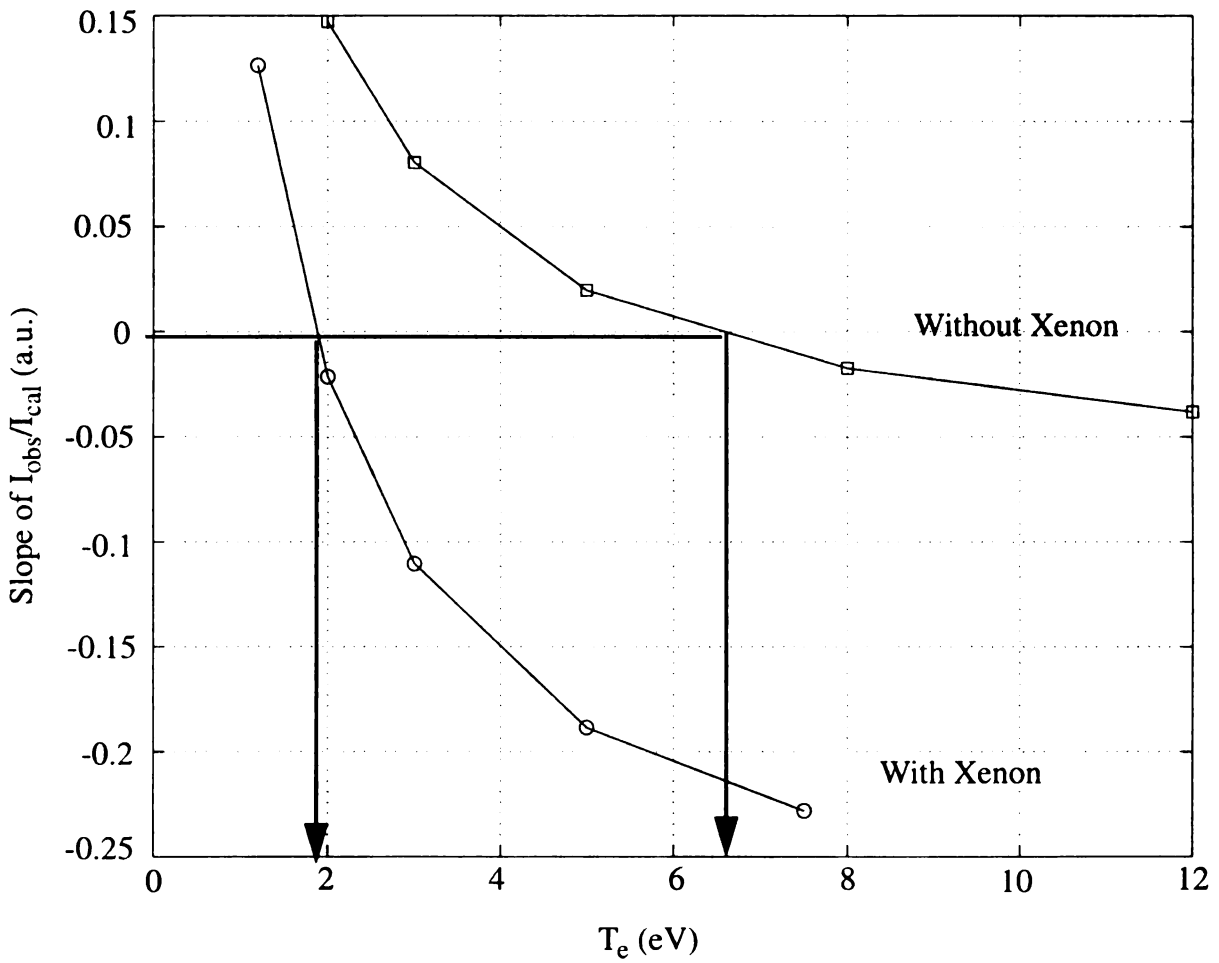

Figure 4.22 Plot of the fitted slopes of the emission ratio lines at five different T_e's(circles : xenon emissions included, squares: xenon emissions excluded). Zero slope indicates the electron temperature in the source.

4.8 Actinometry Results

The actinometry was performed on hydrogen discharges with a small amount of argon (less than 5%) added as the actinometer. The results are shown in Table 4.4 [80]. The relative atomic hydrogen densities are proportional to the intensity ratios of H(486.1 nm) to Ar(656.3 nm) multiplied by argon densities which increased as the pressures increased from 1.1 to 5.3 mTorr. The absolute values of the atomic hydrogen densities can be found using Eqn. (3.30) once the electron temperatures in the source are known. This will be done in Chapter 6.

Table 4.4 The emission ratios of H (486.1nm) to Ar (750.4nm) in H_2 discharges from actinometry (5% of argon gas added).

Pressure (mTorr)	63W	90W
1.14	.2134	.2401
1.4	.2068	.2081
1.6	.1844	.1954
2.0	.1759	.2201
2.4	.2921	.2073
2.8	.2938	.1908
3.5	.2939	.2896
5.3	.2893	.2988

CHAPTER 5

Modeling of the MPDR 610 Plasma Source

5.1 Introduction

The modeling of the plasma discharge in the source region is done using a global [81] or zero-dimensional model in this thesis. This model considers charged particle balance and energy balance in the source region. This chapter begins with a description of the global model and its general expression for most types of gas discharges. Next the models for the plasma sources of different types of gases are developed followed by the determination of some selected parameters in the model from the experimental data. After the appropriate particle and energy balance equations are determined for each type of gas discharge, and arranged in a linear system of equations, the desired discharge properties/ parameters are computed from the set of equations using a numerical method. In addition, a model for the charged particle densities in the chamber region where the substrate is usually located during the processing in a microwave plasma system is considered later in this chapter. The model uses a two-dimensional steady state finite difference method to solve the ambipolar diffusion equation. A comparison of the experimental data and model results will be given and discussed in the next chapter.

5.2 Discharge Global Models : A General Expression

This model is based on the development of Lieberman et al. in 1995 [81]. The two main sets of equations considered in the global models are the power balance and particle balance for all species of interest. These equations are summarized as the following:

(1) Power Balance Equations

The general form of the total power balance equation is

$$P_{abs} = P_{ev} + P_{iw} + P_{ew} \tag{5.2}$$

where P_{abs} is the power absorbed by the system, P_{ev} is the electron energy loss due to all electron-neutral collision processes in the discharge volume, P_{iw} is the ion energy loss to the walls, and P_{ew} is the electron energy loss to the walls. This power balance between the system absorbed power which comes from the external power source (dc, rf, or microwave) and power consumed in the plasma volume (electron-neutral collisions and charged species energy loss to the wall) is illustrated in Fig. 5.1a.

Ion energy is lost to the wall due to ions flowing to the walls at a characteristic velocity which is the Bohm velocity $u_B=(eT_e/M)^{1/2}$ at the plasma sheath edge. With the ion velocity known, then

$$P_{iw} = en_{is}u_B A\varepsilon_{iw} \tag{5.3}$$

where n_{is} is the ion sheath edge density. A is the surface area of the chamber wall, and ε_{iw} is the ion kinetic energy loss per ion lost to the wall. Similarly, the electron energy loss to the walls is

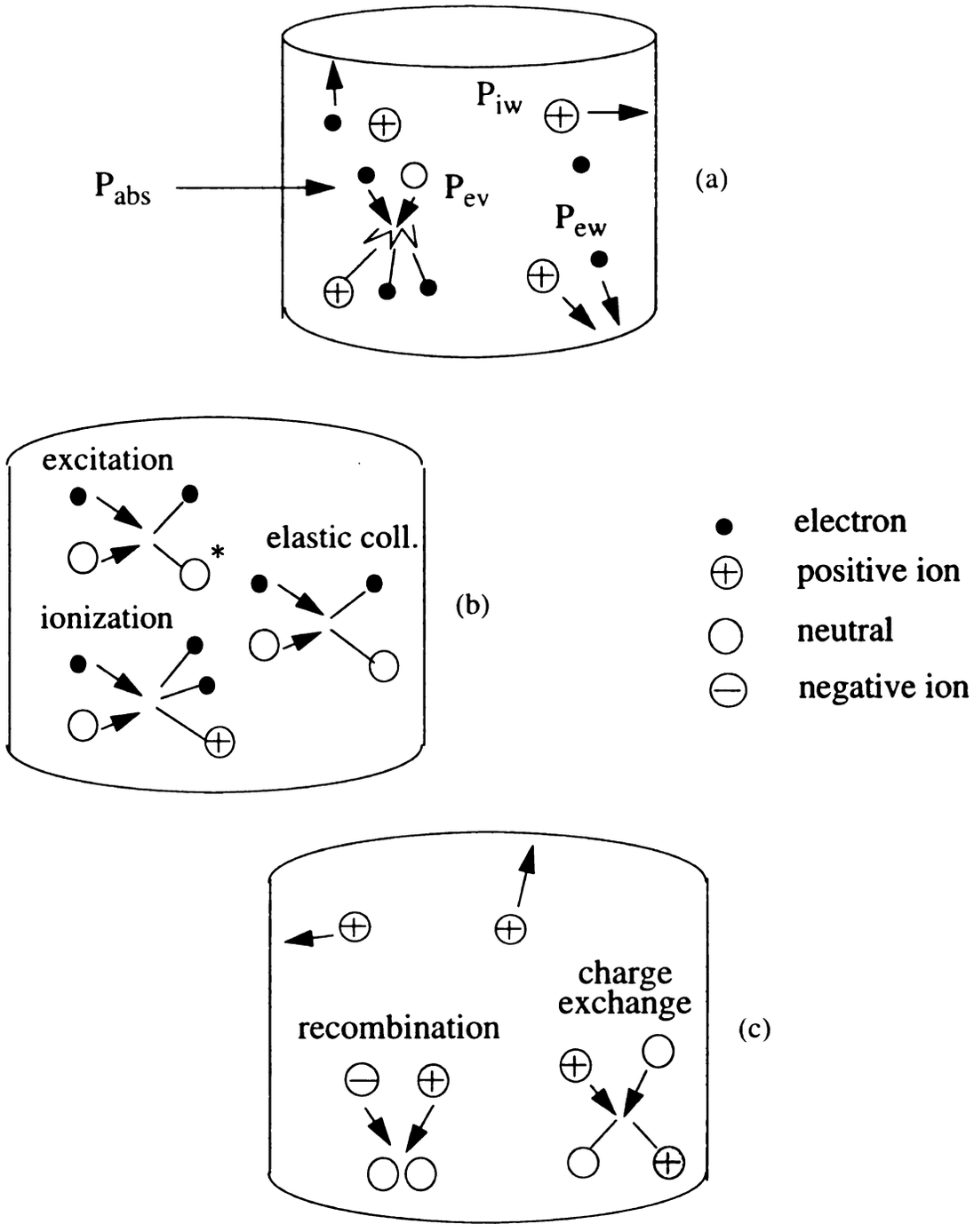

Figure 5.1 Illustration of power balance in the plasma volume (a), electron-neutral collision process (b), and charged particle balance in the discharge volume (c).

$$P_{ew} = en_{es}u_B A\varepsilon_{ew} \tag{5.4}$$

where ε_{ew} is the electron kinetic energy loss per electron lost to the walls, and n_{es} is the electron sheath edge density.

For an atomic gas, the energy loss ε_L per electron-ion pair created due to all electron-neutral collision processes can be expressed as

$$\nu_{iz}\varepsilon_L = \nu_{iz}\varepsilon_{iz} + \sum_{k=1}^{N_{exc}} \nu_{exc,k}\varepsilon_{exc,k} + \nu_{elas}\frac{3mT_e}{M} \tag{5.5}$$

where $\nu = \langle \sigma v \rangle n_n$ is the appropriate collision frequency including ionization, excitation, and elastic collision, $\langle \sigma v \rangle$ is the rate coefficient, n_n is the neutral density, and N_{exc} is the number of excitation energy loss channels. The first term on the right-hand side of Eqn. (5.4) is the energy loss due to the ionization of neutral atoms with an ionization threshold energy of ε_{iz}, the second term represents the total energy loss due to excitation of neutral atoms to various excited states with threshold energies ε_{exc}, and the last term is the energy loss due to electron-neutral elastic scattering. These three types of electron energy loss mechanism due to electron-neutral collisions are illustrated in Fig. 5.1b.

For molecular gases, several additional considerations need be made including:

(a) The generation of multiple positive ions.

(b) Fragmentation of the neutral molecule can provide multiple neutral sources for the generation of ions.

(c) Generation of negative ions.

(d) Additional energy loss channels such as dissociation, and particle loss

channels such as positive-negative ions recombination, need to be included. These require the modification of Eqns. (5.1) and (5.4). Eqn. (5.1) is rewritten as

$$P_{abs} = P_{ev} + \sum_{j=1}^{r} P_{iw,j} + P_{ew} \tag{5.6}$$

where r is the number of positive ion species generated in the system. For H_2, r = 3 for the generation of H^+, H_2^+, H_3^+. Eqn. (5.4) is rewritten as

$$\nu_{iz,i}\varepsilon_{L,i} = \sum_{j=1}^{N_{n,i}} \left(\nu_{iz,ij}\varepsilon_{iz,ij} + \sum_{k=1}^{N_{exc,j}} \nu_{exc,kj}\varepsilon_{exc,kj} + \nu_{elas,j}\frac{3mT_e}{M_j} \right) \tag{5.7}$$

where $N_{n,i}$ is the number of neutral species that generate the ith ion. For Ar^+, $N_{n,i}$ = 1 (Ar), and for H^+, $N_{n,i}$ = 2 (H and H_2). $\nu_{iz,ij}$ is the ionization frequency for production of the ith ion from neutral species j, $\nu_{iz,i}$ is the total ionization frequency for production of the ith ion, $\varepsilon_{iz,ij}$ is the threshold ionization frequency for production of the ith ion from neutral species j, and $\varepsilon_{L,i}$ is the total collisional energy loss per electron-ion pair created for the ith ion. The sum over k includes all inelastic electron-neutral collisional processes that do not produce positive ions; e.g., rotational, vibrational and electronic excitation, dissociation, attachment and detachment. The total power loss in the volume therefore is

$$P_{ev} = en_eV \sum_{i=1}^{r} \nu_{iz,i}\varepsilon_{L,i} \tag{5.8}$$

(2) Particle Balance Equation

Using the continuity equation for the ith positive ion which includes ion diffusion loss

to the walls, volume loss due to positive-negative ion recombination, and asymmetric charge exchange (for the case of mixtures), we have

$$Vn_e\nu_{iz,i} = A_{eff,i}n_{is}u_{B,i} + Vk_{recom,i}n_in_- + V\sum_{j=1}^{N_s} k_{ex,ij}n_in_j \tag{5.9}$$

where V is the discharge reactor volume, $k_{recom,i}$ is the recombination rate coefficient, $k_{ex,ij}$ is the charge-exchange rate coefficient for asymmetric collisions between the ith ion and jth neutral, and n^- is the negative-ion density. The balance between the creation of the ion and the loss of it due to the above loss channel in Eqn. (5.8) is illustrated in Fig. 5.1c.

Under the quasineutral condition, the densities at the sheath edge are related by

$$n_{es} = \sum_{i=1}^{r} n_{is} \tag{5.10}$$

Substituting Eqn. (5.9) into Eqn. (5.3) and Eqn. (5.8) into Eqn. (5.7), the total power balance of Eqn. (5.5) becomes

$$P_{abs} = \sum_{i=1}^{r} en_i\left(A_{eff}\varepsilon_{T,i}u_{B,i} + k_{recom,i}n_-\,\varepsilon_{L,i}V + \sum_{j=1}^{N_s} k_{ex,ij}n_j\varepsilon_{L,i}V\right) \tag{5.11}$$

where

$$A_{eff} = \left.\frac{n_{is}}{n_i}\right|_{axial} 2\pi R^2 + \left.\frac{n_{is}}{n_i}\right|_{radial} 2\pi RL \tag{5.12}$$

is the effective surface area for ion loss and

$$\varepsilon_{T,i} = \varepsilon_{L,i} + \varepsilon_{iw} + \varepsilon_{ew} \tag{5.13}$$

The ratio of sheath edge density n_{is} to the bulk average density n_i is

$$h_L = \left.\frac{n_{is}}{n_i}\right|_{axial} \approx 0.86\left(3 + \frac{L}{2\lambda_i}\right)^{-1/2} \tag{5.14}$$

at the axial sheath edge (z=0 and z=L) and

$$h_R = \left.\frac{n_{is}}{n_i}\right|_{radial} \approx 0.8\left(4 + \frac{R}{\lambda_i}\right)^{-1/2} \tag{5.15}$$

at the radial sheath edge (r = R). Here R and L are the radius and length of the discharge, and $\lambda_i = (n_g\sigma_i)^{-1}$ is the ion mean free path. Eqns.(5.13) and (5.14) are valid for electropositive discharge in low to intermediate pressure regime, where $2\lambda_i/L \geq T_i/T_e$ and $\lambda_i/R \geq T_i/T_e$ respectively. For T_i = 0.5 eV, T_e = 5 eV, and discharge dimension of R = 3.6 cm and L = 3 cm, λ_i should be no less than 0.15 cm for Eqns. (5.13) and (5.14) to be valid. For the detailed derivation of Eqns.(5.13) and (5.14), the reader should refer to Ref. [100],[101].

5.3 Global Models Used in this Dissertation

Models for discharges at lower pressure [84],[85] in the range of 1 mTorr have been created using either full electron energy distribution function (EEDF) solutions or Maxwellian distribution function based solutions. A condition generally considered as necessary for using the Maxwellian distribution is that elastic (electron-electron) collisions dominate over inelastic collisions. The dominance of elastic collisions requires ionization ratios of greater than 10^{-4}[85]. In the discharge considered in this study, the

ionization ratios are typically 10^{-2} to 10^{-3}. This thesis therefore uses the assumption of a Maxwellian distribution.

5.3.1 Argon Discharge Global Models

For argon plasmas, the ionization reaction considered in the model is

$$e + Ar \rightarrow Ar^{+} + 2e \tag{5.16}$$

The electron ionization rate constant K_{iz} in this reaction can be approximated to an Arrhenius form over a limited range of T_e (<100 eV) [82]

$$K_{iz} \approx K_0 e^{-E_{iz}/T_e} \tag{5.17}$$

where $K_0 \approx 6x10^{-14}$ m^3/s is the pre-exponential factor for argon, and E_{iz}=15.76 eV is the ionization energy of argon.

The discharge model is developed first by considering the particle balance in the argon plasma. Three models of charged particle confinements are considered including: (1) no magnetic confinement, (2) magnetic confinement at the side wall, and (3) both magnetic confinement at the side wall and additional ionization created by primary electrons trapped in the magnetic mirror. These three cases are discussed separately as follows:

(1) Particle Diffusion Without Magnetic Confinement

The argon discharge model for the plasma created with MPDR 610 followed from the derivation in the previous section is explained as follows. The particle balance equation considers equating the total species surface loss and the total volume generation of species

via ionization in the source, giving

$$n_i u_B A_{eff} = V K_{iz}(T_e) n_e n_g \tag{5.18}$$

where $A_{eff} = 2\pi R(Rh_l + lh_R)$ is the effective area accounting for possible different plasma densities at axial and radial sheath edges. V is the total volume of the plasma source. The plasma density in the source is denoted as n_i, and $n_i = n_e$ in the argon discharge. n_g is the neutral density. Eqn.(5.17) can be rewritten as

$$\frac{K_{iz}(T_e)}{u_B(T_e)} = \frac{1}{n_g d_{eff}} \tag{5.19}$$

where

$$d_{eff} = \frac{1}{2}\frac{Rl}{Rh_i + lh_R} \tag{5.20}$$

Using Eqn.(5.16) for $K_{iz}(T_e)$, Fig. 5.2 plots T_e vs. $n_g d_{eff}$ for electron temperatures of 1 to 20 eV. The model without magnetic confinement is denoted as $f_{loss} = 1$ in Fig. 5.2. Once n_g and d_{eff} are given, the electron temperature can be determined from it.

(2) Particle Diffusion With Magnetic Confinement

When a static magnetic field exists around the wall of the quartz discharge region, which is the case in the MPDR 610 plasma source, the charged particle diffusion to the wall is reduced due to magnetic confinement. This reduced charge particle flux to the walls is treated by multiplying a fractional loss term, f_{loss}, on the LHS of Eqn. (5.18), giving

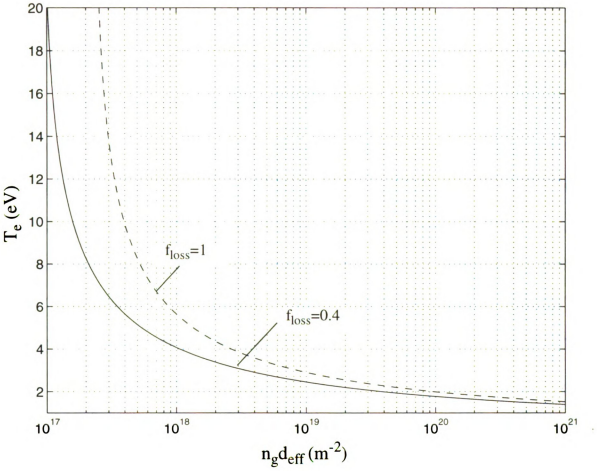

Figure 5.2 The universal plot of T_e vs. $n_g d_{eff}$ in an argon gas discharge.

$$f_{loss} n_i u_B A_{eff} = V K_{iz} n_i n_g \tag{5.21}$$

The f_{loss} term is introduced here to account for the effective fractional loss of electron-ion pairs loss to the wall due to permanent magnets applied around the MPDR 610 source for plasma confinement [105],[106]. The determination of f_{loss} value is based on the arrangement of permanent magnets around the quartz discharge region of MPDR 610. The charged particle loss fraction to the wall f_{loss} with magnetic field confinement is determined by first considering a cylindrical discharge volume of radius R = 1.8 cm and length L = 3.0 cm. It has a total surface diffusion area of $A_t = 2\pi (R^2 + RL) = 54.28$ cm^2. The static magnetic field at the MPDR 610 discharge region provides side wall confinement of the charged particles with an area equals to 33.93 cm^2. For complete confinement on the side wall, the fractional loss will be (54.28-33.93) / 54.28 = 0.37. If there is a small leak of diffusion loss to the side wall, we will expect an adjustment of the f_{loss} value. In the argon plasma model the value of f_{loss} is chosen to be 0.4.s Similarly, Eqn. (5.20) can be rearranged as

$$\frac{K_{iz}(T_e)}{u_B(T_e)} = \frac{f_{loss}}{n_g d_{eff}} \tag{5.22}$$

where d_{eff} is as defined in Eqn. (5.19). Again using Eqn.(5.16) for $K_{iz}(T_e)$, Fig. 5.2 plots T_e vs. $n_g d_{eff}$ with $f_{loss} = 0.4$. The electron temperature can be determined from Fig. 5.2 if n_g and d_{eff} are given.

(3) Particle Diffusion With Magnetic Confinement and Additional Ionization from Trapped Electrons

In addition to the reduced diffusion of charged particle to the wall, the existance of a static magnetic field in the discharge region can provide much better trapping of ionization electrons (the electrons at the high energy tail of its distribution) because of their much smaller mass and high energies compared with those of ions. Therefore these electrons can provide an additional ionization in the discharge. Here another term is added in the RHS of Eqn. (5.20) to account for this ionization, giving

$$f_{loss} n_i u_B A_{eff} = V K_{iz} n_e n_g + V f_{iz} K_{iz} f_e n_e n_g \tag{5.23}$$

where f_{iz} is the additional fractional rate of ionization caused by those electrons. f_e is the fraction of electrons trapped in the magnetic field with respect to the total number of electrons created in the plasma. f_{iz} can be approximated as proportional to the lifetime ratio of trapped electrons to untrapped electrons, which is

$$f_{iz} \propto \left(\frac{\tau_{trapped}}{\tau_{untrappeed}} \right) \propto \frac{\lambda_e}{R} \tag{5.24}$$

where R is the radius of the discharge volume, which is a constant. λ_e is the mean free path of electrons which is inversely proposal to the discharge pressure. Eqn.(5.22) can then be rearranged as

$$V K_{iz} n_i n_g \left(1 + f_e \frac{c_0 \lambda_e}{R} \right) = f_{loss} n_i u_B A_{eff} \tag{5.25}$$

where c_0 is an arbitrary constant. Combine f_e, and c_0/R to a constant c, Eqn. (5.24) can be written as

$$V K_{iz} n_i n_g \left(1 + \frac{c}{p} \right) = f_{loss} n_i u_B A_{eff} \tag{5.26}$$

where p (in mTorr) is the gas pressure. The determination of c is based on the Langmuir probe experimental results. Using the downstream electron temperature data as shown in Fig. 4.15, the electron temperature in the source can be determined by an extrapolation of the T_e curve to z = 0 cm. For argon, the electron temperature in the source is about 5.9 eV at 1 mTorr. The choosing of the c value is to match this temperature at the same pressure in the model. In this argon discharge model, the value of c is determined to be 0.17.

For the power balance equation, since there is no negative-positive ion recombination or charge exchange between ions and neutrals (the reaction rate constants $K_{recom} = K_{ex} = 0$), Eqn. (5.10) is simplified to

$$P_{abs} = en_i A_{eff} E_T u_B \tag{5.27}$$

for the case of without magnetic field confinement for charged particle. For a discharge with a static magnetic field

$$P_{abs} = en_i f_{loss} A_{eff} E_T u_B \tag{5.28}$$

and again $E_T = E_L + E_{iw} + E_{ew}$. For Maxwellian electrons, the mean kinetic energy loss to the walls per electron loss is $E_{ew} = 2T_e$. The mean kinetic energy loss per ion loss is the sum of the ion energy entering the sheath and the energy that the ion gains as it travels through the sheath. The ion velocity entering the sheath is u_B, the Bohm velocity. It corresponds to an energy of $T_e/2$. The potential drop within the sheath between a plasma and a floating wall can be expressed as [51]

$$V_s = T_e \ln\left(\frac{M}{2\pi m}\right)^{1/2} \tag{5.29}$$

For argon, $V_s = 4.7T_e$. Accounting for the ion energy when entering the sheath, we have

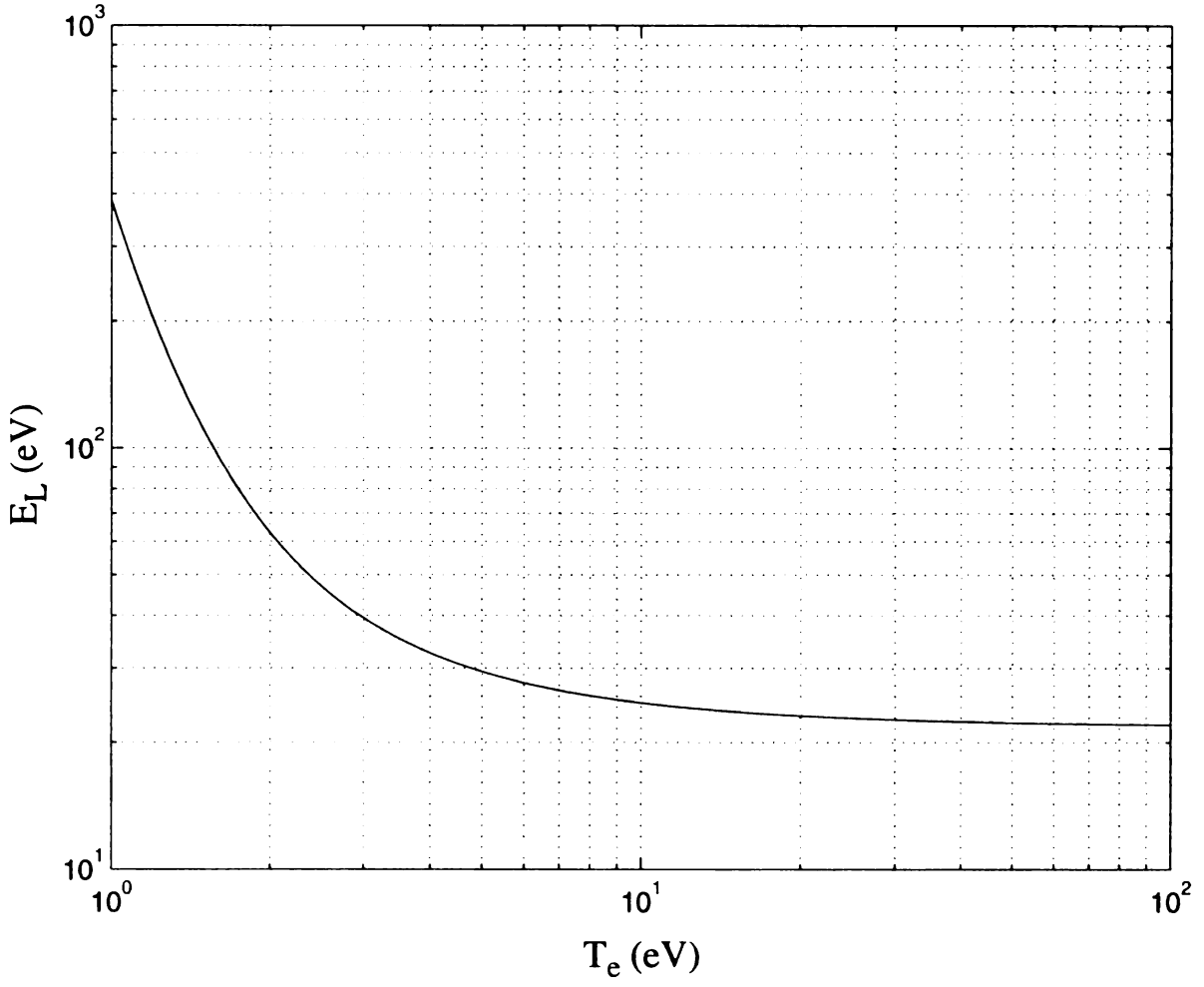

Figure 5.3 The collisional energy loss per electron-ion pair created vs. T_e in the argon plasma.

$$E_{iw} = \frac{T_e}{2} + V_s \tag{5.30}$$

In the case of argon, $E_{iw} = 5.2T_e$. Using the T_e determined earlier from Fig. 5.2, the collisional energy loss E_L is obtained from Eqn. (3.5.8) in Ref. [83]

$$K_{iz}E_L = K_{iz}E_{iz} + K_{exc}E_{exc} + K_{el}\frac{3m}{M}T_e \tag{5.31}$$

where $K_{exc}(T_e)$ is obtained by using the similar approximation for $K_{iz}(T_e)$ in Eqn. (5.16),

$$K_{exc} \approx 2x10^{-14} e^{-E_{exc}/T_e} \ (\mathrm{m^3/sec}) \tag{5.32}$$

where $E_{exc} \approx 11.55$ eV is the excitation threshold energy for argon. And for elastic scattering, K_{el} is approximated by

$$K_{el} \approx 1x10^{-13} \ (\mathrm{m^3/sec}) \tag{5.33}$$

for $T_e > 1$ eV. Fig. 5.3 plotted the collisional energy loss, E_L vs. T_e for an argon discharge. After E_T is calculated, the plasma density can be found from Eqn. (5.27).

5.3.2 Hydrogen Discharge Global Models

Several hydrogen discharge kinetic and chemical reaction models were developed in the past by various researchers [84-88]. They cover a wide pressure range from sub mTorr - 100 Torr. In order to select the appropriate kinetics, species, and reactions for the low pressure range and compact plasma source studied here, we will first consider typical expected collision rates in the compact plasma source. Then these collision rates are compared to the residence time of the species in the plasma which for a flow rate of 30

sccm, plasma discharge volume of 50 cm^3, and a pressure of 1 mTorr is on the order of 10^{-4} seconds. First, an estimate of the neutral-neutral collision rate based on a gas temperature of 400 K, a pressure of 1 mTorr and a collision cross section of 10^{-19} m^2 [89] gives a collision frequency on the order of 10^4 Hz. This corresponds to a mean time between collisions also on the order of 10^{-4} seconds. Next an estimate of the electron-neutral collision frequency for producing excitations or ionization by electrons of energy in the range of 10-30 eV is considered. In this energy range the inelastic collision cross section is in the range of 10^{-20} m^2 [94] and the collision frequency is on the order of 10^5 Hz. This is about 10 times larger than the neutral-neutral collision frequency. Hence the first assumption made is that the primary reaction kinetics are electron-neutral collisions because of the higher electron-neutral collision frequency and the short residence time of neutrals which limits the possibility of neutral-neutral chemical reactions.

The next selection to be made in the model is the species to include. This selection is made based on the species that occur due to direct electron excitation or ionization. The species included are H_2, H, H^+, H_2^+, and H_3^+. The species specifically not included in the model is H^-. In the case of H^-, the dominate mechanism of H^- creation for the conditions in the compact source studied here is dissociative attachment [88]

$$e + H_2(v) \rightarrow H(1s) + H^- \ (v \geq 4)$$

The cross section for this process depends strongly on the vibrational state of the hydrogen. For example, for the v=0 vibrational state the cross section is 2.8×10^{-25} m^{-2} but for the v>4 states the cross section is greater than 10^{-20} m^2 [88]. The formation of H^- ions typically requires that the hydrogen molecules first be vibrational excited, then

dissociative attachment can occur. A check of the vibrational excitation cross sections [94] gives values of a few 10^{-21} m^2 for v=0 to v=1 excitation and 10^{-23} m^2 range for excitation to the v>4 range for the 1-10 eV electron energy range. Therefore, the short residence time of the hydrogen gas and the lower cross section for v>4 vibrational excitation prevents the formation of any significant amounts of H^- ions in the plasma source

Summarizing, the neutral and charged species included in this model are electron, molecular hydrogen, atomic hydrogen, H^+, H_2^+ and H_3^+. Table 5.1 lists the reactions used in the hydrogen discharge model in the low pressure range (0.5-5 mTorr) where most of the ionizations come from electron-neutral collisional ionizations except for Reaction (6), the surface recombination of atomic hydrogen, and Reaction (8), the generation of H_3^+ which comes from the collision of H_2^+ with H_2. Reactions (2), (3), and (9)-(12) account for the electron impact excitations of H and H_2. Also listed are the required threshold energies of electrons, E_{th}, for applicable reactions. K is the reaction rate constant. The calculation of rate constant in Reaction (5) used a linear fit of Fig. 5 in Ref. [96]. For 3 eV $\leq T_e < 7$ eV,

$$\log(K_{h2\_h}) = 2.002(\log T_e - 0.477) - 14.657 \ (m^3/sec) \tag{5.34}$$

For 7 eV $\leq T_e < 14$ eV,

$$\log(K_{h2\_h}) = 0.808(\log T_e - 0.845) - 13.921 \ (m^3/sec) \tag{5.35}$$

For 14 eV $\leq T_e \leq 100$ eV, $K_{h2\_h} \sim 2.2 \times 10^{-14}$ m^3/sec. For rate constants in Reactions (1)-(4), (7), and (9)-(12), a nine-term polynomial fit is used for K's with the following formula [95]

Table 5.1 List of reactions used in the hydrogen discharge model. Reaction rates are taken from Ref. [95] for reactions 1-4 and 7, 9-12. Reaction rates for reaction 5 and 8 are from Ref. [96] and Ref. [93]. Reaction 6 is developed as found in Ref. [81].

Reactions	E_{th} (eV)	K(m^3/sec)
(1) $e + H \rightarrow e + H^+ + e$	13.6	$K_{iz,11}$
(2) $e + H(1s) \rightarrow e + H^*(2s)$	10.2	$K_{exc,11}$
(3) $e + H(1s) \rightarrow e + H^*(2p)$	10.2	$K_{exc,12}$
(4) $e + H_2 \rightarrow H(1s) + H^+ + 2e$	18.0	$K_{iz,12}$
(5) $e + H_2 \rightarrow e + H(1s) + H$	10.0	$2.2\text{-}22 \times 10^{-15}$
(6) $H + H \rightarrow H_2$ (wall recombination)	-----	$\gamma D_{eff}/\Lambda^2$ (s^{-1})
(7) $e + H_2 \rightarrow e + H_2^+ + e$	15.4	$K_{iz,2}$
(8) $H_2^+ + H_2 \rightarrow H_3^+ + H$	-----	2.11×10^{-15}
(9) $e + H_2(X^1\Sigma_g^+) \rightarrow e + H_2(B^1\Sigma_u^+)$	11.37	$K_{exc,21}$
(10) $e + H_2(X^1\Sigma_g^+) \rightarrow e + H_2(C^1\Pi_u)$	11.7	$K_{exc,22}$
(11) $e + H_2(X^1\Sigma_g^+) \rightarrow e + H_2(E^1\Sigma_g^+, F^1\Sigma_g^+)$	12.2	$K_{exc,23}$
(12) $e + H_2(X^1\Sigma_g^+) \rightarrow e + H_2(a^3\Sigma_g^+, b^3\Sigma_u^+, c^3\Pi_u)$	10.0	$K_{exc,24}$

$$\ln K = \sum_{n=0}^{8} b_n (\ln T_e)^n \ (\mathrm{cm}^3/\mathrm{sec}) \qquad (5.36)$$

The coefficients b_n and the minimum temperature T_{min} (in eV) that was fit for each reactions are listed as follows

Reaction (1):

b_0=-3.27140x10^1 b_1=1.35366x10^1 b_2=-5.73933 b_3=1.56315 b_4=-2.87706x10^{-1}
b_5=3.48256x10^{-2} b_6=-2.63198x10^{-3} b_7=1.11954x10^{-4} b_8=-2.03915x10^{-6}
T_{min}=2.00

Reaction (2):

b_0=-2.81495x10^1 b_1=1.00983x10^1 b_2=-4.77196 b_3=1.46781 b_4=-2.97980x10^{-1}
b_5=3.86163x10^{-2} b_6=-3.05169x10^{-3} b_7=1.33547x10^{-4} b_8=-2.47609x10^{-6}
T_{min}=1.26

Reaction (3):

b_0=-2.83326x10 b_1=9.58736 b_2=-4.83358 b_3=1.41586 b_4=-2.53789x10^{-1}
b_5=2.8007x10^{-2} b_6=-1.87141x10^{-3} b_7=6.98667e-5 b_8=-1.12376x10^{-6}
T_{min}=0.10

Reaction (4):

b_0=-3.83460x10 b_1=1.42632x10 b_2=-5.82647 b_3=1.72794 b_4=-3.59812x10^{-1}
b_5=4.82220x10^{-2} b_6=-3.9094x10^{-3} b_7=1.73878x10^{-4} b_8=-3.25284x10^{-6}
T_{min}=3.98

Reaction (7):

b_0=-3.56864x10 b_1=1.733469x10 b_2=-7.76747 b_3=2.21158 b_4=-4.16984x10^{-1}
b_5=5.08829x10^{-2} b_6=-3.83274x10^{-3} b_7=1.61286x10^{-4} b_8=-2.89339x10^{-6}
T_{min}=2.00

Reaction (9):

b_0=-3.0819x10 b_1=1.03887x10 b_2=-4.25977 b_3=1.18123 b_4=-2.27751x10^{-1}
b_5=2.90058x10^{-2} b_6=-2.28759x10^{-3} b_7=1.00435x10^{-4} b_8=-1.86993x10^{-6}
T_{min}=2.00

Reaction (10):

b_0=-3.3482x10 b_1=1.3717x10 b_2=-5.92261 b_3=1.70972 b_4=-3.50523x10^{-1}
b_5=4.83438x10^{-2} b_6=-4.13141x10^{-3} b_7=1.94839x10^{-4} b_8=-3.85428x10^{-6}
T_{min}=2.00

Reaction (11):

b_0=-3.64659x10 b_1=1.43036x10 b_2=-6.07443 b_3=1.67731 b_4=-3.12871x10^{-1}
b_5=3.80542x10^{-2} b_6=-2.86001x10^{-3} b_7=1.19964x10^{-4} b_8=-2.14223x10^{-6}
T_{min}=3.16

Reaction (12):

b_0=-2.85801x10 b_1=1.03854x10 b_2=-5.38383 b_3=1.95064 b_4=-5.39367x10^{-1}
b_5=1.00692x10^{-1} b_6=-1.16076x10^{-2} b_7=7.41162x10^{-4} b_8=-2.00137x10^{-5}
T_{min}=1.26

For reaction (6), which describes wall recombination of atomic hydrogen, the hydrogen surface recombination frequency at the wall is computed by using [81]

$$\nu_H = \gamma \frac{D_{eff}}{\Lambda^2} \ (s^{-1}) \tag{5.37}$$

where γ is the recombination coefficient, and

$$D_{eff} = \frac{kT_h}{M\nu_{nn}} \ (m^2/s) \tag{5.38}$$

is the effective diffusion coefficient with T_h being the temperature of atomic hydrogen, M being the hydrogen atom mass, and ν_{nn} being the neutral-neutral collision frequency given

by

$$\nu_{nn} = n_{H2}\sigma\bar{v} \tag{5.39}$$

where σ is the collision cross section of H with H_2. From Fig. 8 of Ref. [89], $\sigma=2\text{x}10^{-19}$ m^2. And

$$\bar{v} = \left[\frac{8kT_h}{\pi m_h}\right]^{1/2} \tag{5.40}$$

is the averaged atomic hydrogen speed assuming a Maxwellian distribution. Lastly, Λ the effective diffusion length is given by

$$\frac{1}{\Lambda^2} = \left(\frac{2.405}{R}\right)^2 + \left(\frac{\pi}{L}\right)^2 \tag{5.41}$$

The discharge region is a cylinder of 3.6 cm in diameter and 3.0 cm in length. The discharge is assumed uniform with magnetic confinement on the side walls and unrestricted diffusion to both ends of the cylinder. Two balance equations are considered including the power balance equation and the particle balance equation. For power balancing, the absorbed power in the plasma must equal to the sum of the power loss in the discharge volume and the power loss by charged species diffusion to the wall. This can be expressed as

$$P_{abs} = en_1 f_{loss} A_{eff,1} u_{B,1} E_{T,1} + en_2 f_{loss} A_{eff,2} u_{B,2} E_{T,2} + en_3 f_{loss} A_{eff,3} u_{B,3} E_{T,3}$$

$$+ Vn_{H2} n_2 K_{ex,23} E_{L,2} \tag{5.42}$$

where $A_{eff,1}$, $A_{eff,2}$, and $A_{eff,3}$ are the effective surface areas at the sheath edge for H^+,

H_2^+, and H_3^+. Here we also introduce f_{loss}, the fraction of diffusing electron-ion pairs loss to the wall, which accounts for trapping of electrons and ions in the source by the magnetic field lines produced by the three ring-shaped permanent magnets placed around the discharge region. For the case of without magnetic field confinement, $f_{loss} = 1$. In a discharge with magnetic field confinement, the value of f_{loss} for MPDR 610 is 0.38 as is explained previously in Section 5.3.1. E_{iw} is the ion energy loss to the wall. From Eqn. (5.28) and (5.29), $E_{iw} = 3.3T_e$ for H^+. For H_2^+ and H_3^+, $E_{iw} = 3.7T_e$ and $3.9T_e$ respectively. $E_{ew} = 2T_e$ is the electron energy loss to the wall for Maxwellian electrons. n_1, n_2, and n_3 are the densities of H^+, H_2^+ and H_3^+. $u_{B,1}$, $u_{B,2}$, and $u_{B,3}$ are the Bohm velocities of H^+, H_2^+, and H_3^+ respectively. $E_T = E_L + E_{iw} + E_{ew}$, where E_L is the collision energy loss per electron-ion pair created. For H^+,

$$E_{L,1} = \frac{1}{\nu_{iz,1}}\left[\nu_{iz,11}E_{iz,11} + \sum_{j=1}^{2}\nu_{exc,1j}E_{exc,1j} + \nu_{elas,1}\frac{3mT_e}{M_1} + \nu_{iz,12}E_{iz,12}\right] \quad (5.43)$$

where $\nu_{iz,11}=n_H K_{iz,11}$ is the ionization frequency corresponding to reaction (1) in Table 5.1, and $E_{iz,11}$ is the ionization threshold energy of the reaction. Similarly, $\nu_{exc,11}= n_H K_{iz,11}$ and $\nu_{exc,12}= n_H K_{iz,12}$ are the excitation frequencies corresponding to reactions (2) and (3) in Table 5.1, and $E_{exc,11}$ and $E_{exc,12}$ correspond to the excitation threshold energies of reactions (2) and (3), respectively. $\nu_{elas,1}= n_H K_{elas,1}$ is the elastic collision frequency between electron and atomic hydrogen. Here hard sphere collisions are assumed, giving

$$K_{elas,1} = \pi(a_H)^2 v_{avg} \quad (5.44)$$

with

$$v_{avg} = \left[\frac{8kT_e}{\pi m_e}\right]^{1/2} \tag{5.45}$$

where $a_H = 0.53 \times 10^{-10}$ (m) is the radius of hydrogen atom. M_1 in Eqn. (5.42) is the mass of H^+. $\nu_{iz,12} = n_{H2}K_{iz,12}$ is the ionization frequency corresponding to reaction (4) in Table 5.1, and $E_{iz,12}$ is the ionization threshold energy of that reaction. $\nu_{iz,1} = \nu_{iz,11} + \nu_{iz,12}$ is the total ionization frequency for creation of H^+. Similarly, for H_2^+

$$E_{L,2} = \frac{1}{\nu_{iz,2}}\left[\nu_{iz,2}E_{iz,2} + \sum_{j=1}^{4}\nu_{exc,2j}E_{exc,2j} + \nu_{elas,2}\frac{3mT_e}{M_2}\right] \tag{5.46}$$

where $\nu_{iz,2} = n_{H2}K_{iz,2}$ is the ionization frequency corresponding to reaction (7) in Table 5.1, and $E_{iz,2}$ is the ionization threshold energy of the reaction. Similarly, $\nu_{exc,21} = n_{H2}K_{exc,21}$. $\nu_{exc,22} = n_{H2}K_{exc,22}$, $\nu_{exc,23} = n_{H2}K_{exc,23}$, and $\nu_{exc,24} = n_{H2}K_{exc,24}$ are the excitation frequencies corresponding to Reactions (9), (10), (11), and (12) in Table 5.1, and $E_{exc,21}$, $E_{exc,22}$, $E_{exc,23}$, and $E_{exc,24}$ correspond to the excitation threshold energies of Reactions (9), (10), (11), and (12), respectively. $\nu_{elas,2} = n_{H2}K_{elas,2}$ is the elastic collision frequency between electron and hydrogen molecules. Here $K_{elas,2} = K_{elas,2}(T_e)$ is found by integrating the elastic scattering cross section of electrons and molecular hydrogen over the electron energies of 1 to 10^3 eV assuming a Maxwellian distribution of electron.

$$K_{elas,2}(T_e) = \langle\sigma(v)v\rangle_v = \left(\frac{m_e}{2\pi kT_e}\right)^{3/2}\int_0^{1000}\sigma(v)v\exp\left(-\frac{mv^2}{2kT_e}\right)4\pi v^2 dv$$

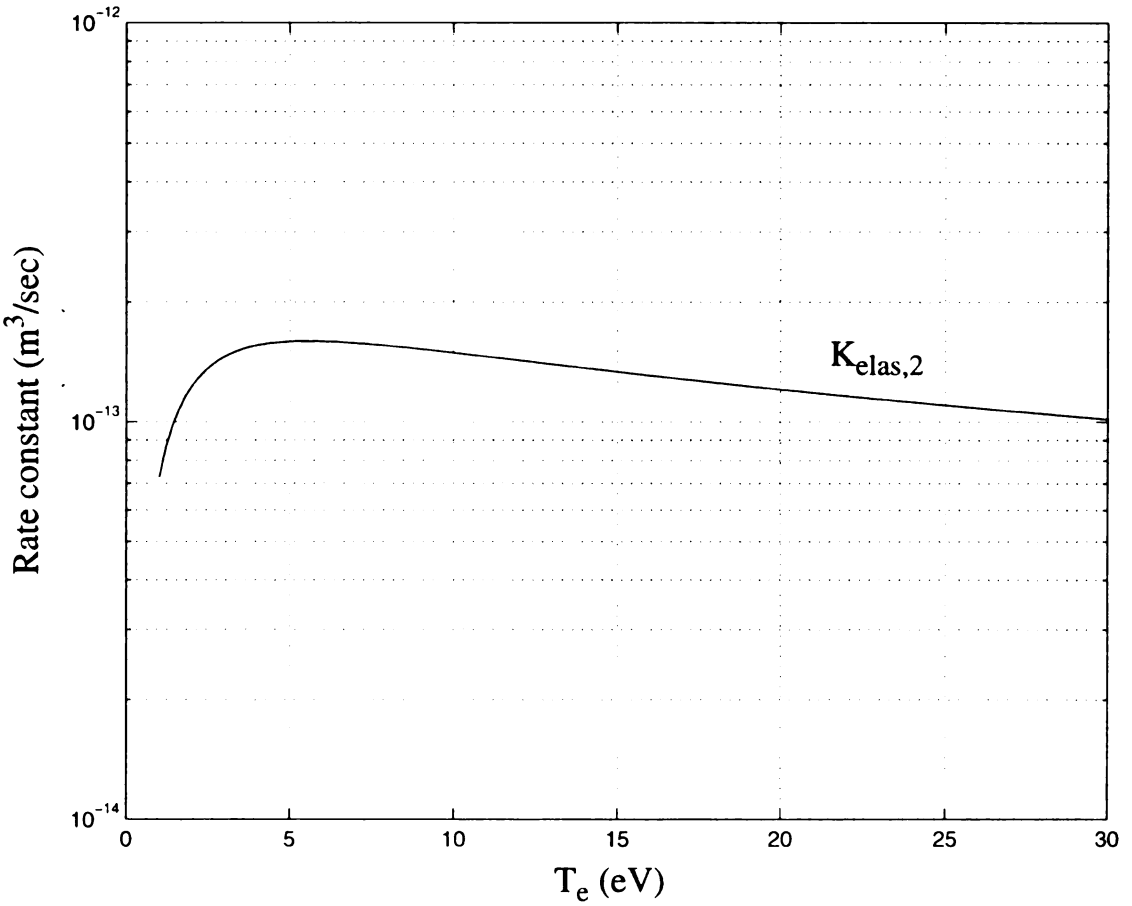

Figure 5.4 The elastic scattering rate of electron collisions with hydrogen molecule.

$$= \left(\frac{m_e}{2\pi k T_e}\right)^{3/2}\left(\frac{8\pi}{m_e^{\,2}}\right)\int_0^{1000}\sigma(E)E\exp\left(-\frac{E}{kT_e}\right)dE \qquad (5.47)$$

The computed result of $K_{elas,2}(T_e)$ from Eqn. (5.46) is plotted in Fig. 5.4. For H_3^+, $E_{L,3} = E_{ew} = 0$ since there is no direct electron impact ionization with H_3 neutrals which do not exist. Hence $E_{T,3} = E_{ew,3}$.

For particle balance, the generation of species in the discharge volume equals the sum of the loss of species within the discharge and the loss of species by recombination on the wall. For H, it is expressed as

$$K_{dissc}n_{H2}n_e = n_H \nu_H + K_{iz,1}n_e n_H \qquad (5.48)$$

for H^+,

$$Vn_e n_H K_{iz,1} + Vn_e n_{H2} K_{iz,12} = f_{loss}A_{eff,1}n_1 u_{B,1} \qquad (5.49)$$

for H_2^+

$$Vn_e n_{H2} K_{iz,2} = f_{loss}A_{eff,2}n_2 u_{B,2} + Vn_{H2}n_2 K_{ex,25} \qquad (5.50)$$

and for H_3^+

$$Vn_2 n_{H2} K_{ex,25} = f_{loss}A_{eff,5}n_5 u_{B,5} \qquad (5.51)$$

where K_{dissc} is the dissociation rate constant of H_2 to H. $K_{iz,1}$ and $K_{iz,2}$ are the ionization rate constant of H and H_2, and $K_{iz,12}$ is the ionization rate constant of H_2 to H^+, and $K_{ex,25}$ is the rate constant of Reaction (8). ν_H is the surface recombination rate of hydrogen atoms, V is the plasma source volume, and n_e is the electron density given by $n_e = n_1 + n_2 + n_3$. The densities of molecular hydrogen and atomic hydrogen are denoted as n_{H2} and

n_H.

Considering another ionization channel from the collisions of trapped primary electrons in the static magnetic field with the neutrals, the charged particle balance equations can be rewritten as

$$K_{dis} n_{H2} n_e (1 + c / p) = n_H \nu_H + K_{iz,1} n_e n_H (1 + c / p) \tag{5.52}$$

for H. And for H^+,

$$V n_e n_H K_{iz,1} (1 + c / p) + V n_e n_{H2} K_{iz,12} (1 + c / p) = f_{loss} A_{eff,1} n_1 u_{B,1} \tag{5.53}$$

for H_2^+

$$V n_e n_{H2} K_{iz,2} (1 + c / p) = f_{loss} A_{eff,2} n_2 u_{B,2} + V n_{H2} n_2 K_{ex,25} \tag{5.54}$$

and lastly for H_3^+

$$V n_2 n_{H2} K_{ex,25} = f_{loss} A_{eff,5} n_5 u_{B,5} \tag{5.55}$$

The determination of the constant *c* is based on the Langmuir probe measurements and OES results for electron temperatures in the hydrogen discharge at some particular discharge conditions. The electron temperature (T_e) at 90 Watt input power and 3 mTorr from OES is about 6.5 eV (see Fig. 4.22), and from the downstream T_e measurements of single Langmuir probe, the electron temperature in the source at a pressure of 1 mTorr is around 7.8 eV by extrapolating the T_e curve in Fig. (4.17) to z = 0 cm. Fitting these values of T_e in the hydrogen discharge model, we get c = 6.5.

For the energy balance and charged particle balance expressions used in the global model, the value of the surface recombination coefficient of atomic hydrogen is difficult to *a prior* determine. For the γ quantity, atomic hydrogen recombination on surfaces depends

on many factors including material type, surface temperature, and surface cleanliness [87,97]. Hence, the ability to just look up the γ value from previous studies does not exist, rather the literature just allows the prediction of a broad range of possible values. In this study we will use measured atomic hydrogen densities together with the model to extract the γ value in the compact plasma source studied. The specific value of γ used in the hydrogen model is discussed in the next chapter.

Table 5.2 Reactions that generates ions or neutrals in the Ar-H_2 mixture discharge models. Species considered: e, Ar, Ar^+, H_2, H, H_3^+ H_2^+, H^+, ArH^+.

Reaction	Rate Constant (m^3/s)	Reference
(1) $Ar + e \rightarrow Ar^+ + e + e$	$6x10^{-14}e^{-15.7/Te}$	81
(2) $H_2^+ + Ar \rightarrow ArH^+ + H$	$1.76x10^{-15}$	90
(3) $e + H_2 \rightarrow H(1s) + H^+ + 2e$	See Table 5.1	95
(4) $e + H_2 \rightarrow e + H(1s) + H$	See Table 5.1	96
(5) $H_2^+ + H_2 \rightarrow H_3^+ + H$	$2.11x10^{-15}$	93
(6) $e + H \rightarrow e + H^+ + e$	See Table 5.1	96
(7) $Ar^+ + H_2 \rightarrow ArH^+ + H$	$8.90x10^{-16}$	90
(8) $ArH^+ + e \rightarrow Ar + H(n=2)$	$5x10^{-15}$	91
(9) $ArH^+ + H_2 \rightarrow H_3^+ + Ar$	$4.5x10^{-16}$	92

Table 5.3 Lists of reactions not included in the discharge model due to small reaction cross sections and therefore large mean free path compared to the dimension of the source.

Reaction	Cross Section $x10^{-20}$ (m^2)	T(eV)	Reference
$H + Ar \rightarrow Ar^+ + H^-$	~0	<20	90
$H + H_2 \rightarrow H + H + H$	~0	<20	89
$H_2 + H_2 \rightarrow H + H + H_2$	~0	<17	89
$H^+ + H_2 \rightarrow H_2^+ + H$	<0.7	<50	89
$H_2^+ + Ar \rightarrow Ar^+ + H_2$	8.6-3.3	0.1-1	90
$H^+ + Ar \rightarrow Ar^+ + H$	~0	<40	90
$Ar^+ + H_2 \rightarrow H_2^+ + Ar$	14.8-7.75	0.1-1	90

5.3.3 Argon-Hydrogen Mixture Discharge Global Models

In addition to the reactions considered in argon and hydrogen discharges, a new ionic species, ArH^+ is taken into account. Also the reactions of charge exchange between positive ions and neutrals need to be considered. A summary of the reactions that generate ions or neutral in the argon-hydrogen discharge model are listed in Table 5.2. These include the direct electron impact ionization and dissociative attachment. The electron-

neutral collisions that result in the excitation of hydrogen are the same as were discussed in the hydrogen global model listed in Table 5.1. The rate constants in Reactions (2) and (7) were calculated from the cross section data in Ref. [90] assuming ions of averaged temperature of T_i = 0.5 eV. And therefore $K_{ex} = \langle\sigma v\rangle = \sigma(2eT_i/M_i)^{1/2}$.

Some neutral-neutral and ion-neutral collisions that were not included in this model are summarized in Table 5.3. The reasons to exclude them in the model are these reactions all have small enough collision cross sections and hence large enough mean free paths (>3.0 cm) compared to the dimensions of the source that they do not occur in large numbers in the discharge.

The particle balance equations for H, H^+, H_2^+, H_3^+, Ar^+, ArH^+ were obtained by equating the generation of species in the discharge to the sum of species loss due to charge transfer/exchange to another species and species loss on wall recombination. For H, it is written as

$$VK_{iz,12}n_{H2}n_e + VK_{ex,34}n_{H2}n_3 + VK_{ex,24}n_{Ar}n_2 + VK_{ex,25}n_{H2}n_2 + VK_{recom}n_4n_e$$

$$= Vn_H\nu_H + VK_{iz,1}n_en_H \tag{5.56}$$

for H^+ :

$$Vn_en_HK_{iz,1} + Vn_en_{H2}K_{iz,12} = f_{loss}A_{eff,1}n_1u_{B,1} \tag{5.57}$$

for H_2^+ :

$$Vn_en_{H2}K_{iz,2} = Vn_{H2}(\, n_2K_{ex,24} + n_2K_{ex,25}) + f_{loss}A_{eff,2}n_2u_{B,2} \tag{5.58}$$

for H_3^+:

$$Vn_2n_{H2}K_{ex,25} + Vn_{H2}\, n_4\, K_{ex,45} = f_{loss}A_{eff,5}n_5u_{B,5} \tag{5.59}$$

for Ar^+:

$$Vn_e n_{Ar} K_{iz,Ar} = Vn_3 n_{H2} K_{ex,34} + f_{loss} A_{eff,3} n_3 u_{B,3} \tag{5.60}$$

for ArH^+:

$$Vn_3 n_{H2} K_{ex,34} + Vn_2 n_{Ar} K_{ex,24} = Vn_e n_4 K_{recom} + Vn_{H2} n_4 K_{ex,45} + f_{loss} A_{eff,4} n_4 u_{B,4} \tag{5.61}$$

and

$$n_e = n_1 + n_2 + n_3 + n_4 + n_5. \tag{5.62}$$

where n_1 denotes the density of H^+, n_2 the density of H_2^+, n_3 the density of Ar^+, n_4 the density of ArH^+, and n_5 the density of H_3^+. n_e is the electron density. n_{H2}, n_H, and n_{Ar} denote the neutral densities of molecular hydrogen, atomic hydrogen, and argon respectively. Considering another ionization channel from the collision of trapped primary electrons in the static magnetic field with the neutrals, the charged particle balance equations can be rewritten as, for H

$$VK_{iz,12} n_{H2} n_e (1 + c_1 / p) + VK_{ex,34}\, n_{H2} n_3 + VK_{ex,24}\, n_{Ar} n_2 + VK_{ex,25}\, n_{H2} n_2 + VK_{recom} n_4 n_e$$

$$= Vn_H \nu_H + VK_{iz,1} n_e n_H (1 + c_1 / p) \tag{5.63}$$

for H^+ :

$$Vn_e n_H K_{iz,1} (1 + c_1 / p) + Vn_e n_{H2} K_{iz,12} (1 + c_1 / p) = f_{loss} A_{eff,1} n_1 u_{B,1} \tag{5.64}$$

for H_2^+ :

$$Vn_e n_{H2} K_{iz,2} (1 + c_1 / p) = Vn_{H2}\, n_2 (K_{ex,24} + K_{ex,25}) + f_{loss} A_{eff,2} n_2 u_{B,2} \tag{5.65}$$

for H_3^+:

$$Vn_2n_{H2}K_{ex,25} + Vn_{H2}\,n_4\,K_{ex,45} = f_{loss}A_{eff,5}n_5u_{B,5} \tag{5.66}$$

for Ar^+:

$$Vn_en_{Ar}K_{iz,Ar}\,(1 + c_2 / p) = Vn_3n_{H2}K_{ex,34} + f_{loss}A_{eff,3}n_3u_{B,3} \tag{5.67}$$

for ArH^+:

$$Vn_3n_{H2}K_{ex,34} + Vn_2n_{Ar}K_{ex,24} = Vn_en_4K_{recom} + Vn_{H2}n_4K_{ex,45} + f_{loss}A_{eff,4}n_4u_{B,4} \tag{5.68}$$

where $c_1 = 6.5$ and $c_2 = 0.17$ as were determined in the hydrogen and argon discharge models.

From Eqn.(5.10), the power balance equation for the mixture model can be written as

$$P_{abs} = \sum_{i=1}^{5} en_i(A_{eff,i}E_{T,i}u_{B,i})$$

$$+ Vn_2(n_{Ar}K_{ex,24} + n_{H2}K_{ex,25})E_{L,2} + Vn_3n_{H2}K_{ex,34}E_{L,3} \tag{5.69}$$

Here $E_{L,1}$ and $E_{L,2}$ are the collisional energy loss per electron-ion pair created for electron collisions with H and H_2 and are as defined in Eqns. (5.42) and (5.45). $E_{L,3}$ is the collisional energy loss for electron collision with Ar and is determined from Fig. 5.3 once the electron temperature in the discharge is known. Since there is no direct electron impact ionization of ArH^+ and H_3^+, $E_{L,4} = E_{L,5} = 0$. Hence the total energy loss $E_{T,4} = E_{iw,4} = 5.19T_e$, and $E_{T,5} = E_{iw,5} = 3.89T_e$ from Eqns. (5.28) and (5.29).

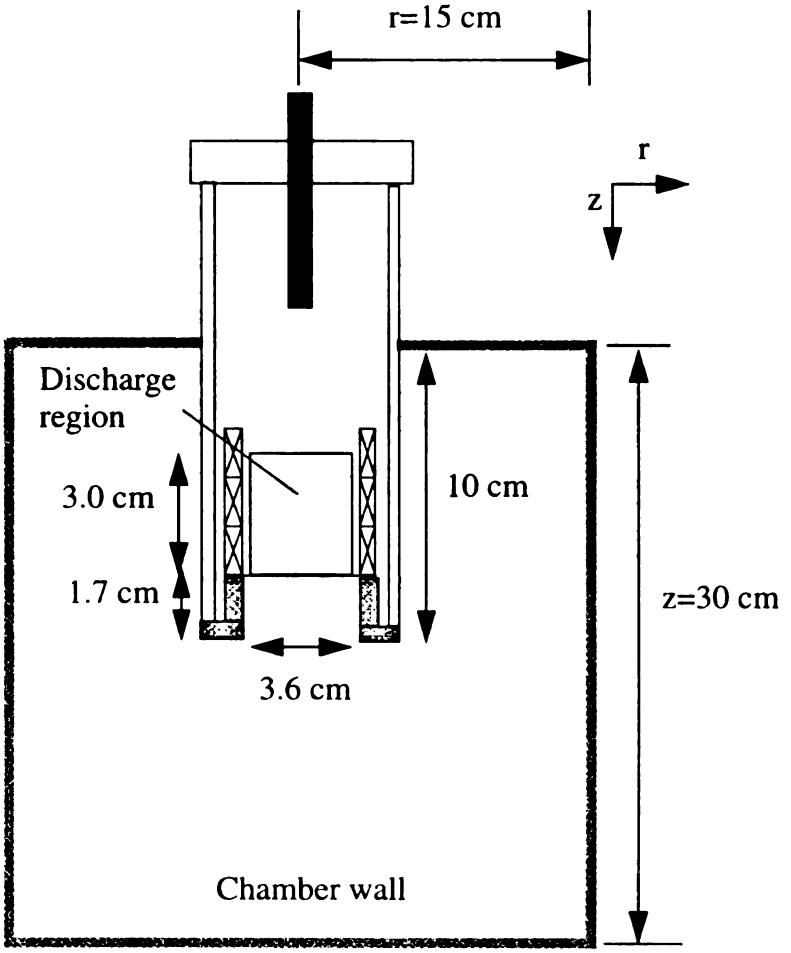

Figure 5.5 The downstream particle diffusion simulation geometry.

5.3.4 Downstream Diffusion Models

A downstream model is constructed as shown in Fig. 5.5 to predict the plasma species density in the region where the substrates being processed are located. A two-dimension cylindrical coordinate system using the r and z coordinates is chosen for the downstream model of charged particle densities. The charge species density is assumed to be symmetric in the ϕ direction. The total area simulated is with r = 15 cm and z = 30 cm. The walls of the downstream chamber and the walls of the compact plasma source are given the boundary conditions that the ion density is zero. The input ion flux to the region is at the exit of the plasma source. The plasma density calculated with the plasma source model is used as the input density value to the downstream model. In the downstream region the ambipolar diffusion equation is solved [98],[99]. The ambipolar diffusion equation can be expressed as

$$\nabla^2 n = \frac{\nu_{iz}}{D_a} \tag{5.70}$$

where n is the positive ion density, ν_{iz} is the ionization frequency, and D_a is the ambipolar diffusion coefficient. This equation does not consider volume recombination processes because of the low pressures.

CHAPTER 6

Modeling Results and Comparison

6.1 Introduction

The results applying the global model to the MPDR 610 plasma source with magnetic confinement in the source region for three different gas discharges are discussed here. Specifically, the modeling results of the Ar, H_2, and Ar-H_2 mixture plasmas using the models developed in Chapter 5 will be presented. The modeled plasma properties are the electron and ion densities, the neutral densities, and the electron temperatures. The power absorption in the discharge by elastic and inelastic collisions (e.g. dissociation, excitation, and ionization etc.) are also discussed. Lastly, the modeling results of particle diffusion in the downstream region using ambipolar diffusion model are presented and compared with the experimental measurements.

6.2 Modeling Results in the Sources Region

The results of discharge properties using the models discussed in the previous chapter with magnetic confinement of charged particle and modified charged particle confinement with additional ionization/dissociation processes due to trapped electrons in the static

magnetic field lines are discussed in the following three subsections each of which corresponds to a different type of gas discharges.

Recall that from Section 5.2 in Chapter 5, the fractional loss term f_{loss} = 0.37 for complete confinement on the side wall. If there is a small leak resulting to the diffusion loss to the side wall, we will expect an adjustment of the f_{loss} value. In the argon plasma model the value of f is chosen to be 0.4 to account for the possible particle loss to the wall. For hydrogen models, the f value is chosen to be 0.38. The reason for a smaller f_{loss} in the hydrogen model than that in the argon model is because argon ions have much larger mass than those of hydrogen, about 20 times, the gyro-radius of the argon ions along the magnetic field lines is larger than that of the hydrogen ions. Therefore the diffusion leak to the wall in the argon plasma is expected to be larger than in the hydrogen plasma [102],[103].

6.2.1 Argon Plasma Model

Fig. 6.1 plots the modeling results of electron temperatures in argon discharges. Two models were used including Model 1: particle diffusion with magnetic field confinement at the wall, and Model 2: particle diffusion with magnetic field confinement at the wall and an additional ionization due to electrons trapped in the magnetic field lines. For the model with a fixed f_{loss} value of 0.4, it predicts a much higher electron temperature at low pressures (especially less than 1 mTorr) compared with the probe measurements done at the downstream position of 2 cm from the source. In the second model, the constant c = 0.17 is used. This value is chosen for a good fit with the electron temperature of around 5.8

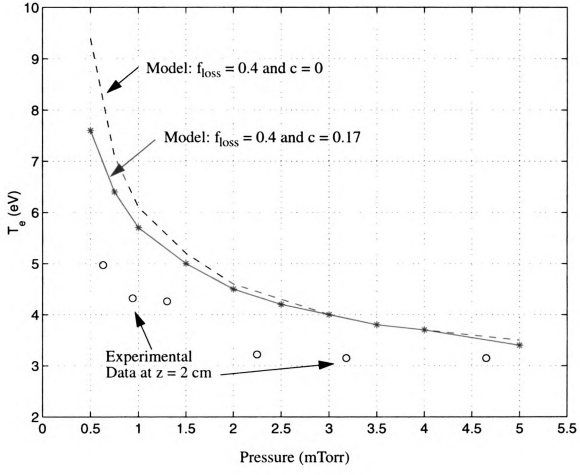

Figure 6.1 The electron temperatures in Ar plasmas. The dashed line is from the model using constant *f* term over the pressure range (Model 1), and the solid line is from Model 2.

eV at a discharge pressure of 1 mTorr from extrapolating the downstream probe measurements of T_e as shown earlier in Fig. 4.15. At higher pressures, the predicted electron temperatures from the two models are very close since the effects of electron-trapping in the magnetic field lines, that is, the (1 + c / p) term accounting for additional ionization due to trapped electrons in the magnetic field lines in Eqns. (5.48)-(5.50), will lessen with higher collision frequencies between the electrons and the neutrals.

The modeled electron densities in the argon plasma sources are plotted in Fig. 6.2. The absorbed powers from the experimental conditions (see Fig. 4.3), which were not uniform over the investigated pressure range, were used in computing the electron densities, n_e , in both of the models for a fixed input power of 90 W. A constant absorbed power of 80 W is also plotted for comparison. In the model of fixed f_{loss}, the electron densities drop down more quickly as the pressures go lower. While in the model of considering additional ionizations from primary electrons, the electron densities are more uniform over the investigated pressure range. This is because at lower pressures the confinement of primary electrons are much better due to less collisions, and as a result, lower the averaged electron temperature as is shown in Fig. 6.1. The ion energy loss to the wall is therefore less with lower electron temperatures. Hence, from Eqn. (5.27) in Chapter 5, the ion densities will become larger compared to the fixed f_{loss} value model (Model 1) for the same absorbed power.

6.2.2 Hydrogen Plasma Model

Fig. 6.3 plots the electron temperatures of hydrogen plasmas over the pressures from

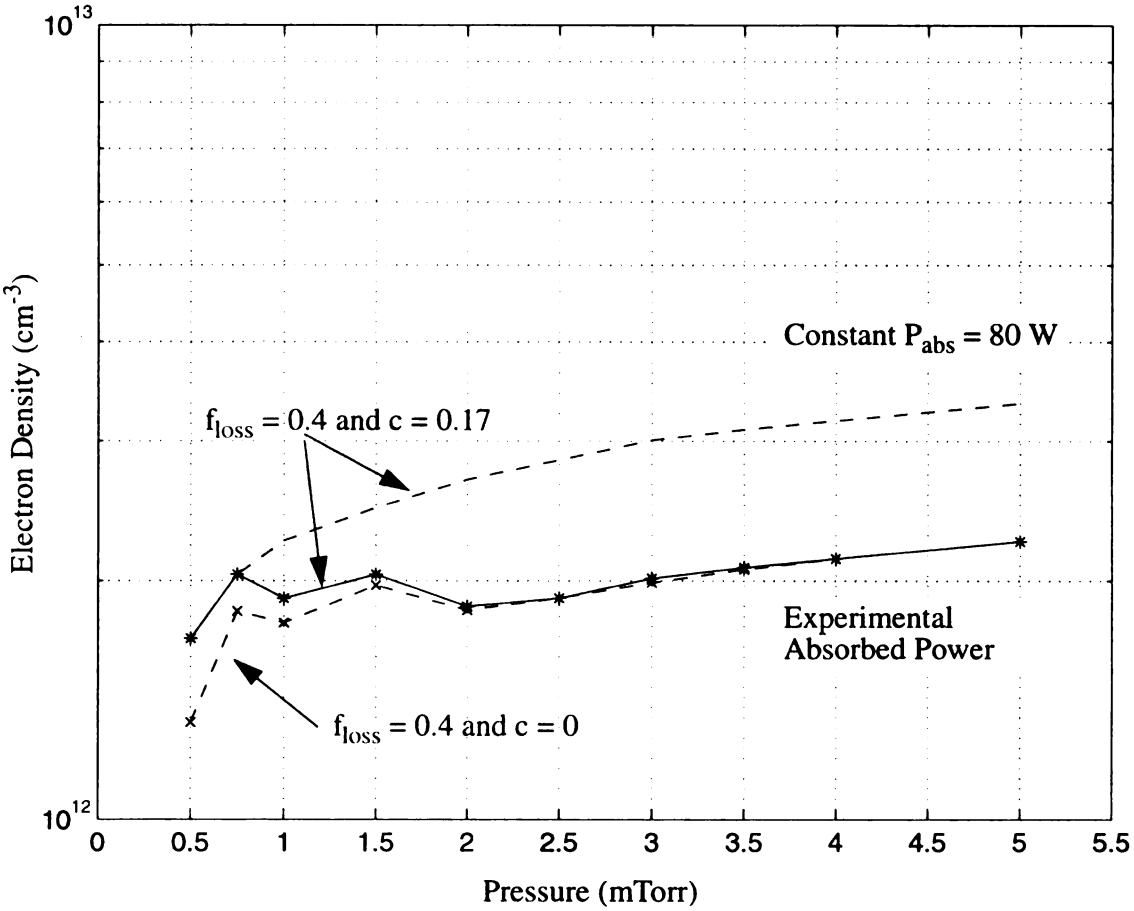

Figure 6.2 The electron densities in Ar plasma. The solid line with (*) is the model using f_{loss}= 0.40 and c= 0.17 and dash line with (x) is the model using constant f_{loss} over the pressure. Both models use the absorbed power corresponding to the experimental conditions. The density with a uniform absorbed power 80 W is also shown.

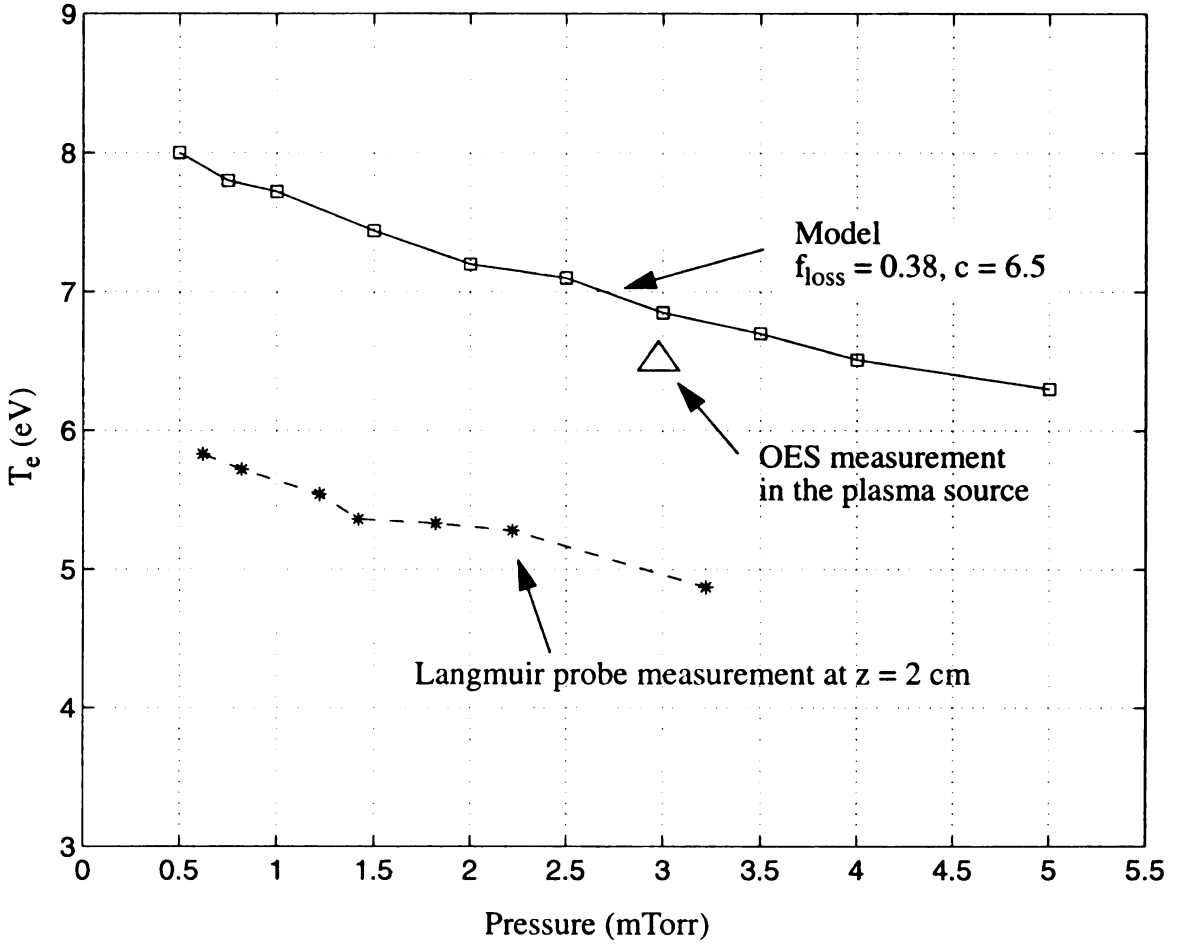

Figure 6.3 Electron temperatures of hydrogen plasma. The solid line is from the model prediction and the dashed line from the probe measurements taken at 2 cm downstream. The discharge conditions are 90 W of input power and 30 sccm of flow rate.

0.5 to 5 mTorr using the model with f_{loss} = 0.38 and c = 6.5. The determination of the loss fraction f_{loss} is described in the beginning of Section 6.2. The constant value c is chosen so that the electron temperatures of the model at pressures 1 mTorr and 3 mTorr and 90 W input powers will match the experimental results both from the probe measurements and optical emission spectroscopy (OES). As it is shown in Fig. 4.17, the source electron temperature at 1 mTorr can be estimated by extrapolating the downstream T_e vs. position curve to z = 0 cm and from the OES of the hydrogen discharge at 3 mTorr as shown in Fig. 4.22. The model with the chosen c value gives T_e = 7.8 eV at 1 mTorr and T_e = 6.9 eV at 3 mTorr both agree in small error with the results from the experiments. For a constant value of the loss fraction f_{loss} = 0.38 and c = 0, there is no reasonable T_e (less than 20 eV) that can be obtained in the model within the lower pressure range. The electron temperatures at 2 cm downstream shown in Fig. 4.11 is also replotted here in Fig. 6.3. The two curves (model prediction and experimental results) show similar trend versus pressure variation with an average difference of about 2 eV higher in the source than in the downstream region. This reduction in electron temperature at the downstream position occurs because (1) the electrons lose energy when they collide inelastically with other species and (2) the higher energy electrons can reach the source walls through the sheath potential and thus are lost via wall recombination.

The collisional energy loss per electron-ion pair created for electron collisions with neutrals H and H_2 is shown in Fig. 6.4. It is shown that the value of $E_{L,2}$ ranged from 130 down to 58 eV at electron temperatures of 5 to 10 eV. These values for hydrogen are about two to four times larger than those for argon discharge shown earlier in Fig. 5.3. This is because additional energy loss channels are included in a molecular gas discharge, such as

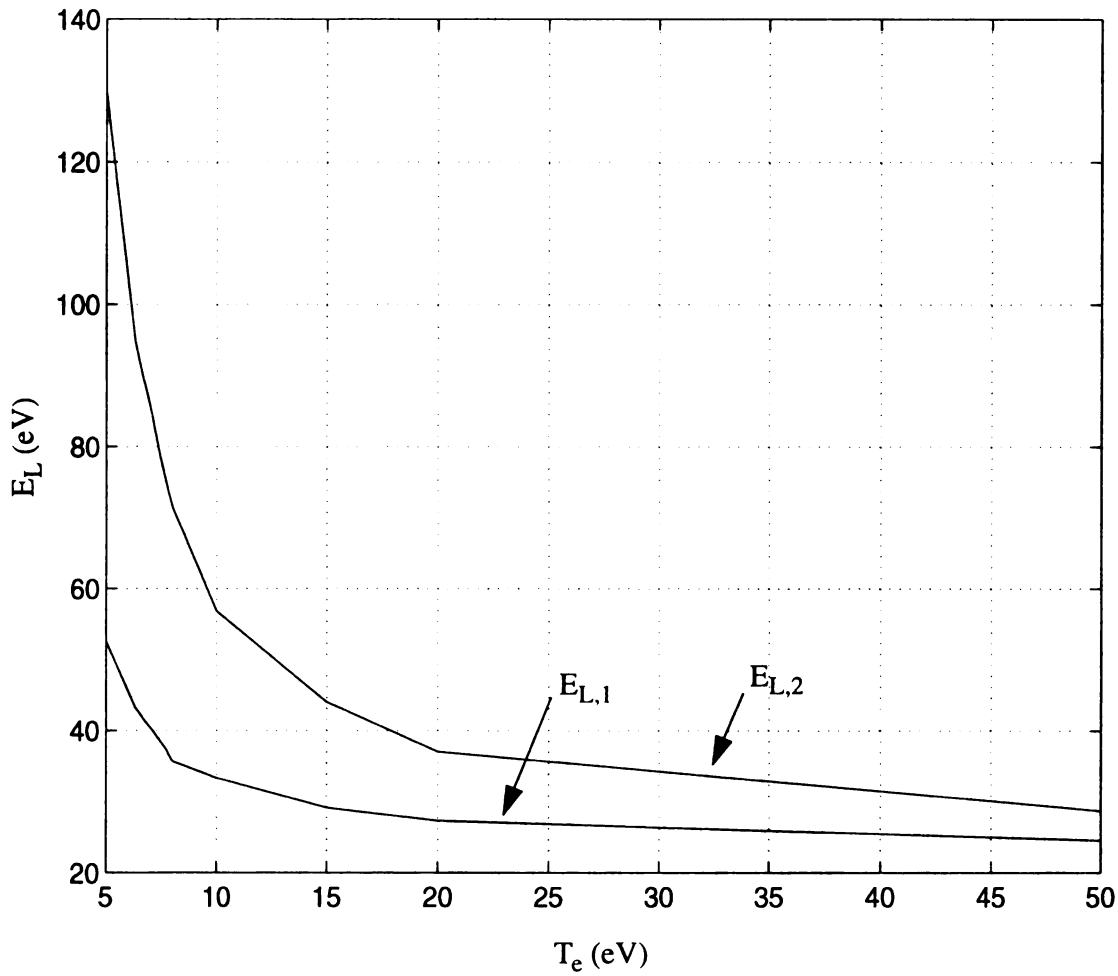

Figure 6.4 The collisional energy loss per electron-ion pair created in the hydrogen plasma. $E_{L,1}$ is the electron and atomic hydrogen collision energy loss, and $E_{L,2}$ is the electron and molecular hydrogen collision energy loss.

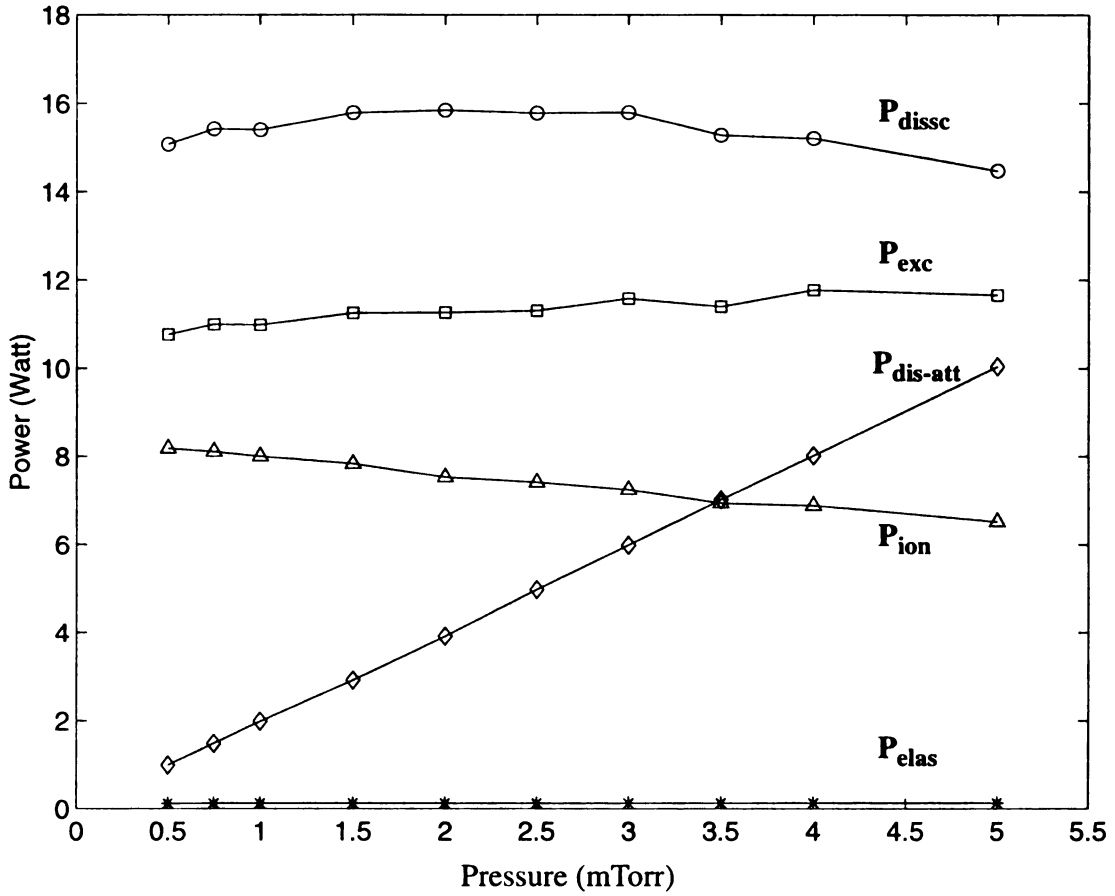

Figure 6.5 The power absorbed in the plasma volume by various collision processes including dissociation, excitation, ionization, dissociative attachments, and elastic collisions. The discharge conditions are 90 W of input power and 30 sccm of flow rate. The model used $f_{loss} = 0.38$, $c = 6.5$, and $\gamma = 0.005$.

dissociation, and excitation (vibrational, rotational, and electronic).

Fig. 6.5 shows the power absorbed in the plasma by different collision processes including dissociation, excitation, ionization, dissociative attachment (Reactions (8) in Table 5.1), and elastic collisions. A constant absorbed power of 60 W in the plasma over the pressure range is used in the hydrogen model. Note that the power absorbed by dissociation first slowly goes up, peaks at around 2.7 mTorr, and then slowly goes down, while the power absorbed by the dissociative attachment process goes up quickly within the investigated pressure range. The power absorbed by elastic collisions is found to be very small compared to all the other processes.

Fig. 6.6 shows the prediction of atomic hydrogen densities in the hydrogen plasma from the model using two different atomic hydrogen surface recombination coefficients: 0.005 and 0.05. The measured atomic hydrogen density from actinometry is also plotted. The atomic hydrogen densities were determined using the data shown earlier in Table 4.4 and Eqn. (3.29). The use of Eqn. (3.29) requires the calculation of the reaction rates, K's, which are each a function of the electron temperature. The electron temperatures utilized in the calculation at various pressures are those from the hydrogen discharge model plotted in Fig. 6.3. The predicted densities showed a good match with those of the experiment at $\gamma = 0.005$. Therefore this γ value is adopted in the model.

Fig. 6.7 shows the neutral and ionic particle densities in the hydrogen plasma. The dominant neutral species found in the hydrogen plasma source is H_2 and the dominant ionic species is H_2^+. Also noted in Fig. 6.7, the H_3^+ density increases quickly as the pressure increases. From the prediction of the model, at pressures of 5 mTorr and above, the H_3^+ density will become larger than those of H^+ and continue to increase as the

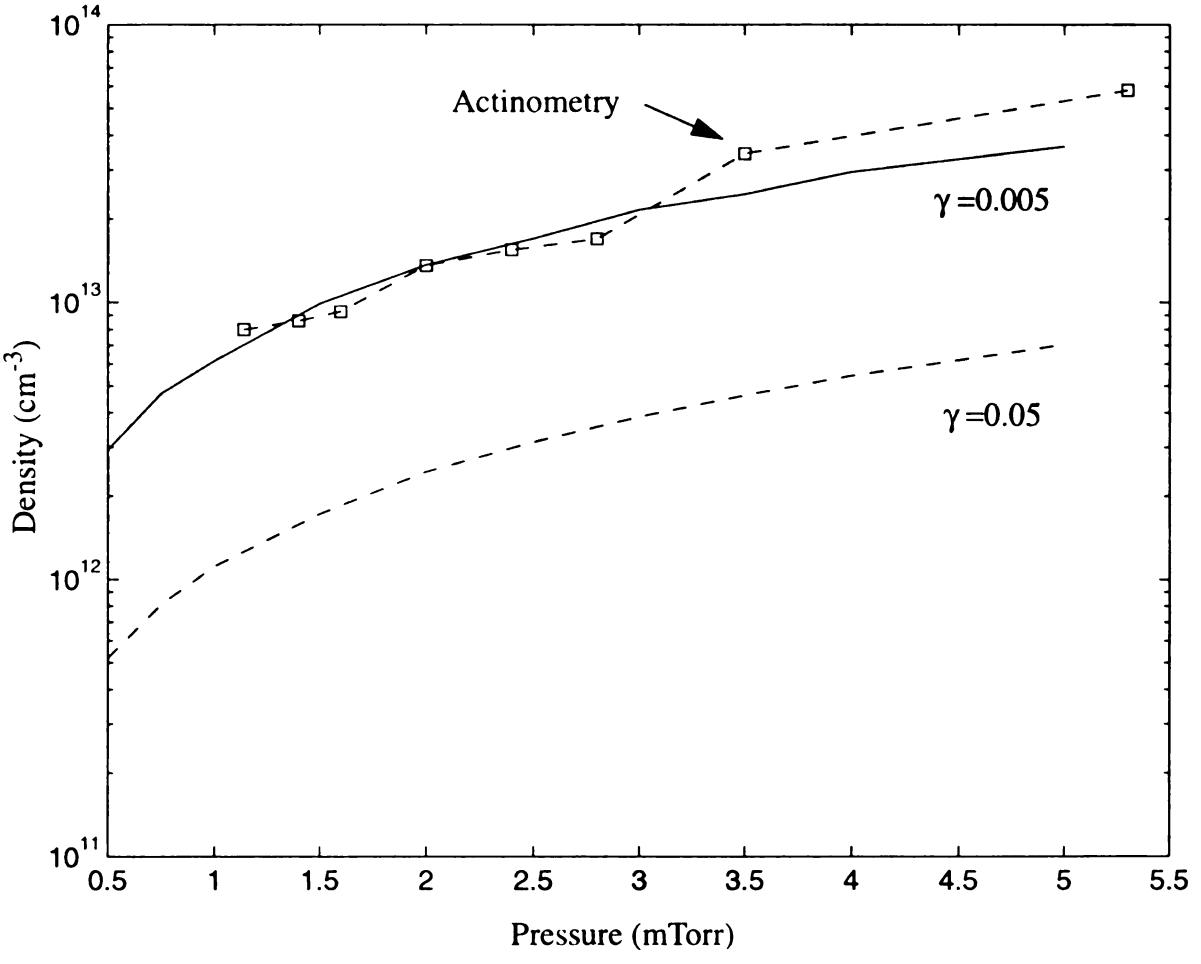

Figure 6.6 Determination of the atomic hydrogen surface recombination coefficient γ in the hydrogen plasma model from actinometry. The discharge conditions are 90 W of input power and 30 sccm of flow rate. The model used f_{loss} = 0.38, c = 6.5.

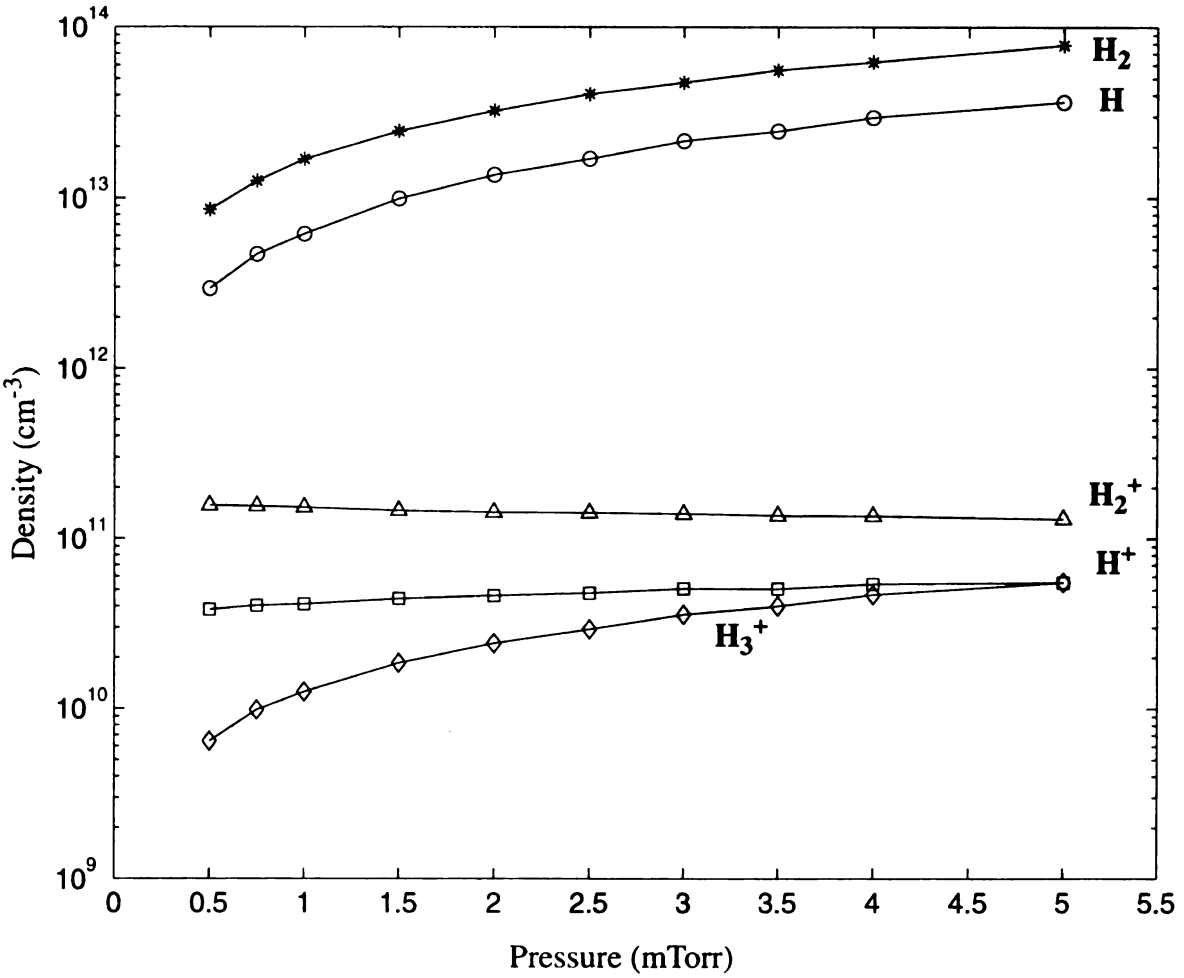

Figure 6.7 Neutral and ion densities in the H_2 plasma with input power of 90 W. The model used f_{loss} = 0.38, c = 6.5, and γ = 0.005.

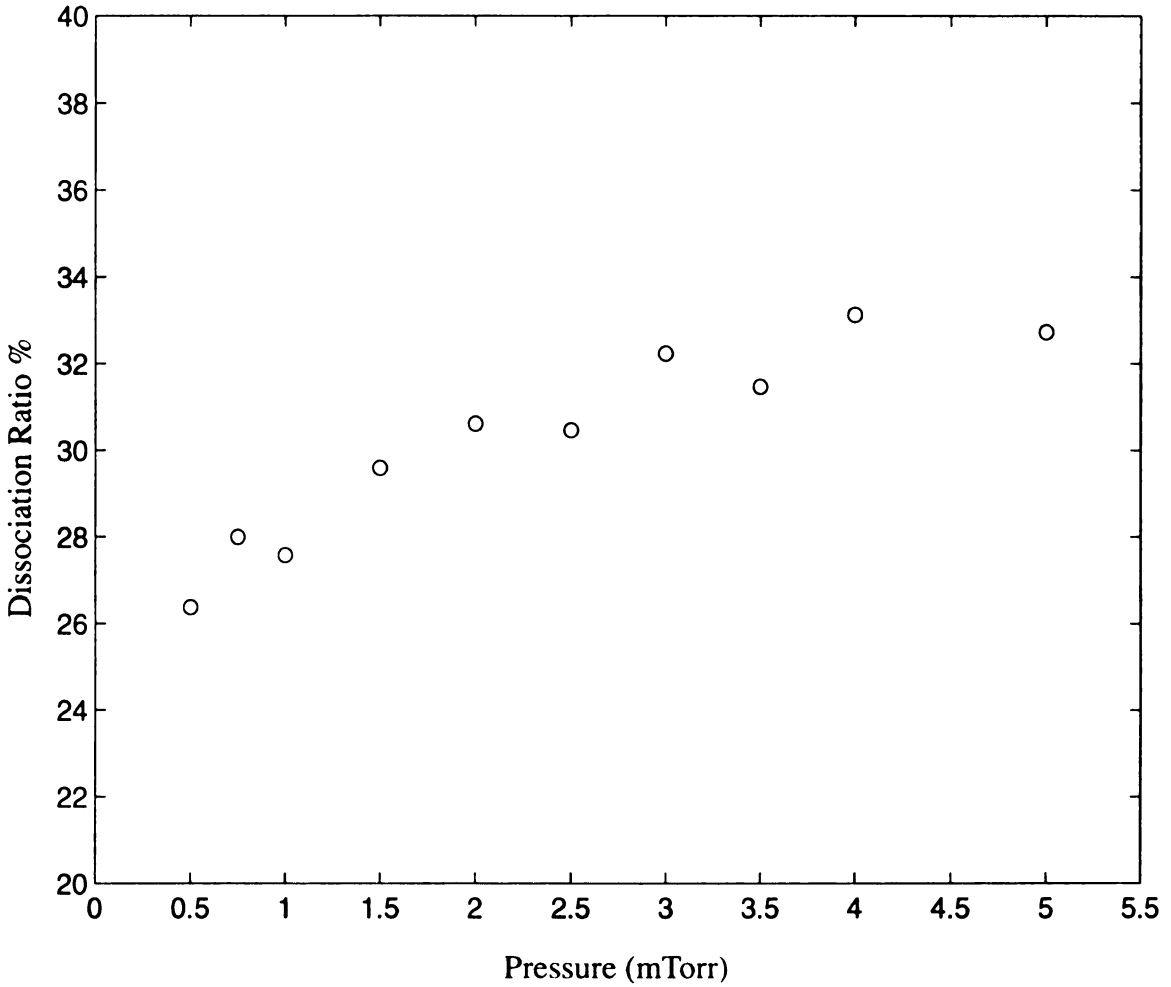

Figure 6.8 Atomic hydrogen dissociation percentage in the hydrogen plasma predicted by the model using P_{in} = 90 W, f_{loss} = 0.38, c = 6.5, and γ = 0.005.

pressure increases.

The dissociation percentage in the hydrogen plasmas is calculated using the atomic hydrogen density divided by the total gas density at various pressures and is shown in Fig. 6.8. The dissociation rate shows an overall increase with the pressure.

6.2.3 Argon-Hydrogen Mixture Model

The electron temperatures of the argon-hydrogen mixture discharges at different gas combinations are shown in Fig. 6.9. The discharge at two pressures were modeled: 0.6 and 4 mTorr. Both had input powers of 90 W. The electron temperature increases as it goes from a low hydrogen partial pressure ratio, $P(H_2)/P(Ar)$ to a high partial pressure ratio. For example, at 4 mTorr, the electron temperature is 4.0 eV at hydrogen partial pressure ratio of 0.2 and increases to 5.1 eV at pressure ratio of 5.0. This is expected since at a low $P(H_2)/P(Ar)$, the mixture contains mostly the argon gas and little hydrogen gas, the discharge hence will behave more close to an argon discharge with T_e = 3.7 eV at 4 mTorr as shown earlier in Fig. 6.1. As the hydrogen partial pressure ratio increases to 5.0, the Ar-H_2 mixture discharge contains mostly the hydrogen gas, therefore the discharge has a T_e more close to that of the hydrogen discharge (T_e = 6.5 eV) at the same pressure of 4 mTorr which is shown in Fig. 6.3. The experimental data at the same plasma conditions are also plotted for comparison. The measurements were taken with the probe positioned at 2 cm downstream from the end of the MPDR 610 body.

Fig. 6.10 shows the modeled neutral and charged particle densities in the mixture discharge at 0.6 mTorr. The dominant ion species is Ar^+ at a hydrogen partial pressure

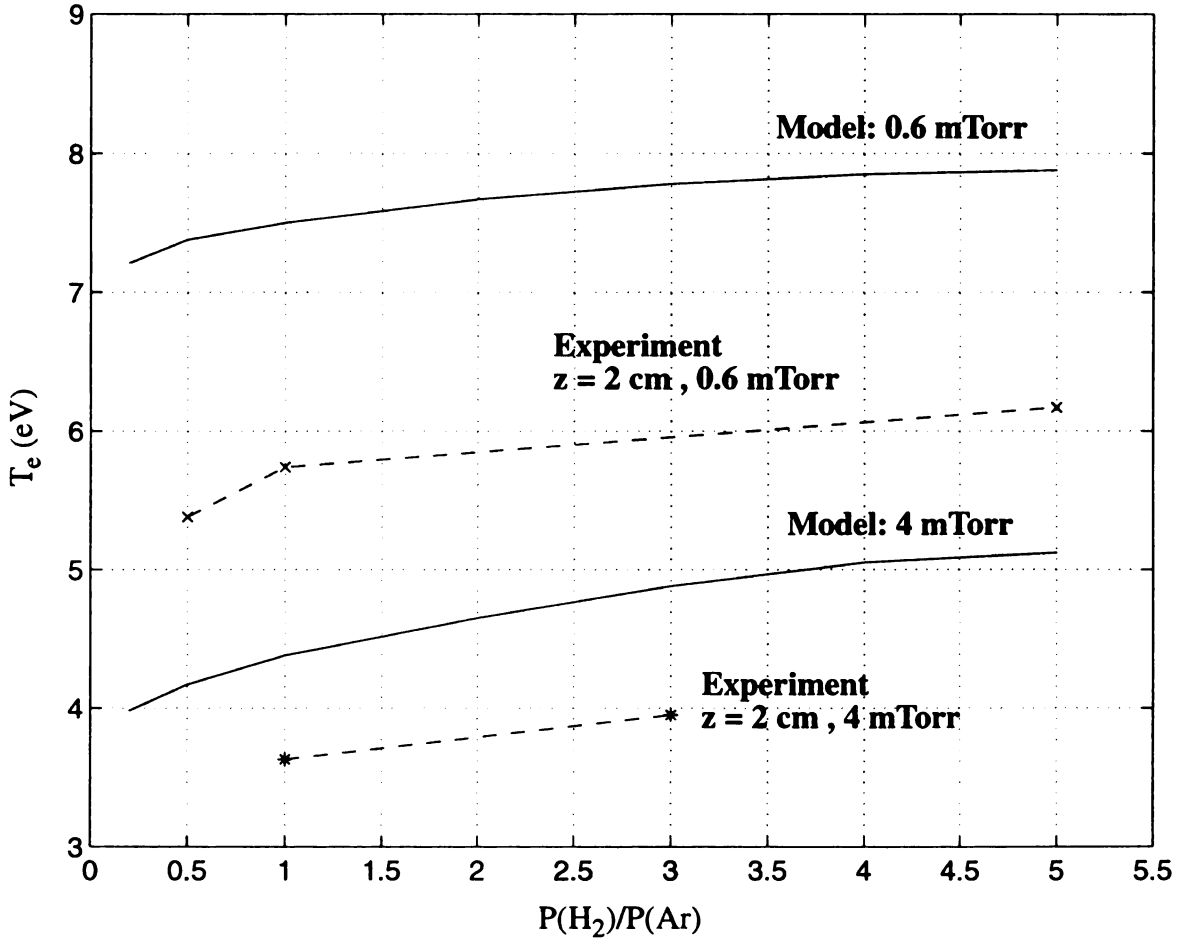

Figure 6.9 Electron temperatures in the Ar-H_2 mixture plasma.

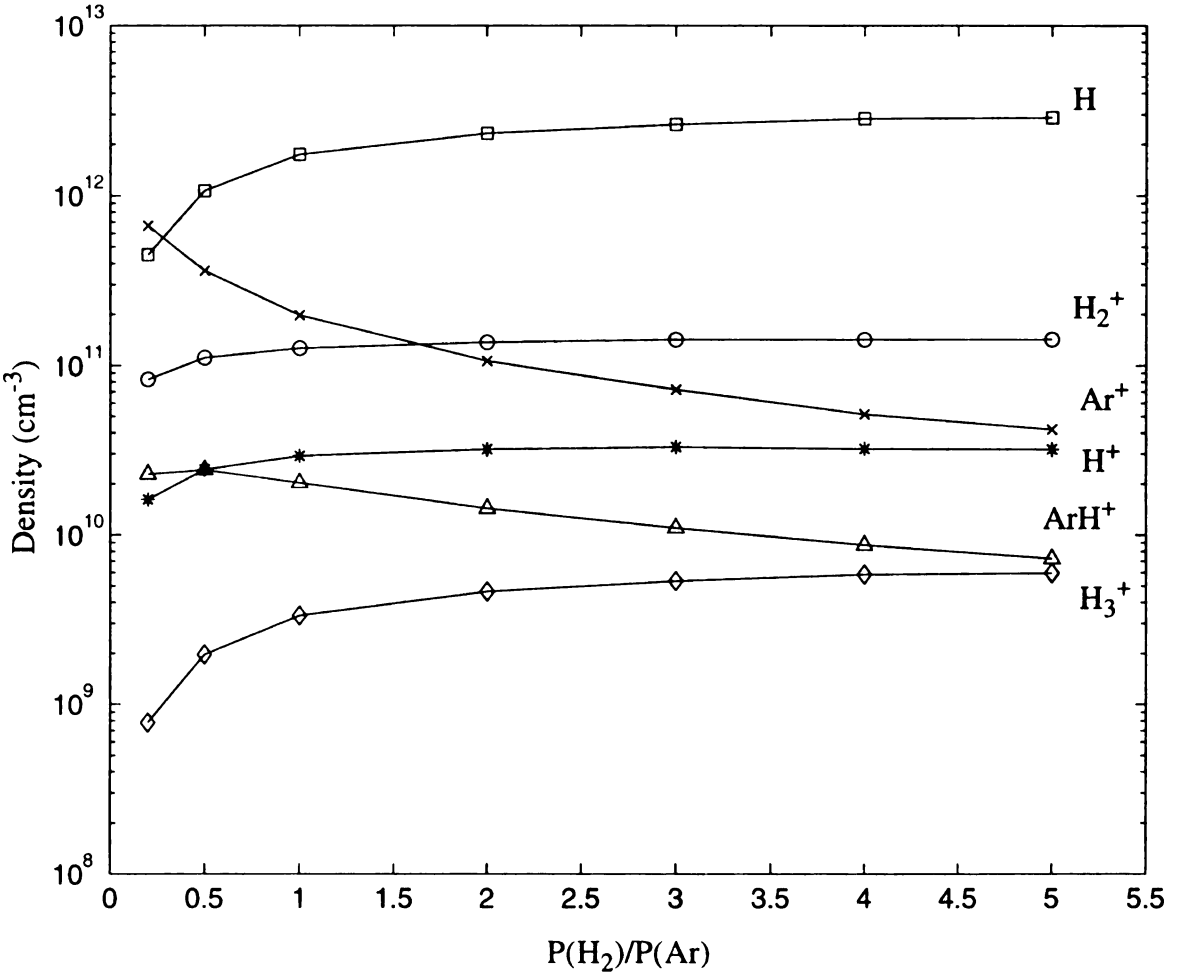

Figure 6.10 Neutral and ion densities in the Ar-H_2 plasma at 0.6 mTorr with input power of 90 W.

ratio smaller than 2.0. While at ratios greater than 2.0, the dominant ion species becomes H_2^+. The densities of H_3^+ are relatively low compared with that of H^+. This agrees with the hydrogen model prediction at the same pressure of 0.6 mTorr. At a higher pressure of 4 mTorr, the density of Ar^+ are dominant most of the time in the partial pressure ratio range of 0.2 to 4.0. This is shown in Fig. 6.11.

6.3 Modeling Results in the Downstream Region

The downstream charged particle density prediction using the diffusion model was described earlier in Section 5.3.4. The model used the plasma density in the source found from the plasma source modeling as the input boundary condition and then solved the ambipolar diffusion model to calculate the charged particle density in the downstream region (z= 0 - 30 cm, r= 0 - 15 cm). In the source region, two models were used in the calculation of electron densities in the argon discharges. The results are shown earlier in Fig. 6.2. Using these values as the boundary values for the diffusion model, the electron densities of the argon plasmas in the downstream region are computed for various pressures.

Fig. 6.12 shows the simulated electron density in the argon plasma with a 90 W input power at 2 cm downstream. The density measurements from double Langmuir probe as shown in Fig. 4.6 are also plotted for comparison. The model using $f_{loss} = 0.4$ and $c = 0$ predicts a density curve that is more close to the experimental variation over pressures, while the model using $f_{loss} = 0.4$ and $c = 0.17$ predicts a more uniform density over the investigated pressure range.

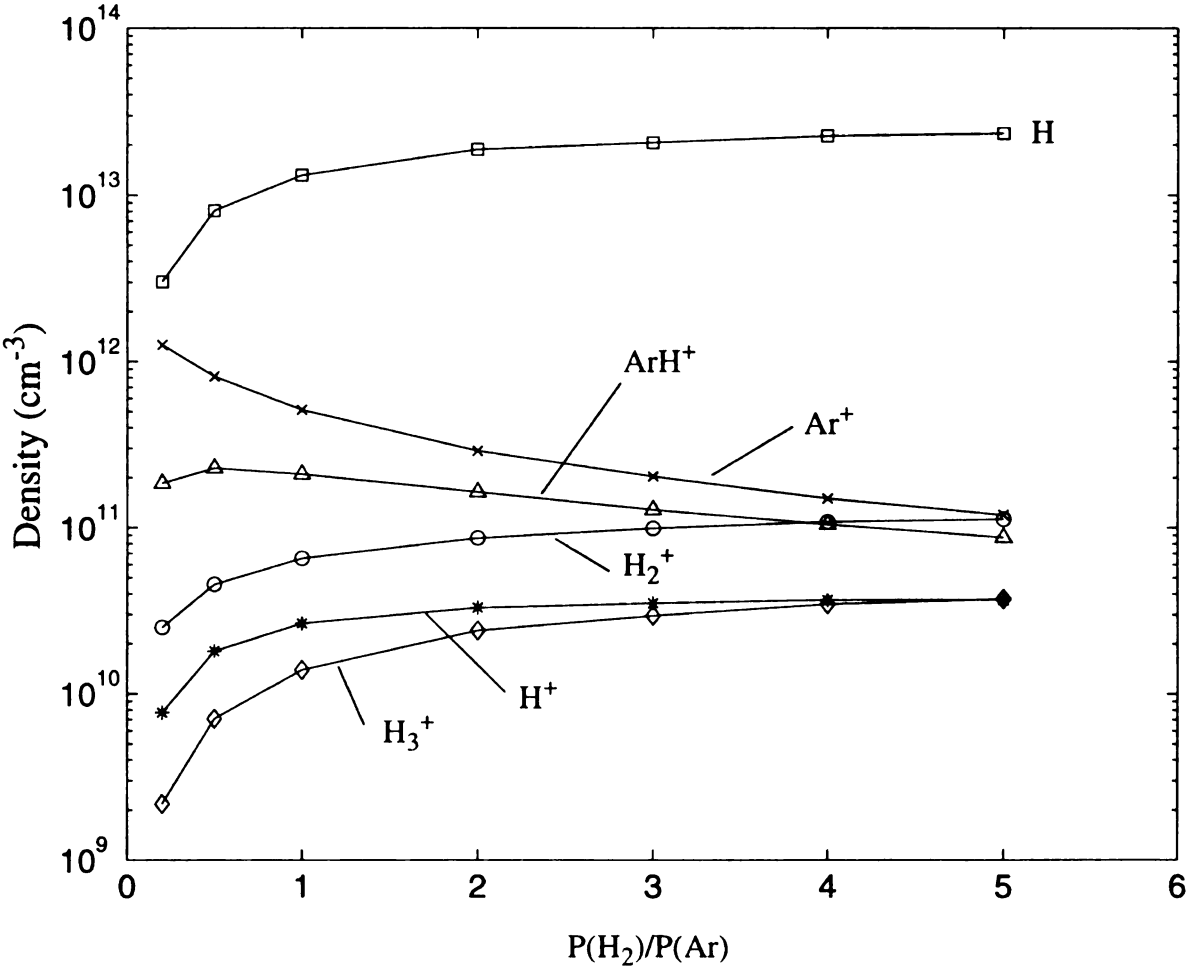

Figure 6.11 Neutral and ion densities in the Ar-H_2 mixture plasma at 4 mTorr with input power of 90 W.

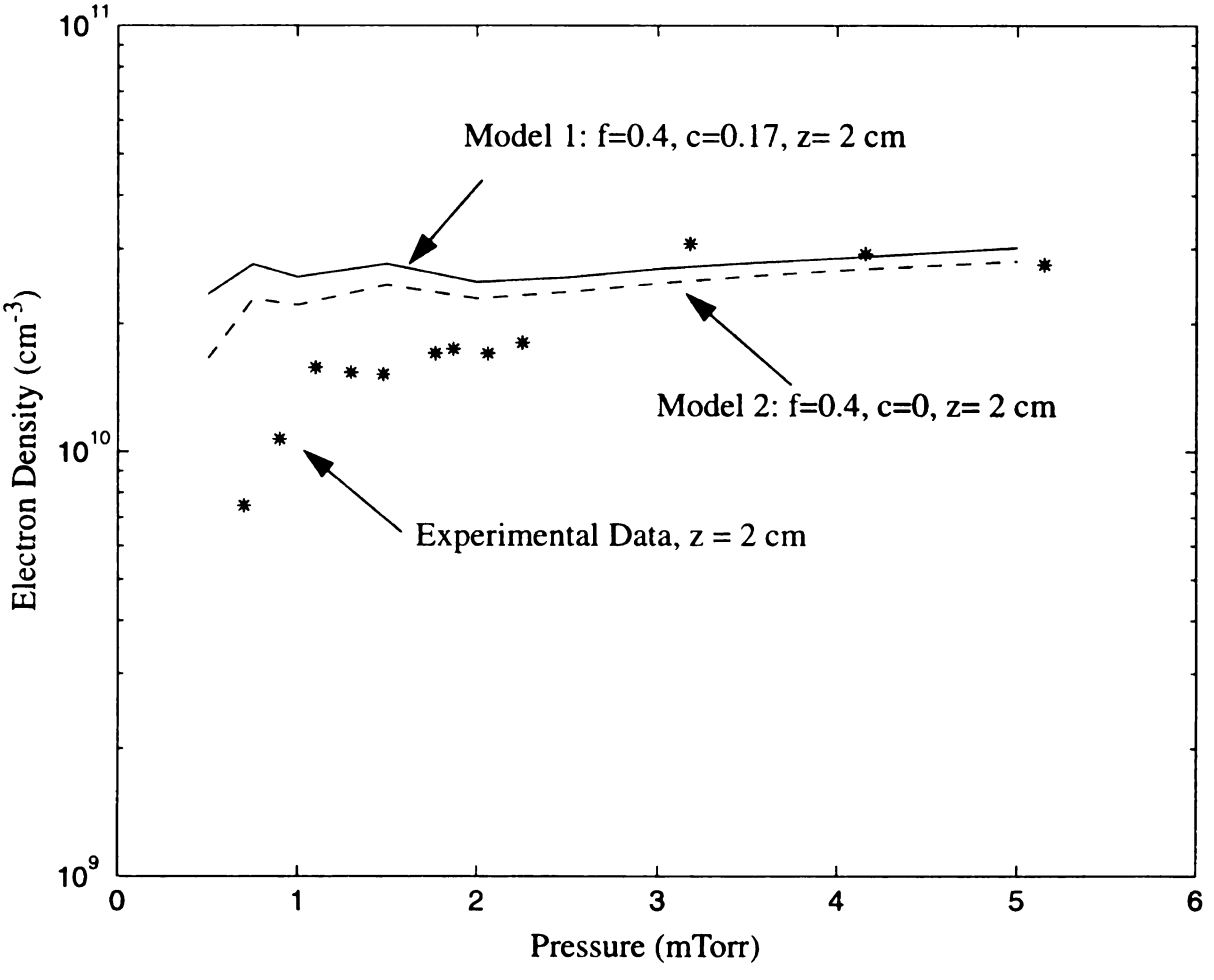

Figure 6.12 Ar plasma electron density at downstream z = 2 cm. The dashed line is the model 2 prediction and the solid line is model 1 prediction. The (*) points are from experimental measurements. The input power is 90 W and flow rate is 8 sccm.

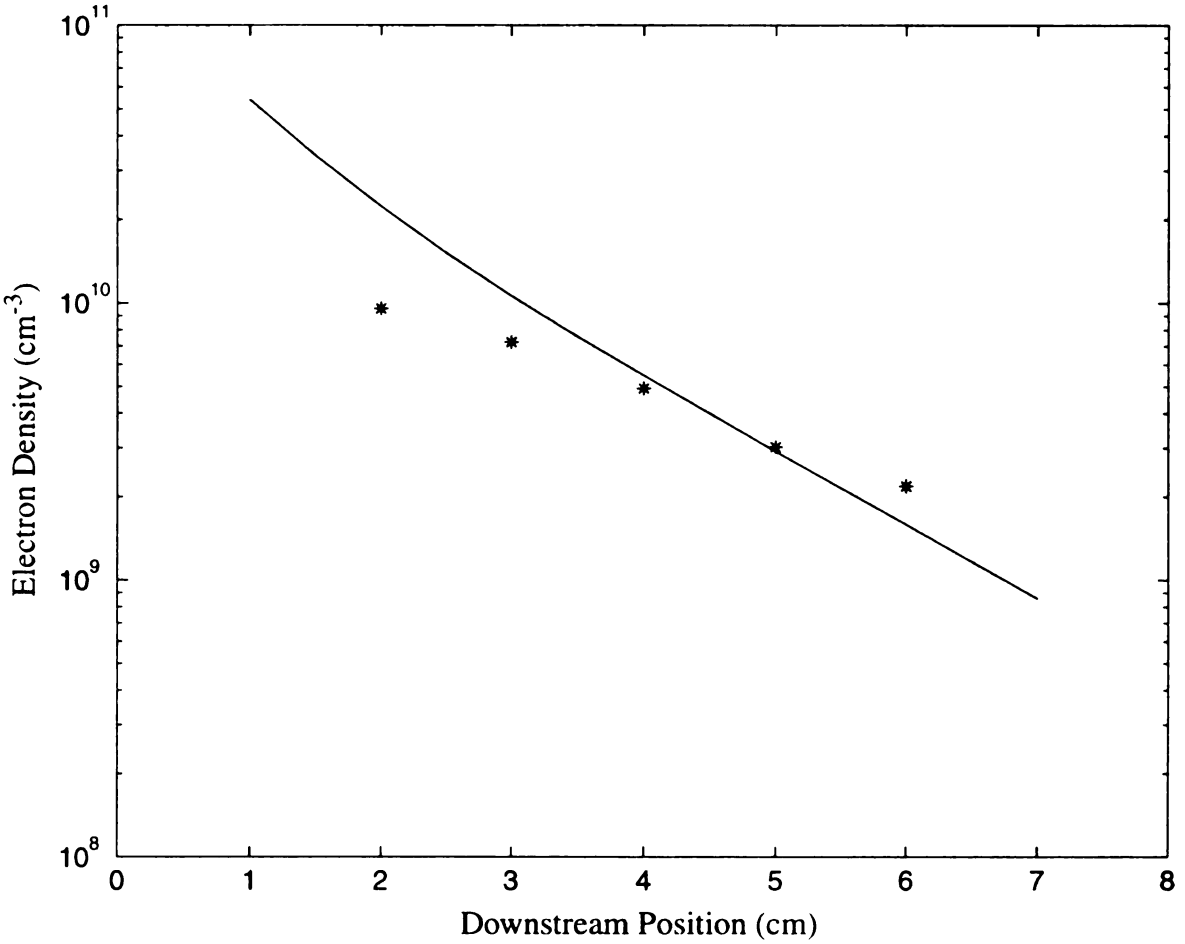

Figure 6.13 Comparison of argon plasma diffusion model with experimental data taken in the downstream region. Plasma conditions: P_{in} = 90 W, 1 mTorr, ans 8 sccm.

Fig. 6.13 compares the experimental results of electron densities at 2 cm downstream from Langmuir probe measurements with the results from the hydrogen discharge model using $f_{loss} = 0.38$ and $c = 6.5$. The input power is also 90 W, the same as in Fig. 6.12. It is found that at pressures higher than 2 mTorr, the model has a better fit with the experimental data in magnitude, while at pressures less than 2 mTorr, the difference between the measured and modeled results becomes larger.

The electron densities in the argon and hydrogen plasmas at various downstream positions are plotted in Fig. 6.14 and Fig. 6.15, respectively. The input conditions for both figures are 90 W input power and 1 mTorr pressure. It is shown that the model prediction of the electron density in both of the discharges has a faster decreasing rate along the downstream distance than those from the experimental measurements. This may be explained as follows. In the downstream diffusion model, it assumes no ionization process in the downstream region, hence the ionization frequency equals to zero. This may not be true. The ionization processes are expected to continue in the downstream region until at some distance the electron energy is too low to cause any ionization.

6.4 Conclusions

Global plasma source models have been developed for argon, hydrogen, and argon-hydrogen discharges, The models incorporate the effects of both static magnetic field confinement of charged particles and additional ionization produced by trapped electrons in the magnetic fields. Comparison of the experimental measurements for the argon, hydrogen, and argon-hydrogen discharges to the models indicates the importance of

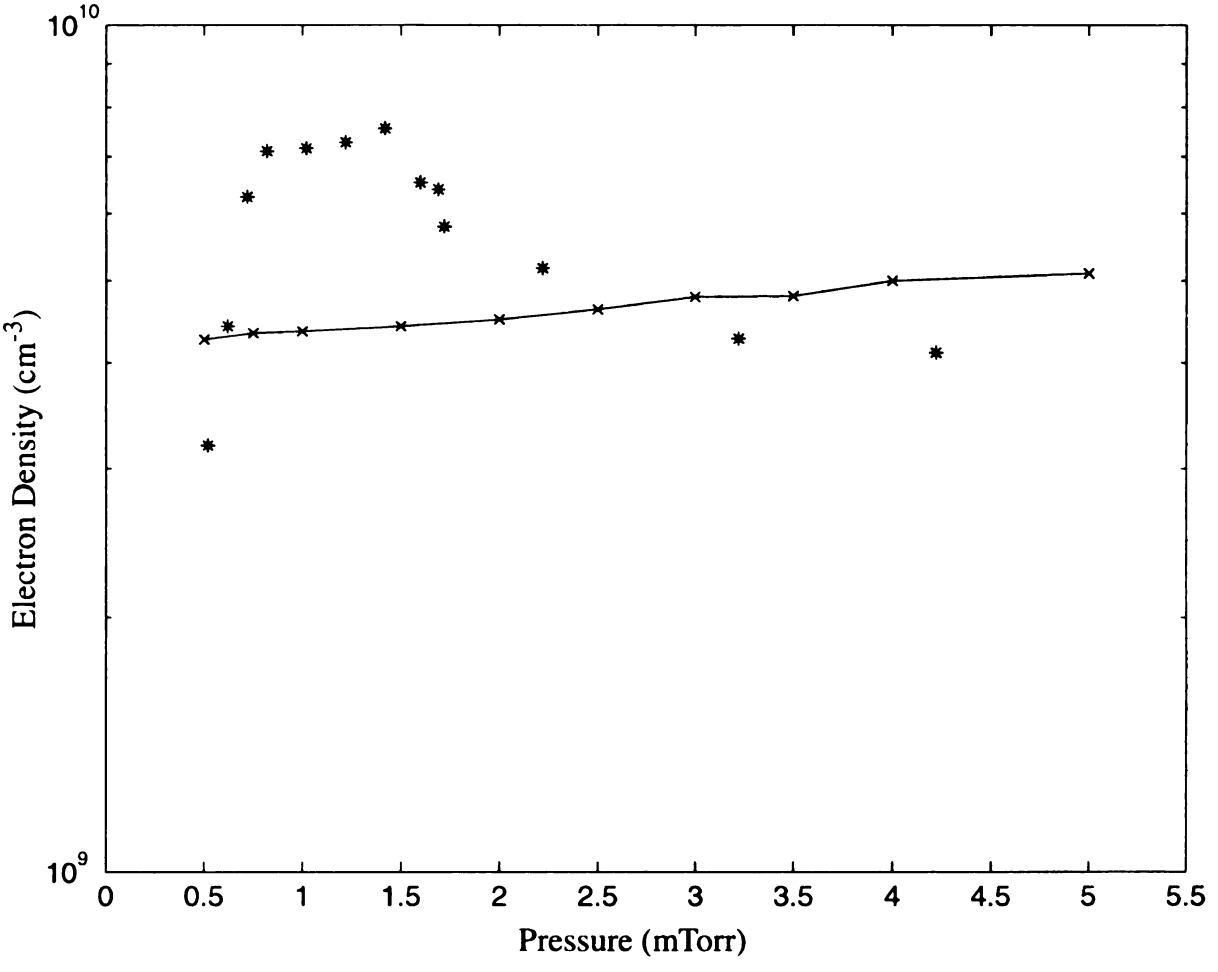

Figure 6.14 Comparison of hydrogen discharge model with experimental data at z = 2 cm. The input power is 90 W. Flow rate= 30 sccm.

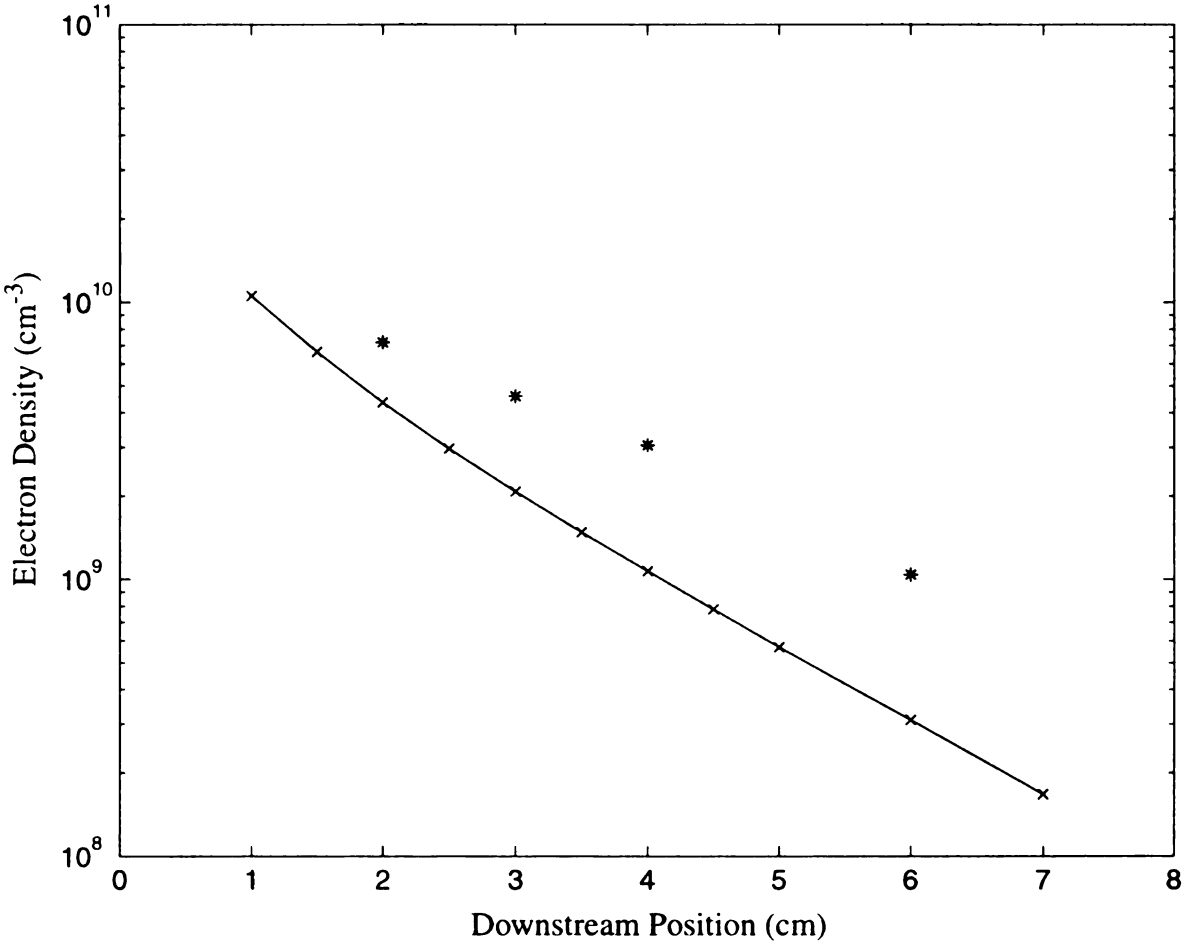

Figure 6.15 Comparison of hydrogen plasma diffusion model with experimental data taken in the downstream region. Plasma conditions: P_{in} = 90 W, 1 mTorr, and 30 sccm.

considering both of these magnetic field influences in the plasma source for predicting the electron temperature. Overall the electron temperature in the discharges can be reasonably predicted by comparing with the experimental results The determination of the charged species densities showed general agreement at downstream z = 2 cm with a factor of 2 or less difference between the measurements and models.

CHAPTER 7

Summary and Recommendations for Future Research

7.1 Summary of the Results

The study of the neutral and charged species properties in the electron cyclotron resonance microwave plasma disk reactor (MPDR) presented in this work provides a more complete understanding of the low pressure, high density plasma behavior in both atomic and molecular gas discharges. Knowledge of the macroscopic plasma properties such as ion densities, electron energy distribution function, and neutral density allows better control and integration of plasma processing, as well as, improvement in discharge operation (uniformity, deposition/etch rate, substrate damage, ...). A spatially-averaged discharge model is developed based on the chosen experimental results for better understanding and predicting of the discharge characteristics in atomic, molecular, and mixture gas discharges.

7.1.1 Ion Density Measurements

The ion density in the MPDR 610 discharge is measured with a double Langmuir

probe in the downstream region at 2 - 10 cm from the source. The ion density at z = 2 cm in the argon discharges generally increases with the pressure (0.5-5 mTorr) except at pressures of around 1.2 mTorr where the microwave reflected power jumps from 10 W to 24 W. With a decreased absorbed power versus pressure, the ion density has little change in this range of pressures. The peak ion density of 3.08×10^{10} cm^{-3} occurs at pressures around 3 mTorr with a microwave input power of 90 W and a flow of 8 sccm (see Fig.4.6).

The ion density in the hydrogen discharges at z = 2 cm has a peak of 7.5×10^{9} cm^{-3} at a pressure around 1.5 mTorr, 90 W input power, and flow of 30 sccm (Fig. 4.7). The microwave reflected power, unlike the case in argon discharges, is stable and very small (less than 5 W) in the hydrogen plasma. The ion density along the downstream direction is also measured for both argon and hydrogen discharges (Fig. 4.8). It is found to decrease less quickly versus downstream distance that predicted by a pure ambipolar diffusion model.

7.1.2 Electron Energy in the Discharge

The electron energy and its distribution function in the MPDR created discharges are investigated via single Langmuir probe. The probe is usually positioned at 2 cm downstream away from the discharge generated region. The measured electron energy in the argon discharge at an input power of 90 W varies from 5.0 to 3.2 eV for the pressure range of 0.5 - 4.7 mTorr. The electron energy in hydrogen plasma at the same input power varies from 5.8 to 4.9 eV for the pressure range of 0.5 - 3 mTorr. The electron energy distribution functions for both argon and hydrogen discharges show a Maxwellian like

distribution at energies less than 10 eV and have some deviations from the Maxwellian at the tail of the distributions. The downstream electron energies are also recorded at positions z = 2 to 10 cm for both of the discharges and are used to estimate the electron temperature in the source by extrapolating the temperature data taken at various downstream positions. For the argon plasma at 1 mTorr, 90 W input power, and 8 sccm flow rate, the predicted electron temperature in the source is about 5.8 eV and is 7.8 eV for the hydrogen discharge at the same input conditions at flow rate of 30 sccm. The electron temperature in the argon-hydrogen mixture discharge is measured at three pressures including 0.6, 1.0, and 4 mTorr. The mixture gas composition is varied at each pressure. The electron temperature at 1 mTorr and 90 W input power varies from 4.8 to 5.7 eV for hydrogen partial pressure ratio of 1 to 4.

7.1.3 Optical Emission Spectroscopy (OES)

Optical emission from three noble gases including Ar, Kr, and Xe added in the hydrogen discharge are observed and recorded to obtain the electron temperature in the discharge source region. The observed emission lines have threshold energies from 9.82 to 13.5 eV. The results are discussed for the case of with and without xenon emission included. The electron temperature in the hydrogen discharge determined from OES at 3 mTorr and 90 W input power is 6.5 eV. Argon emission from its doubly ionized atoms are observed at 328.59 nm and 331.13 nm (Fig. 4.12) which suggests the existence of an non ignorable number of high energy electrons in the argon discharge. Actinometry is performed to obtain the information on the atomic hydrogen concentration in the hydrogen discharge. The actinometry data is further analyzed in Chapter 6 using the

electron temperature in the source so that the density of atomic hydrogen is obtained.

7.1.4 Modeling of the Compact ECR Plasma Source

A spatially-averaged (global) model is developed for low pressure discharge conditions. The model uses charged particle conservation by equating the generation of the ions in the plasma volume to the diffusion loss on the wall, and it uses power balance of electrons which absorb energy from the input microwave power and lose energy due to collisions with the neutral (e.g. Ar, H_2, and H). The collision processes can be elastic or inelastic, such as ionization, excitation, dissociation. Radial diffusion of the charged species in the plasma is restricted due to the arrangement of permanent magnets around the discharge chamber in MPDR 610. Electron temperature, neutral and charged species densities are solved in argon, hydrogen, and argon-hydrogen mixture discharges. Determination of atomic hydrogen surface recombination coefficient is done by comparing the modeled hydrogen atom concentrations of different recombination coefficients with the experimental results of actinometry (see Fig.6.6). The model provides a good prediction of the electron temperature in all three discharges when compared with the experimental results. For the argon discharge, the model also have a good agreement of the ion densities with the experiments within reasonable error. However, the density profile from the model of the hydrogen discharge does not predict a peak at a certain range of pressure as the experiment indicates.

7.2 Recommendations for Future Research

In addition to the plasma properties (electron temperature, neutral and ion densities) investigated in this thesis, there are still some properties left experimentally unknown, such as the neutral temperature and ion energy in the discharge, which can play a critical role in surface processing. Positive ion bombardment on the substrate is important in achieving anisotropic etching with high aspect ratio necessary for microelectronic manufacturing in deep submicron features. Electrostatic energy [108] or optical Doppler shift measurement using optical emission spectroscopy (OES) [109] or Laser-induced fluorescence (LIF) [110],[111] technique is suggested for the study of ion energies or gas temperature in the discharge. In a molecular gas or gas mixture discharge, it is also useful to use a mass spectrometer to measure the relative number of various ions with different charge or mass. While it is not possible to distinguish the individual density of each charged species when utilizing a Langmuir probe to measure the charged particle density in the plasma.

In the modeling of the discharge with magnetic confinement applied on the discharge chamber, the model developed in this work provides a good overall agreement with the experiment within the pressure range investigated. The ion density profile in the hydrogen model, however, does not show a similarity at a certain pressure range as the experiment result. A more complex model of the magnetic confinement of the charged particle should be studied for improvement.

The developed model has successfully predict the electron temperature, neutral and ion densities in the discharge (atomic, molecular, and mixture gas discharges). Future extended work should go to the modeling of other molecular or mixture discharges (Cl_2,

Ar/CH_4, H_2/CH_4, ...) which is frequently used in the deposition and etching processes.

APPENDICES

Appendix A

Argon Plasma Global Model Program

```
%************************************************************ %
% Argon plasma modeling with consideration of plasma confinement, f_loss  %
% and additional ionization from trapped electrons.                       %
% This program calculates the electron denity at various absorbed powers  %
% and pressures by first generating Te vs ng*d plots with and without a    %
% f_loss term and using it to determine Te.                               %
%************************************************************ %

Kiz0=6e-14;       %m3/s
Eiz=15.76;        %eV
e=1.6e-19;
mi=40*1.67e-27;  %kg

i=0;

for Te=1:0.1:20;
  i=i+1;
  Kiz=Kiz0*exp(-Eiz/Te);
  ub=sqrt(e*Te/mi);
  left=Kiz/ub;
  x(i)=0.4/left;
  y(i)=1/left;
end

Te=1:0.1:20;
semilogx(x,Te,y,Te,'--'),grid
xlabel('n_gd_eff (m-2)')
ylabel('Te (eV)')
title('Ar plasma with f_l=1, 0.4  /model/argon/te-nd.eps')
axis([1e17 1e21 1 20])
```

```
R=1.8; L=3;      %cm, cylindrical discharge dimension
k=1.38e-23;
Pin=.1;                              %mW, input power
Pr=[1 1 2.4 2.6 3.8 4  4 4 4 4];     %0.1W, reflected power
p=[0.5 0.75 1 1.5 2 2.5 3 3.5 4 5]; %mTorr
f_loss=.4;       %fraction of diffusion loss to the wall

clear T
clear nd

for j=1:10

Tar=420;                             %Kelvin, argon gas temperature
ng=p(j)*1e-3*133.32/(k*Tar)  %m-3, neutral gas density at a specified pressure

lampda=1/(ng*1e-6)/1e-14     %cm, ion collision cross section=1e-14 cm2
if lampda>L
 hl=.4;
 hr=.4;
else
 hl=.86/sqrt(3+L/2/lampda);
 hr=.8/sqrt(4+R/lampda);
end

Aeff=f_loss*2*pi*R*(R*hl+L*hr)*1e-4;                    %m2
deff=R*L/(f_loss/(1+.17/p(j))*2*(R*hl+L*hr))*1e-2;   %m
nd(j)=ng*deff                                                    %m-2

%-------------- Determine Te in the plasma ----------------------%
for i=1:191
 if (nd(j)<y(i)) & (nd(j)>y(i+1))
  T(j)=1+0.1*i
  break
 end
end

ub=sqrt(e*T(j)/mi);   %m/s

%Determine electron collisional energy loss, Ec

if T(j)>=1 & T(j)<=2
 Ec(j)=800-(800-88)*(T(j)-1)
elseif T(j)<=3
 Ec(j)=88-(88-50)*(T(j)-2)
elseif T(j)<=4
 Ec(j)=50-(50-38)*(T(j)-3)
```

```
elseif T(j)<=5
  Ec(j)=38-(38-31)*(T(j)-4)
elseif T(j)<=6
  Ec(j)=31-(31-28)*(T(j)-5)
elseif T(j)<=7
  Ec(j)=28-(28-25)*(T(j)-6)
elseif T(j)<=8
  Ec(j)=25-(25-23)*(T(j)-7)
elseif T(j)<=9
  Ec(j)=23-(23-22)*(T(j)-8)
elseif T(j)<=10
  Ec(j)=22-(22-21)*(T(j)-9)
elseif T(j)<=20
  Ec(j)=21-(21-20)*(T(j)-10)
elseif T(j)>20
  Ec(j)=20
end

% Total energy loss per electron-ion pair created, eV
Et=Ec(j)+7.2*T(j);

% The absorbed power by plasma, Watt
Pabs=Pin*909-Pr(j)*9.015;

% Calculated electron density, m-3
ne(j)=Pabs/(e*ub*Aeff*Et);

end
ne
```

Appendix B

Hydrogen Discharge Global Model Program

```
%========================================================%
% This program calculates the neutral, electron, and ion densities of    %
% hydrogen discharges at low pressures (0.5-4 mTorr). The neutral and     %
% ionic species considered include H2, H, H+, H2+, and H3+. The reactions %
% included are mostly electron-neutral collisions.                        %
%========================================================%

%Constant values

k=1.38e-23;
e=1.6e-19;
a_h=.53e-10;      %meter
m_h=1.67e-27;     %kg

%----------------- Plasma source condition ----------------------%

R=1.8; L=3;           %cm, cylindrical discharge dimension
Th=420; Th2=420;      %Kelvin; temperature of neutrals
p=5;                  %mTorr, chamber pressure
Th=Th2;
Ng=p*1e-3*133.32/(k*Th2);
N_h2=Ng               %m^-3
Ne=3.0e17;            %m^-3
gamma=0.005;          %hydrogen surface recombination coefficient

fl_h=0.38;            %fraction of diffusion loss to the wall

lampda_1=1/(N_h2)/1e-19;    %m, H+ collision cross section=1e-19 m2
lampda_2=1/(N_h2)/1e-18;    %m, H2+ collision cross section=1e-18 m2

if lampda_1 >L*1e-2
```

```
 hl=0.4; hr=0.4;
else
 hl=.86/sqrt(3+L*1e-2/2/lampda_1);
 hr=.8/sqrt(4+R*1e-2/lampda_1);
end

A1=fl_h*2*pi*R*(R*hl+L*hr)*1e-4;     %m2

if lampda_2 >L*1e-2
 hl=0.4; hr=0.4;
else
 hl=.86/sqrt(3+L*1e-2/2/lampda_2);
 hr=.8/sqrt(4+R*1e-2/lampda_2);
end

A2=fl_h*2*pi*R*(R*hl+L*hr)*1e-4;     %m2

lampda_5=1/(N_h2*1e-6)/1e-15;  %cm, H3+ collision cross section=1e-15 cm2

if lampda_5 >L
 hl=0.4; hr=0.4;
else
 hl=.86/sqrt(3+L*1e-2/2/lampda_5);
 hr=.8/sqrt(4+R*1e-2/lampda_5);
end

A5=fl_h*2*pi*R*(R*hl+L*hr)*1e-4;     %m2

Te=input('Input the electron temperature (eV), Te =');


V=pi*R^2*L*1e-6;              %m^3
v_avg=sqrt(8*k*Th/pi/m_h);    %m/s
z=(pi/L)^2+(2.405/R)^2;       %cm^-2

% Calculate ionization rate constants Kiz_11, Kiz_2, Kiz_12;

b1=[-3.27140e1 1.35366e1 -5.73933 1.56315 -2.87706e-1 3.48256e-2 -2.63198e-
3 1.11954e-4 -2.03915e-6];

b2=[-3.56864e1 1.733469e1 -7.76747 2.21158 -4.16984e-1 5.08829e-2 -
3.83274e-3 1.61286e-4 -2.89339e-6];

b3=[-3.83460e1 1.42632e1 -5.82647 1.72794 -3.59812e-1 4.82220e-2 -3.9094e-3
1.73878e-4 -3.25284e-6];
```

```
ln_Kiz2=0;
ln_Kiz11=0;
ln_Kiz12=0;

for i=1:9

 ln_Kiz11=ln_Kiz11+b1(i)*log(Te)^(i-1);
 ln_Kiz2=ln_Kiz2+b2(i)*log(Te)^(i-1);
 ln_Kiz12=ln_Kiz12+b3(i)*log(Te)^(i-1);

end

Kiz_11=exp(ln_Kiz11)*1e-6;    %m^3/s
Kiz_2=exp(ln_Kiz2)*1e-6;      %m^3/s
Kiz_12=exp(ln_Kiz12)*1e-6;    %m^3/s

% Determine hydrogen dissociation rate constant
if Te<7 & Te>=3

 m=log10(12/2.2)/log10(7/3);
 lg_Kh=m*(log10(Te)-log10(3))+log10(2.2e-15);
 Kh2_h=10^(lg_Kh);             %m^3/s

elseif Te<=14

 m=log10(2.1/1.2)/log10(14/7);
 lg_Kh=m*(log10(Te)-log10(7))+log10(1.2e-14);
 Kh2_h=10^(lg_Kh);

else

 Kh2_h=2.2e-14;                %m^3/s

end

% Rate constant for creation of H3+
Kex_25=2.11e-15;               %m^3/s

% Ionization threshold energies, eV
Eiz_11=13.6; Eiz_2=15.4; Eiz_12=18;

ub1=sqrt(1.6e-19*Te/m_h);     %m/s
ub2=sqrt(1.6e-19*Te/2/m_h);   %m/s
ub5=sqrt(1.6e-19*Te/3/m_h);   %m/s

% ---------- Solving for densities of H+,H2+,H3+ ----------%
```

```
err1=10;
c=6.5;

while err1 > 5

A(1,:)=[V*gamma*k*Th*z*1e4/m_h/(2e-19*v_avg)/N_h2+V*Kiz_11*Ne*(1+c/
p) 0 -V*Kex_25*N_h2 0];
A(2,:)=[-V*Ne*Kiz_11*(1+c/p) A1*ub1 0 0];
A(3,:)=[0 0 V*N_h2*Kex_25+A2*ub2 0];
A(4,:)=[0 0 -V*N_h2*Kex_25 A5*ub5];
b=[V*Kh2_h*N_h2*Ne; V*Ne*N_h2*Kiz_12; V*N_h2*Ne*Kiz_2; 0]*(1+c/p);
X=A\b;

N_h=X(1);
N_1=X(2); N_2=X(3); N_3=X(4);
new=Ng-N_h;
err1=abs(new-N_h2)/N_h2*100;
N_h2=new;

end

%Checking for reasonable Te assumption

c=sum(X)-X(1);
err=abs(Ne-c)/Ne*100


%------------------- Computing the power absorbed by plasma----------------------%

b1=[-2.81495e1 1.00983e1 -4.77196 1.46781 -2.97980e-1 3.86163e-2 -3.05169e-
3 1.33547e-4 -2.47609e-6];

b2=[-2.83326e1 9.58736 -4.83358 1.41586 -2.53789e-1 2.80071e-2 -1.87141e-3
6.98667e-5 -1.12376e-6];

b3=[-3.0819e1 1.03887e1 -4.25977 1.18123 -2.27751e-1 2.90058e-2 -2.28759e-3
1.00435e-4 -1.86993e-6];

b4=[-3.3482e1 1.3717e1 -5.92261 1.70972 -3.50523e-1 4.83438e-2 -4.13141e-3
1.94839e-4 -3.85428e-6];

b5=[-3.64659e1 1.43036e1 -6.07443 1.67731 -3.12871e-1 3.80542e-2 -2.86001e-
3 1.19964e-4 -2.14223e-6];

b6=[-2.85801e1 1.03854e1 -5.38383 1.95064 -5.39367e-1 1.00692e-1 -1.16076e-
```

```
2 7.41162e-4 -2.00137e-5];

ln_Kexc11=0; ln_Kexc12=0;
ln_Kexc21=0; ln_Kexc22=0; ln_Kexc23=0; ln_Kexc24=0; ln_Kexc25=0;

for i=1:9

 ln_Kexc11=ln_Kexc11+b1(i)*log(Te)^(i-1);
 ln_Kexc12=ln_Kexc12+b2(i)*log(Te)^(i-1);
 ln_Kexc21=ln_Kexc21+b3(i)*log(Te)^(i-1);
 ln_Kexc22=ln_Kexc22+b4(i)*log(Te)^(i-1);
 ln_Kexc23=ln_Kexc23+b5(i)*log(Te)^(i-1);
 ln_Kexc24=ln_Kexc24+b6(i)*log(Te)^(i-1);

end

Kexc_11=exp(ln_Kexc11)*1e-6;   %m^3/s
Kexc_12=exp(ln_Kexc12)*1e-6;   %m^3/s
Kexc_21=exp(ln_Kexc21)*1e-6;   %m^3/s
Kexc_22=exp(ln_Kexc22)*1e-6;   %m^3/s
Kexc_23=exp(ln_Kexc23)*1e-6;   %m^3/s
Kexc_24=exp(ln_Kexc24)*1e-6;   %m^3/s
Kexc_25=Kh2_h;                  %m^3/s

Kelas_1=pi*(a_h^2)*sqrt(8*1.6e-19*Te/pi/9.11e-31);   %m^3/s

if Te<13
 Kelas_2=1.5e-13;                %m^3/s
else
 Kelas_2=1.2e-13;
end

%Excitation threshold energy, eV

Eexc_11=10.2; Eexc_12=10.2;
Eexc_21=11.37; Eexc_22=11.7; Eexc_23=12.2; Eexc_24=10;
Eexc_25=10;

Eexc1=Kexc_11*Eexc_11+Kexc_12*Eexc_12;
Eexc2=Kexc_21*Eexc_21+Kexc_22*Eexc_22+Kexc_23*Eexc_23+Kexc_24*Ee
xc_24+Kexc_25*Eexc_25;

viz_1=N_h*Kiz_11+N_h2*Kiz_12;
viz_2=N_h2*Kiz_2;

Eexc=[N_h*Eexc1/viz_1 N_h2*(Eexc2-Kexc_25*Eexc_25)/viz_2];
```

```
Eelas=[N_h*Kelas_1*3*9.11e-31*Te/m_h/viz_1  N_h2*Kelas_2*3*9.11e-31*Te/
2/m_h/viz_2];
Eion=[(N_h*Kiz_11*Eiz_11+N_h2*Kiz_12*Eiz_12)/viz_1  N_h2*Kiz_2*Eiz_2/
viz_2];
Edissc=N_h2*Kexc_25*Eexc_25/viz_2;

Pexc=e*[Eexc(1)*N_1*A1*ub1 Eexc(2)*N_2*A2*ub2];
Pelas=e*[Eelas(1)*N_1*A1*ub1 Eelas(2)*N_2*A2*ub2];
Pion=e*[Eion(1)*N_1*A1*ub1 Eion(2)*N_2*A2*ub2];
Pdissc=e*Edissc*N_2*A2*ub2;

El_1=(N_h*(Kiz_11*Eiz_11+Eexc1+Kelas_1*3*9.11e-31*Te/
m_h)+N_h2*Kiz_12*Eiz_12)/(N_h*Kiz_11+N_h2*Kiz_12);

El_2=N_h2*(Kiz_2*Eiz_2+Eexc2+Kelas_2*3*9.11e-31*Te/2/m_h)/viz_2;  %eV

e_iz=N_h2*Kiz_2*Eiz_2/viz_2;
e_exc=N_h2*Eexc2/viz_2;
e_elas=N_h2*Kelas_2*3*9.11e-31*Te/2/m_h/viz_2;

Eew=2*Te;
Eiw1=3.3*Te;Eiw2=3.7*Te;Eiw3=3.9*Te;
Et_1=El_1+Eew+Eiw1; Et_2=El_2+Eew+Eiw2;
Et_5=Eiw3;

El=[El_1 El_2];

Pex=e*V*N_2*(N_h2*Kex_25)*El_2;

% Compute absorbed power by plasma, Watt
Pabs=e*(N_1*A1*Et_1*ub1+N_2*A2*Et_2*ub2+N_3*A5*Et_5*ub5)+Pex

%(Reset Ne value for actual absorbed power, Pabs)

N=[N_h2 N_h Ne N_1 N_2 N_3];

Pw=[Pelas(1)+Pelas(2) Pdissc Pexc(1)+Pexc(2) Pion(1)+Pion(2) Pex Pabs];

N_h,N(4:6)
```

Appendix C

Hydrogen/Argon Mixture Discharge Global Model Program

```
%=====================================================%
% This program calculates the neutral, electron, and ion densities of   %
% H2-Ar discharges at low pressures (0.5-4 mTorr). The neutral and       %
% ionic species considered include H2, H, Ar, Ar+, H+, H2+, and H3+.     %
% The reactions included are electron-neutral and ion-neutral collisions.%
%=====================================================%

%Constant values
k=1.38e-23;
e=1.6e-19;
a_h=.53e-10;      %meter
m_h=1.67e-27;   %kg

%----------------- Plasma source condition ----------------------%
R=1.8; L=3;           %cm, cylindrical discharge dimension
Th=420; Th2=420;  %Kelvin; temperature of neutrals
Tar=420;
p=4;                  %mTorr, total chamber pressure
ng=p*1e-3*133.32/k/Th;
r_flow=5;             %H2/Ar flow(pressure) ratio
N_ar=1/(1+r_flow)*ng          %m^-3
N_h2=r_flow/(1+r_flow)*ng   %m^-3
p2=N_h2;
Ne=4.0e17;                    %m^-3
gamma=0.005;       %hydrogen surface recombination coefficient

fl_ar=0.4;             %fraction of diffusion loss to the wall
fl_h=.38;
```

```
lampda_1=1/(N_h2)/1e-19;    %m, H+ collision cross section=1e-19 m2
lampda_2=1/(N_h2)/1e-18;    %m, H2+ collision cross section=1e-18 m2
lampda_3=1/(N_ar)/1e-18;    %m, Ar+ collision cross section=1e-14 cm2
lampda_4=1/(N_ar)/1e-19;    %m, ArH+ collision cross section=1e-15 cm2
lampda_5=1/(N_h2)/1e-19;    %m, H3+ collision cross section=1e-15 cm2

lampda=[lampda_1 lampda_2 lampda_3 lampda_4 lampda_5];

for i=1:5

if lampda(i) >L
 hl=0.4; hr=0.4;
else
 hl=.86/sqrt(3+L*1e-2/2/lampda(i));
 hr=.8/sqrt(4+R*1e-2/lampda(i));
end
if i<=2
 Aeff(i)=fl_h*2*pi*R*(R*hl+L*hr)*1e-4;     %m2
elseif i<=4
 Aeff(i)=fl_ar*2*pi*R*(R*hl+L*hr)*1e-4;    %m2
else
 Aeff(i)=fl_h*2*pi*R*(R*hl+L*hr)*1e-4;     %m2
end

end

A1=Aeff(1); A2=Aeff(2); A3=Aeff(3); A4=Aeff(4); A5=Aeff(5);

Te=input('Input the electron temperature (eV), Te =');


V=pi*R^2*L*1e-6;              %m^3
v_avg=sqrt(8*k*Th/pi/m_h);    %m/s
z=(pi/L)^2+(2.405/R)^2;       %cm^-2

%---------- Calculate Kiz_11, Kiz_2, Kiz_12 ----------%
b1=[-3.27140e1 1.35366e1 -5.73933 1.56315 -2.87706e-1 3.48256e-2 -2.63198e-
3 1.11954e-4 -2.03915e-6];

b2=[-3.56864e1 1.733469e1 -7.76747 2.21158 -4.16984e-1 5.08829e-2 -
3.83274e-3 1.61286e-4 -2.89339e-6];

b3=[-3.83460e1 1.42632e1 -5.82647 1.72794 -3.59812e-1 4.82220e-2 -3.9094e-3
1.73878e-4 -3.25284e-6];
```

```
ln_Kiz2=0;
ln_Kiz11=0;
ln_Kiz12=0;

for i=1:9
 ln_Kiz11=ln_Kiz11+b1(i)*log(Te)^(i-1);
 ln_Kiz2=ln_Kiz2+b2(i)*log(Te)^(i-1);
 ln_Kiz12=ln_Kiz12+b3(i)*log(Te)^(i-1);
end

Kiz_11=exp(ln_Kiz11)*1e-6;    %m^3/s
Kiz_2=exp(ln_Kiz2)*1e-6;      %m^3/s
Kiz_12=exp(ln_Kiz12)*1e-6;    %m^3/s
Kiz_ar=6e-14*exp(-15.76/Te); %m3/s

% Determine hydrogen dissociation rate constant

if Te<7 & Te>=3
 m=log10(12/2.2)/log10(7/3);
 lg_Kh=m*(log10(Te)-log10(3))+log10(2.2e-15);
 Kh2_h=10^(lg_Kh);              %m^3/s
elseif Te<=14
 m=log10(2.1/1.2)/log10(14/7);
 lg_Kh=m*(log10(Te)-log10(7))+log10(1.2e-14);
 Kh2_h=10^(lg_Kh);
else
 Kh2_h=2.2e-14;
end

Kex_24=1.76e-15;  %m3/s, Rate constant for creation of ArH+
Kex_34=8.9e-16;   %m3/s, Rate constant for creation of ArH+
Kex_23=0;   %m3/s
Kex_32=0;   %m3/s
Kex_25=2.11e-15; %m3/s, Rate constant for creation of H3+
Kex_45=4.5e-16;  %m3/s, Rate constant for creation of H3+
Krecom=5e-15;    %m3/s, Rate constant for e-ArH+ recombination

% Ionization threshold energies, eV
Eiz_11=13.6; Eiz_2=15.4; Eiz_12=18;
Eiz_ar=15.76;

ub1=sqrt(1.6e-19*Te/m_h);      %m/s
ub2=sqrt(1.6e-19*Te/2/m_h);    %m/s
ub3=sqrt(1.6e-19*Te/40/m_h);   %m/s
ub4=sqrt(1.6e-19*Te/41/m_h);   %m/s
ub5=sqrt(1.6e-19*Te/3/m_h);    %m/s
```

```
%Solving for densities of H+,H2+,Ar+,ArH+,H3+

err1=10;
c1=6.5; c2=.17;

while err1 >2

A(1,:)=[V*gamma*k*Th*z*1e4/m_h/(2e-19*v_avg)/
N_h2+V*Kiz_11*Ne*(1+c1/p)     0     -V*(Kex_24*N_ar+Kex_25*N_h2)     -
V*Kex_34*N_h2 -V*Krecom*Ne 0];
A(2,:)=[-V*Ne*Kiz_11*(1+c1/p) A1*ub1 0 0 0 0];
A(3,:)=[0 0 V*N_ar*(Kex_24+Kex_23)+A2*ub2 -V*N_h2*Kex_32 0 0];
A(4,:)=[0 0 -V*N_ar*Kex_23 V*N_h2*(Kex_32+Kex_34)+A3*ub3 0 0];
A(5,:)=[0 0 -V*N_ar*Kex_24 -V*N_h2*Kex_34  A4*ub4+V*Ne*Krecom 0];
A(6,:)=[0 0 -V*N_h2*Kex_25 0 0 A5*ub5];

b=[V*Kh2_h*N_h2*Ne;          V*Ne*N_h2*Kiz_12;          V*N_h2*Ne*Kiz_2;
V*Ne*N_ar*Kiz_ar*(1+c2/p)/(1+c1/p); 0; 0]*(1+c1/p)];

X=A\b;
N_h=X(1);
N_1=X(2);N_2=X(3);N_3=X(4);N_4=X(5); N_5=X(6);

new=p2-N_h;
err1=abs(new-N_h2)/N_h2*100;
N_h2=new;

end

%Checking for reasonable Te assumption

ni=sum(X)-X(1);
err=abs(Ne-ni)/Ne*100

%------------ Computing the power absorbed by plasma ----------%

b1=[-2.81495e1 1.00983e1 -4.77196 1.46781 -2.97980e-1 3.86163e-2 -3.05169e-
3 1.33547e-4 -2.47609e-6];
b2=[-2.83326e1 9.58736 -4.83358 1.41586 -2.53789e-1 2.80071e-2 -1.87141e-3
6.98667e-5 -1.12376e-6];
b3=[-3.0819e1 1.03887e1 -4.25977 1.18123 -2.27751e-1 2.90058e-2 -2.28759e-3
1.00435e-4 -1.86993e-6];
b4=[-3.3482e1 1.3717e1 -5.92261 1.70972 -3.50523e-1 4.83438e-2 -4.13141e-3
1.94839e-4 -3.85428e-6];
b5=[-3.64659e1 1.43036e1 -6.07443 1.67731 -3.12871e-1 3.80542e-2 -2.86001e-
```

```
3 1.19964e-4 -2.14223e-6];
b6=[-2.85801e1 1.03854e1 -5.38383 1.95064 -5.39367e-1 1.00692e-1 -1.16076e-
2 7.41162e-4 -2.00137e-5];

ln_Kexc11=0; ln_Kexc12=0;
ln_Kexc21=0; ln_Kexc22=0; ln_Kexc23=0; ln_Kexc24=0; ln_Kexc25=0;

for i=1:9
 ln_Kexc11=ln_Kexc11+b1(i)*log(Te)^(i-1);
 ln_Kexc12=ln_Kexc12+b2(i)*log(Te)^(i-1);
 ln_Kexc21=ln_Kexc21+b3(i)*log(Te)^(i-1);
 ln_Kexc22=ln_Kexc22+b4(i)*log(Te)^(i-1);
 ln_Kexc23=ln_Kexc23+b5(i)*log(Te)^(i-1);
 ln_Kexc24=ln_Kexc24+b6(i)*log(Te)^(i-1);
end

Kexc_11=exp(ln_Kexc11)*1e-6;   %m^3/s
Kexc_12=exp(ln_Kexc12)*1e-6;   %m^3/s
Kexc_21=exp(ln_Kexc21)*1e-6;   %m^3/s
Kexc_22=exp(ln_Kexc22)*1e-6;   %m^3/s
Kexc_23=exp(ln_Kexc23)*1e-6;   %m^3/s
Kexc_24=exp(ln_Kexc24)*1e-6;   %m^3/s
Kexc_25=Kh2_h;                  %m^3/s

Kelas_1=pi*(a_h^2)*sqrt(8*1.6e-19*Te/pi/9.11e-31);   %m^3/s
if Te<13
 Kelas_2=1.5e-13;                %m^3/s
else
 Kelas_2=1.2e-13;
end

%Excitation threshold energy, eV

Eexc_11=10.2; Eexc_12=10.2;
Eexc_21=11.37; Eexc_22=11.7; Eexc_23=12.2; Eexc_24=10;
Eexc_25=10;

Eexc1=Kexc_11*Eexc_11+Kexc_12*Eexc_12;
Eexc2=Kexc_21*Eexc_21+Kexc_22*Eexc_22+Kexc_23*Eexc_23+Kexc_24*Ee
xc_24+Kexc_25*Eexc_25;

viz_1=N_h*Kiz_11+N_h2*Kiz_12;
viz_2=N_h2*Kiz_2;
Eexc=[N_h*Eexc1/viz_1 N_h2*(Eexc2-Kexc_25*Eexc_25)/viz_2];
Eelas=[N_h*Kelas_1*3*9.11e-31*Te/m_h/viz_1  N_h2*Kelas_2*3*9.11e-31*Te/
2/m_h/viz_2];
```

```
Eion=[(N_h*Kiz_11*Eiz_11+N_h2*Kiz_12*Eiz_12)/viz_1  N_h2*Kiz_2*Eiz_2/
viz_2];
Edissc=N_h2*Kexc_25*Eexc_25/viz_2;

Pexc=e*[Eexc(1)*N_1*A1*ub1 Eexc(2)*N_2*A2*ub2];
Pelas=e*[Eelas(1)*N_1*A1*ub1 Eelas(2)*N_2*A2*ub2];
Pion=e*[Eion(1)*N_1*A1*ub1 Eion(2)*N_2*A2*ub2 Eiz_ar*N_3*A3*ub3];
Pdissc=e*Edissc*N_2*A2*ub2;

El_1=(N_h*(Kiz_11*Eiz_11+Eexc1+Kelas_1*3*9.11e-31*Te/
m_h)+N_h2*Kiz_12*Eiz_12)/(N_h*Kiz_11+N_h2*Kiz_12);
El_2=N_h2*(Kiz_2*Eiz_2+Eexc2+Kelas_2*3*9.11e-31*Te/2/m_h)/
(N_h2*Kiz_2);  %eV

%Find the electron collisional energy loss of creating Ar+
if Te>=1 & Te<=2
 El_3=800-(800-88)*(Te-1)
elseif Te<=3
 El_3=88-(88-50)*(Te-2)
elseif Te<=4
 El_3=50-(50-38)*(Te-3)
elseif Te<=5
 El_3=38-(38-31)*(Te-4)
elseif Te<=6
 El_3=31-(31-28)*(Te-5)
elseif Te<=7
 El_3=28-(28-25)*(Te-6)
elseif Te<=8
 El_3=25-(25-23)*(Te-7)
elseif Te<=9
 El_3=23-(23-22)*(Te-8)
elseif Te<=10
 El_3=22-(22-21)*(Te-9)
elseif Te<=20
 El_3=21-(21-20)*(Te-10)
elseif Te>20
  El_3=20
end


Eew=2*Te;  %eV
Eiw1=3.3*Te; Eiw2=3.7*Te; Eiw3=4.7*Te; Eiw4=5.2*Te; Eiw5=3.9*Te;
Et_1=El_1+Eew+Eiw1; Et_2=El_2+Eew+Eiw2; Et_3=El_3+Eew+Eiw3;
Et_4=Eew+Eiw4; Et_5=Eew+Eiw5;

Pex=e*V*[N_2*(N_ar*Kex_23+N_ar*Kex_24+N_h2*Kex_25)*El_2
```

```
N_3*N_h2*(Kex_32+Kex_34)*El_3]

% Compute absorbed power by plasma, Watt
Pabs=e*(N_1*A1*Et_1*ub1+N_2*A2*Et_2*ub2+N_3*A3*Et_3*ub3+N_4*A4*
Et_4*ub4+N_5*A5*Et_5*ub5)+Pex(1)+Pex(2)

%(Reset Ne value for actual absorbed power Pabs)

N=[N_ar N_h2 N_h Ne N_1 N_2 N_3 N_4 N_5];
Pw=[Pelas(1)+Pelas(2) Pdissc Pexc(1)+Pexc(2) Pion(1)+Pion(2) Pion(3) Pex
Pabs];
N(5:9)
```

BIBLIOGRAPHY

Bibliography

[1] **Plasma Etching: An Introduction**, edited by D. M. Manos, and D.L. Flamm, Academic, New York (1988).

[2] S. Samukawa, M. Sasaki, and Y. Suzuki: "Extremely high selective, highly isotropic, and high rate ECR plasma etching for n^+ poly-Si at the ECR position", J. Vac. Sci. Technol. B 8, 1192 (1990).

[3] D. Henry, J. M. Francou, and A. Inward: "Resonant inductive plasma etching evalution of an industrial prototype", J. Vac. Sci. Technol. A 10, 3426 (1992).

[4] S. Samukawa, M. Sasaki, and Y. Suzuki: "Perfect selective and highly anisotropic electron cyclotron resonance plasma etching for WSi_x/ploy-Si at electron cyclotron resonance position", J. Vac. Sci. Technol. B 8, 1062 (1990).

[5] J. Paraszczak, M. Hatzakis, E. Babich, J. Shaw, E. Arthur, B. Grenon, and M. Depaul: "Plasma etching of polymers for multilayer lithography", **Microcircuit Engineering 84**, 517 (1984).

[6] G. T. Salbert, D. K. Reinhard, and J. Asmussen: "Oxide growth on Si using a microwave ECR oxygen plasma", J. Vac. Sci. Technol. A 8, 2919 (1990).

[7] J. L. Rogers, P. S. Andry, W. J. Varhue, P. McGaughnea, E. Adams and R. Kontra: "Low-temperature homoepitaxial growth of Si by electron cyclotron resonance plasma enchanced chemical vapor deposition", Appl. Phys. Lett. 67, 971 (1995).

[8] P. Gadgil, D. Dane, and T. D. Mantei: "Selective and uniform high rate etching of polysilicon in a magnetically confined microwave discharge", J. Vac. Sci. Technol., B 11, 216 (1993).

[9] J. L. Shohet, "Plasma science and engineering," in **Encyclopedia of Science and Technology**. San Diego: Harcourt, Brace, Jovanovich, 1987.

[10] K. Niazi, A. J. Lichtenberg, M. A. Lieberman and F. L. Flamm, "Operation of a helical resonator plasma source", Plasma Source Sci. Technol. 3, 482-495, 1994.

[11] J. M. Cook, D. E. Ibbotson, P. D. Foo, and D. L. Flamm, "Etching results and comparison of low pressure electron cyclotron resonance and radio frequency discharge sources," J. Vac. Sci. Technol. A 8, 1820-1824, 1990

[12] J. M. Cook, D. E. Ibbotson, and D. L. Flamm, "Application of a low-pressure radio frequency discharge source to ploysilicon gate etching," J. Vac. Sci. Technol. B 8, 1-4, 1990

[13] R. W. Boswell, "Plasma production using a standing helicon wave," Phys. Lett. A 33, 457, 1970.

[14] F. F. Chen, "Landau damping of helicon waves," Australian National Univ. Report ANU-PRL IR, 85/12, 1985, unpublished.

[15] F. F. Chen, Plasma Phys. Controlled Fusion, 33, 339, 1991.

[16] A. J. Perry, D. Vender, and R. W. Boswell, D. Vender, "The application of the helicon source to plasma processing," J. Vac. Sci. Technol. B 9, 310-317, 1991.

[17] A. R. Ellingboe, and R. W. Boswell, "Capacitive, inductive, and helicon-wave modes of operation of a helicon plasma source," Phys. Plasmas 3, 2797-2804, 1996.

[18] F. F. Chen, "Helicon plasma sources," Ch. 1 in **High Density Plasma Soruces**, O. A. Popov ed., Park Ridge, NJ, (1995) and its quoted references.

[19] T. Shoji, Y. Sakawa, S. Nakazawa, K. Kadota, and T. Sato, "Plasma production by helicon wave," Plasma Source Sci. Technol. 2, 5-10, 1993 and its quoted references.

[20] N. Jiwari, H. Iwasawa, A. Narai, H. Sakaue, H. Shindo, T. Shoji, and Y. Horiike, "Al etching characteristics employing helicon wave plasma," Jpn. J. Appl. Phys. 32, 3019-3022, 1993.

[21] D. L. Pappas and J. Hopwood: "Deposition of diamond like carbon using a planar radio frequency induction plasma", J. Vac. Sci. Technol. A 12, 1576 (1993).

[22] J. Hopwood, C. R. Guarnieri, S. J. Whitehair, and J. J. Cuomo: "Langmuir probe measurements of radio frequency induction plasma", J. Vac. Sci. Technol. A 11, 152 (1993).

[23] J. Hopwood, C. R. Guarnieri, S. J. Whitehair, and J. J. Cuomo: "Electromagnetic fields in a radio-frequency induction plasma", J Vac. Sci. Technol. A 11, 147 (1993).

[24] K. Suzuki, S. Okudaira, N. Sakudo, and I. Kanomato, "Microwave plasma etching", Jpn. J. Appl. Phys. 16, 1979-1984, 1977.

[25] L. Bardos, G. Longar, I. Stoll, J. Musil, and F. Zacek, "A method of formation of thin oxide films on silicon in a microwave magnetoactive plasma," J. Phys. D: Appl. Phys. 8, L195-197, 1975.

[26] S. Y. Shapoval, V. T. Petrashov, O. A. Popov, M. D. Yoder, P. Maciel, and C. K. C. Lok, "Electron cyclotron resonance plasma chemical vapor deposition of large area uniform silicon nitride film." J. Vac. Sci. Technol. A 9, 3071, 1991.

[27] W. Holber, "Electron cyclotron resonance ion sources," in **Handbook of Ion Beam Processing Technology, Principles, Deposition, Fim Modification and Synthesis**, J. Cuomo, S. Rossnagel, and H. Kauffman, eds., Noyes Publications 1989.

[28] O. A. Popov, "Electron cyclotron resonance plasma sources and their use in plasma assisted chemical vapor deposition of thin films," in **Physics of Thin Films**, Vol. 18, M. Francombe, and J. Vossen, eds., New York, NY:Academic Press, 1994.

[29] M. A. Liebermann, and R. A. Gottscho, in **Physics of Thin Films**, Vol. 18, M. Francombe, and J. Vossen, eds., Academic Press, 1994.

[30] James E. Stevens, "Electron cyclotron resonsnce plasma sources," in **High Density Plasma Sources**, O. A. Popov ed., Park Ridge, NJ, 1995.

[31] T. D. Mantei and S. Dhole, "Characterization of a permanent magnet electron cycletron resonance plasma source," J. Vac. Sci. Technol. B 9, 26-33, 1991.

[32] A. Narai, T. Hashimoto, T. Ichihashi, H. Shincho, and Y. Horioko, "Compact electron cycletron resonance plasma-etching reactor employing permanent magnets", Jpn. J. Appl. Phys. 30, 3159-3163, 1991.

[33] M. Pichot, A. Durandet, J. Pelletier, Y. Arnal and L. Vallier, "Microwave multipolar plasmas excited by distributed ECR : Concept and performance," Rev. Sci. Instrum. 59, 1072-1075, 1988.

[34] J. Asmussen, "Microwave plasma disk processing machines," Ch. 6 in **High Density Plasma Sources**, O. A. Popov ed., Park Ridge, NJ, 1995.

[35] J. Asmussen, **Handbook of Plasma Processing Technology**, Ch.11, S. M. Rossnagel, J. J. Cuomo, and W. D. Westwood, eds., Noyes, Park Ridge, NJ (1990).

[36] J. Root, and J. Asmussen, "Experimental performance of a microwave cavity, plasma disk ion source," Rev. Sci. Instrum. 56, 1511, 1985.

[37] M. Meyyappan and T. R. Govindan, "Modeling of electron cyclotron resonance discharges," IEEE Trans. Plasma Sci. 23, 623, 1995.

[38] N. S. Yoon, N.-H. Choi, H.-B. Park, and D.-I. Choi, "One-dimensional fluid model of ECR discharge with inhomogeneity effects of external magnetic field," IEEE Trans. Plasma Sci. 23, 609, 1995.

[39] M. Li, H.-M. Wu, and Y. Chen, "Two-dimensional simulation of inductive plasma sources with self-consistant power deposition," IEEE Trans. Plasma Sci. 23, 558, 1995.

[40] D. P. Lymberopoulos and D. J. Economou, "Two-dimensional simulation of polysilicon etching with chlorine in a high density plasma reactor," IEEE Trans. Plasma Sci. 23, 573, 1995.

[41] M. Surendra, and D. B. Graves, "Particle simulations of radio-frequency glow discharge," IEEE Trans. Plasma Sci. 19, 144, 1991.

[42] K. Nagayama, B. Farouk, and Y. H. Lee, "Particle simulation of radio-frequency plasma discharges of methane for carbon film deposition," IEEE Trans Plasma Sci. Vol. 26, 125, 1998.

[43] S. C. Kuo, E. E. Kunhardt, and S. P. Kuo, "Monte Carlo simulation of electron behavior in an ECR discharge," J. Appl. Phys. 73, 4197-4203, 1993.

[44] N.-H. Choi, W. H. Koh, N. S. Yoon, H.-B. Park, and D.-I. Choi, "One-dimensional hybrid modeling and simulation of ECR discharge," IEEE Trans. Plasma Sci. 23, 617, 1995.

[45] D. B. Graves, H. Wu, and R. K. Porteous, "Modeling and simulation of high density plasmas," Jpn. J. Appl. Phys. 32, 2999-3006, 1993.

[46] T. A. Grotjohn, "Numerical modeling of a compact ECR ion source," Rev. Sci. Instru. 63, 2535-2537, 1990.

[47] Venkatesh P. Gopinath and Timothy A. Grotjohn, "Three dimensional electromagnetic PIC model of a compact ECR plasma source," IEEE Trans. Plasma Sci., Vol. 23, 602-608, 1995.

[48] T. A. Grotjohn, "Modeling the electron heating in a compact electron cyclotron resonance ion source," Rev. Sci. Instru. 67, 921-923, 1996.

[49] V. M. Donnelly, Ch. 1, **Plasma Diagnostics** Vol. 1, O. Auciello and D.L. Flamm edited, Academic, New York 1989.

[50] F. F. Chen, **Plasma Diagnostic Techniques**, R. H. Huddlestone and S. L. Leonard edited, P.113, Academic Press, New York (1965).

[51] ***Principles of Plasma Discharges and Materials Processing***, by Michael A. Liberman and Allan J. Lichtenberg, Ch. 6, J. Wiley & Sons (1994).

[52] M. J. Druyvestefyn, Z. Phys. 64, 781 (1920).

[53] E. Heideneich, J. Parazczak, M. Moisan, and G. Sauv: "Electron energy distributions in oxygen microwave plasmas", J. Vac. Sci. Technol. B 6, 288 (1988).

[54] W. Rundle, D. R. Clark, and J. M. Deckers: "Electron energy distribution functions in an O_2 glow discharge", Can. J. Phys. 51, 144 (1973).

[55] M. V. Malyshev and V. M. Donnelly, "Determination of electron temperatures in plasmas by multiple rare gas optical emission, and implications for advanced actinometry," J. Vac. Sci. Technol. A 15, 550 (1997).

[56] J. W. Coburn and M. Chen, "Optical emission spectroscopy of reactive plasmas: A method for correlation emission intensities to reactive particle density", J. Appl. Phys. 51, 3134, (1980).

[57] J.-S. Jeng, J. Ding, J. W. Taylor, and N. Hershkowitz, "Absolute fluorine atom concentrations in RIE and ECR CF_4 plasmas measured by actinomerty," Plasma Sources Sci. Technol. 3, 154, 1994.

[58] Kevin L. Junck, and Ward D. Getty, "Comparison of Ar ECR plasmas in three magnetic field configurations. I. Electron temperature and plasma density," J. Vac. Sci. Technol. A 12(5), 2767, 1994.

[59] A. Gicquel, M. Chenevier, and M. Lefebvre, "Spatially resolved spectroscopic analysis of the plasma," in Handbook of Industrial Diamonds and Diamond Films, ed. M. A. Prelas, G. Popovici, L. K. Bigelow, Marcel Dekker, 1998.

[60] J. D. Walker Jr. and R. M. St. John, "Design of a high density atomic hydrogen source and determination of Balmer cross sections", J. Chem Phys. 61, 2394 (1974).

[61] G. R. Mohlmann, F. J. De Heer and J. Los, "Emission cross sections of Balmer α, β, γ radiation for electrons on H_2 and D_2", Chem. Phys., 25, 103 (1977).

[62] 1990-91 CRC Handbook of Chemistry and Physics, 71st edition, Lide D.R. edited, p.10-129.

[63] P. V. Feltsan and I. P. Zapesochnyi, Ukr. Fiz. Zh. 12, 633, 1967.

[64] P. V. Feltsan and I. P. Zapesochnyi, Ukr. Fiz. Zh. 12, 1423, 1967.

[65] P. V. Feltsan and I. P. Zapesochnyi, Ukr. Fiz. Zh. 13, 205, 1968.

[66] James H. Stapleton, Chap. 1 in **Linear Statistical Models**, John Wiley & Sons, New York, NY, 1995.

[67] J. Asmussen, R. Fritz, L. Mahoney, G. Fournier, and G. Demaggio, "ECR ion and free radical sources for MBE applications," Rev. Sci. Instrum., 61, 282 (1990).

[68] S. Strite, J. Ruan, Z. Li, N. Manning, A. Salvador, H. Chen, D. J. Smith, W. J. Choyke, and H. Morkoc, "An investigation of the properties of cubic GaN grown on GaAs by plasma assisted molecular-beam epitaxy," J. Vac. Sci. Technol., B 9, 1924 (1991).

[69] M. E. Sherwin, G. O. Munns, E. G. Woelk, T. J. Drummond, M. E. Elta, F. L. Terry, and G. I. Haddad, "The design of an ECR plasma system and its application to InP grown by CBE," J. Cryst. Growth, 111, 605 (1991)

[70] C. Pawlowski and M. Aslam, "Laser ablation deposition of $YBa_2Cu_3O_{7-x}$ thin films

using a microwave plasma disk reactor oxygen source," J. Appl. Phys., 74, 6430 (1993).

[71] K. Yamamoto, R. H. Hammond, and J. S. Harris, Jr., "The relative effect on the oxygen concentration in $YBa_2Cu_3O_{7-x}$ of atomic and ionic oxygen fluxes, produced by a small compact ECR source," J. Vac. Sci. Technol. A9, 2587 (1991).

[72] C. R. Abernathy, P. W. Wisk, S. J. Pearton, and F. Ren, "Effect of electron cyclotron resonance generated hydrogen plasmas on carbon incorporation and interfacial quality of GaAs and AlGaAs grown by metalorganic molecular-beam epitaxy," J. Vac. Sci. Technol. B, 10, 2153 (1992).

[73] A. K. Srivastava, J. Asmussen, T. Antaya, and K. Harrison, "The study of a 2.45 GHz and plasma source as a plasma generator for the SCECR electron cyclotron resonance ion source," Rev. Sci. Instrum. 65, 1135 (1994).

[74] A. K. Srivastava, M. Dahimene, T. Grotjohn, and J. Asmussen, "Experimental charaterization of a compact ECR ion source," Rev. Sci. Instrum. 63, 2556 (1992).

[75] A. K. Srivastava, and J. Asmussen, "Comparison of the operational performance of a compact ECR plasma source at excitation frequencies of 2.45 GHz and 915 MHz," J. Vac. Sci. Technol. A 11, 1307 (1993).

[76] A. K. Srivastava and J. Asmussen, "Measurements of the impressed electric field inside a coaxial electron cyclotron resonance plasma source," Rev. Sci. Instrum., 66, 1028 (1995)

[77] J. Asmussen, T. A. Grotjohn, P. U. Mak, M. A. Perrin, "The design and application of electron cyclotron resonance discharges," IEEE Trans. Plasma Science, 25, 1196 (1997).

[78] J. Asmussen, "Coaxial Cavity Type Radio Frequency Wave, Plasma Generating Apparatus." US Patent 4,906,900 (1990).

[79] A. K. Srivastava, "Properties of electron cyclotron resonance plasma sources", Ph. D. Dissertation, Department of Electrical Engineering, Michigan State University (1995).

[80] M.-H. Tsai and T. A. Grotjohn, "Investigation of diagnostic sensors and control models for a compact ion source", invited paper, the 24th IEEE International Conference on Plasma Science, May 19-22, 1997.

[81] C. Lee, and M. A. Lieberman: "Global model of Ar, O_2, Cl_2, and Ar/O_2 high-density plasma discharges", J. Vac. Sci. Technol. A13, 368 (1995).

[82] V. Vahedi, "Modeling and simulation of rf discharges used for plasma processing," Thesis, University of California, Berkeley, 1993, or V. Vahedi, R. A. Steward, and

M. A. Lieberman, J. Vac. Sci. Technol. A11, 1275, 1993.

[83] ***Principles of Plasma Discharges and Materials Processing***, by Michael A. Liberman and Allan J. Lichtenberg, Ch. 3, J. Wiley & Sons (1994).

[84] D. Jacquin, J. Bretagne, and R. Ferdinand, "Kinetic study of low-pressure H_2 multipole discharge," Plasma Chem. and Plasma Processing 9, 165, 1989. (Also see references listed within.)

[85] D. K. Otorbaev, M. C. M. van de Sanden, and D. C. Schram, "Heterogeneous and homogeneous hydrogen kinetics in plasma chemistry," Plasma Sources Sci. Technol. 4, 293-301, 1995. (Also see references listed within.)

[86] K. Hassouni, S. Farhat, C. D. Scott, and A. Gicquel, "Modeling species and energy transport in moderate pressure diamond deposition H-2 plasmas," J. De Phys. III, 6, 1229 (1996).

[87] L. St-Onge, and M. Moisan, "Hydrogen atom yield in rf and microwave hydrogen discharge," Plasma Chem. & Plasma Procs. 14 (2), 87, (1994). (Also see references listed within.)

[88] W. G. Graham, "The kinetics of negative hydrogen ions in discharges," Plasma Sources Sci. Technol., 4, 281-292 (1995).

[89] A. V. Phelps, "Cross sections and swarm coefficients for H^+, H_2^+, H_3^+, H, H_2 and H^- in H_2 for energies from 0.1 eV to 10 keV", J. Phys. Chem. Ref. Data, 19, 653 (1990).

[90] A. V. Phelps, "Collisions of H^+, H_2^+, H_3^+, ArH^+, H^-, H, and H_2 with Ar and of Ar^+ and ArH^+ with H_2 for energies from 0.1eV to 10 keV", J. Phys. Chem. Ref. Data 21, p.883, 1992.

[91] D. K. Otorbaev, A.J.M. Buuron, N. T. Guerassimov, and M.C.M. van de Sanden, "Spectroscopic measurement of atomic hydrogen level populations and hydrogen dissociation degree in expanding cascaded arc plasma", J. Appl. Phys. 76, p.4499, 1994.

[92] H. Villinger, J. H. Futrell, F. Howorka, N. Duric, and W. Lindinger, "The proton transfer from ArH^+ to various neutrals," J. Chem. Phys. 76, 3529, 1982.

[93] C. D. Scott, S. Farhat, A. Gicquel, K. Hassouni, and M. Lefebvre, "Determining electron temperature and density in a hydrogen microwave plasma," J. Thermophysics and Heat Transfer 10, 426-435, 1996.

[94] H. Tawara,Y. Itikawa, H. Nishimura, and M. Yoshino, "Cross sections and related data for electron collisions with hydrogen molecules and molecular ions," J. Phys. Chem. Ref. Data, Vol. 19, No. 3, (1990).

[95] R. K. Janev, W. D. Langer, K. Evans, Jr, D. E. Post, ***Elementary Processes in Hydrogen-Helium Plasmas***, Springer-Verlag, Berlin and Heidelberg, 1987.

[96] Keiji Sawada and Takashi Fujimoto, "Effective ionization and dissociation rate coefficients of molecular hydrogen in plasma," J. Appl. Phys. 78 (5), 2913 (1995).

[97] J. Geddes, R. W. McCullough, A. Donnelly and H. B. Gilbody, "Dissociation of hydrogen in high-frequency discharges," Plasma Sources Sci. Technol. 2, 93-99, 1993.

[98] V. Gopinath, G. T. Salbert, T. A. Grotjohn, and D. K. Reinhard, "electron cyclotron resonance sputter removal of SiO_2 on silicon wafers," J. of Vacuum Science and Technol. B 11, pp. 2067-2070, 1993.

[99] P. Mak, M.-H. Tsai, J. Natarajan, B. L. Wright, T. A. Grotjohn, F. M. A. Salam, M. Siegel, and J. Asmussen, "Investigation of multipolar electron cyclotron resonance plasma source sensors and models for plasma control", J. of Vacuum Sci. and Technol., vol. A-14, pp. 1894-1900, 1996.

[100]V. A. Godyak, *Soviet Radio Frequency Discharge Research* (Delphic Associates, Inc., Falls Church, VA, 1986), Chap. 5.

[101]A. J. Lichtenberg, V. Vahedi, M. A. Lieberman, and T. Rognlien, "Modeling electronegative plasma discharges," J. Appl. Phys. 75, 2339 (1994).

[102]N. Hershkowitz, K. N. Leung, and T. Romesser, "Plasma leakage through a low-beta line cusps", Phys. Rev. Lett. 35, p.277-280, 1975.

[103]K. N. Leung, N. Hershkowitz, and K. R. MacKenzie, "Plasma confinement by localized cusps", Phys. Fluids 19, p.1045, 1976.

[104]G. Mattieussent and J. Pelletier in **Microwave Excited Plasmas**, edited by M. Moisan and J. Pelletier, Elsevier, Amsterdam, 1992.

[105]K. N. Leung, T. K. Samec, and A. Lamm, "Optimization of permanent magnet plasma confinement", Phys. Letts. 51A, p.490, 1975.

[106]K. N. Leung, G. R. Taylor, J. M. Barrick, S.L. Paul, and R.E. Kribel, "Plasma confinemnet by pemanent magnet boundaries", Phys. Letts. 57A, p.145, 1976.

[107]L. Thimas, J. l. Jauberteau, I. Jauberteau, J. Aubreton, and A. Catherinot, "Characterization of an Argon-hydrogen microwave discharge used as an atomic hydrogen source", Plasma Chem. and Plasma Processng 17, p.193, 1997.

[108]J. Hopwood, D. K. Reinhard, and J. Asmusen, "Charged particle densities and energy distributions in a multipolar ECR plasma etching source," J. Vac. Sci. Technol. A8, 3103, 1990.

[109]J. Forster, C. C. Klipper, L. A. Berry, and S. M. Gorbatkin, "Doppler shift measurements of ion energy distribution widths in an ECR/multipole hybrid reactor," J. Vac. Sci. Technol. A 10, 3114, 1992.

[110]D. J. Trevor, N. Sadeghi, T. Nakamo, J. Derouard, R. A. Gottscho, P. D. Foo, and J. M. Cook, "Spacially resolved ion velocity distributions in a diverging field ECR plasma reactor," Appl. Phys. Lett 57, 1188-1190, 1990.

[111]G. P. Davis, and R. A. Gottscho, "Measurement of spatially resolved gas-phase plasma temperatures by optical emission and laser-induced fluorescence spectroscopy," J. Appl. Phys. 54, 3080, 1983.